A Description of the Advanced Research WRF Version 3

William C. Skamarock
Joseph B. Klemp
Jimy Dudhia
David O. Gill
Dale M. Barker
Michael G. Duda
Xiang-Yu Huang
Wei Wang
Jordan G. Powers

NCAR TECHNICAL NOTES

The Technical Note series provides an outlet for a variety of NCAR manuscripts that contribute in specialized ways to the body of scientific knowledge but which are not suitable for journal, monograph, or book publication. Reports in this series are issued by the NCAR Scientific Divisions; copies may be obtained on request from the Publications Office of NCAR. Designation symbols for the series include:

EDD: *Engineering, Design, or Development Reports*
Equipment descriptions, test results, instrumentation, and operating and maintenance manuals.

IA: *Instructional Aids*
Instruction manuals, bibliographies, film supplements, and other research or instructional aids.

PPR: *Program Progress Reports*
Field program reports, interim and working reports, survey reports, and plans for experiments.

PROC: *Proceedings*
Documentation of symposia, colloquia, conferences, workshops, and lectures. (Distribution may be limited to attendees.)

STR: *Scientific and Technical Reports*
Data compilations, theoretical and numerical investigations, and experimental results.

Contents

Appendices

List of Figures

List of Tables

Acknowledgments

Many people beyond this document's author list have contributed to the development of dynamics and physics. For the dynamics solver development, we would like to thank Louis Wicker for his assistance with the Runge-Kutta integration scheme; George Bryan and Jason Knievel for contributing in the turbulent mixing algorithms and other model filters; Mark Richardson, Anthony Toigo and Claire Newman for generalizing the WRF code for global applications.

For physics contributions, we would like to thank Tom Black, John Brown, Kenneth Campana, Fei Chen, Shu-Hua Chen, Ming-Da Chou, Aijun Deng, Mike Ek, Brad Ferrier, Georg Grell, Bill Hall, Songyou Hong, Zavisa Janjic, Jack Kain, Hiroyuki Kusaka, Ruby Leung, Jeong-Ock Lim, Kyo-Sun Lim, Yubao Liu, Chin-Hoh Moeng, Ken Mitchell, Eli Mlawer, Hugh Morrison, Jon Pleim, Tanya Smirnova, Dave Stauffer, Wei-Kuo Tao, Mukul Tewari, Greg Thompson, Guenther Zaengl and others. We also acknowledge the contribution by Min Chen, Ju-Won Kim, Steven Peckham, Tanya Smirnova, John Brown and Stan Benjamin for the digital filter initialization development.

The development of WRF-Var represents an international team effort. We would like to acknowledge the following people for their contributions to the WRF-Var system: Yong-Run Guo, Wei Huang, Qingnong Xiao, Syed Rizvi, Francois Vandenberghe, Mike McAtee, Roy Peck, Wan-Shu Wu, Dezso Devenyi, Jianfeng Gu, Mi-Seon Lee, Ki-Han Youn, Eunha Lim, Hyun-Cheol Shin, Shu-Hua Chen, Hui-Chuan Lin, John Bray, Xin Zhang, Zhiquan Liu, Tom Auligne, Xianyan Zhang, and Yongsheng Chen.

We would like express our appreciation to John Michalakes for developing the WRF Software Framework. We would also like thank Jacques Middlecoff, Tom Henderson, Al Bourgeois, Matt Bettencourt, Todd Hutchinson, Kent Yang, and Dan Schaffer for their contributions to the software development.

Finally, we would like to thank George Bryan, Jim Bresch, Jian-Wen Bao and John Brown for their careful review of this document. We also thank Cindy Bruyère for assistance with the graphics.

x

Chapter 1

Introduction

The Weather Research and Forecasting (WRF) model is a numerical weather prediction (NWP) and atmospheric simulation system designed for both research and operational applications. WRF is supported as a common tool for the university/research and operational communities to promote closer ties between them and to address the needs of both. The development of WRF has been a multi-agency effort to build a next-generation mesoscale forecast model and data assimilation system to advance the understanding and prediction of mesoscale weather and accelerate the transfer of research advances into operations. The WRF effort has been a collaborative one among the National Center for Atmospheric Research's (NCAR) Mesoscale and Microscale Meteorology (MMM) Division, the National Oceanic and Atmospheric Administration's (NOAA) National Centers for Environmental Prediction (NCEP) and Earth System Research Laboratory (ESRL), the Department of Defense's Air Force Weather Agency (AFWA) and Naval Research Laboratory (NRL), the Center for Analysis and Prediction of Storms (CAPS) at the University of Oklahoma, and the Federal Aviation Administration (FAA), with the participation of university scientists.

WRF reflects flexible, state-of-the-art, portable code that is efficient in computing environments ranging from massively-parallel supercomputers to laptops. Its modular, single-source code can be configured for both research and operational applications. Its spectrum of physics and dynamics options reflects the experience and input of the broad scientific community. Its WRF-Var variational data assimilation system can ingest a host of observation types in pursuit of optimal initial conditions, while its WRF-Chem model provides a capability for air chemistry modeling.

WRF is maintained and supported as a community model to facilitate wide use internationally, for research, operations, and teaching. It is suitable for a broad span of applications across scales ranging from large-eddy to global simulations. Such applications include real-time NWP, data assimilation development and studies, parameterized-physics research, regional climate simulations, air quality modeling, atmosphere-ocean coupling, and idealized simulations. As of this writing, the number of registered WRF users exceeds 6000, and WRF is in operational and research use around the world.

The principal components of the WRF system are depicted in Figure 1.1. The WRF Software Framework (WSF) provides the infrastructure that accommodates the dynamics solvers, physics packages that interface with the solvers, programs for initialization, WRF-Var, and WRF-Chem. There are two dynamics solvers in the WSF: the Advanced Research WRF (ARW) solver (originally referred to as the Eulerian mass or "em" solver) developed primarily at NCAR, and the
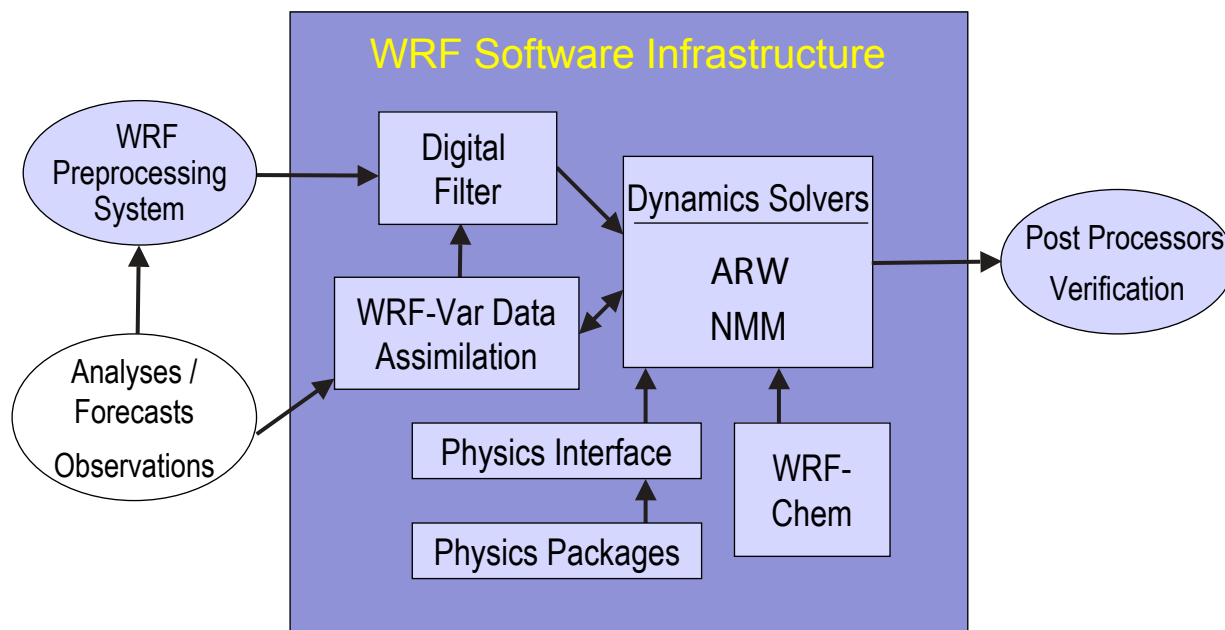
Figure 1.1: WRF system components.

NMM (Nonhydrostatic Mesoscale Model) solver developed at NCEP. Community support for the former is provided by the MMM Division of NCAR and that for the latter is provided by the Developmental Testbed Center (DTC).

1.1 Advanced Research WRF

The ARW is the ARW dynamics solver together with other components of the WRF system compatible with that solver and used in producing a simulation. Thus, it is a subset of the WRF modeling system that, in addition to the ARW solver, encompasses physics schemes, numerics/dynamics options, initialization routines, and a data assimilation package (WRF-Var). The ARW solver shares the WSF with the NMM solver and all other WRF components within the framework. Physics packages are largely shared by both the ARW and NMM solvers, although specific compatibility varies with the schemes considered. The association of a component of the WRF system with the ARW subset does not preclude it from being a component of WRF configurations involving the NMM solver. The following section highlights the major features of the ARW, Version 3, and reflects elements of WRF Version 3, which was first released in April 2008.

This technical note focuses on the scientific and algorithmic approaches in the ARW, including the solver, physics options, initialization capabilities, boundary conditions, and grid-nesting techniques. The WSF provides the software infrastructure. WRF-Var, a component of the broader WRF system, was adapted from MM5 3DVAR (Barker et al., 2004) and is encompassed within the ARW. While WRF-Chem is part of the ARW, Version 3, it is described outside of this technical note. Those seeking details on WRF-Chem may consult Grell et al. (2005) and

http://ruc.fsl.noaa.gov/wrf/WG11/status.htm . For those seeking information on running the ARW system, the ARW User's Guide (Wang et al., 2008) has the details on its operation.

1.2 Major Features of the ARW System, Version 3

ARW Solver

- *Equations:* Fully compressible, Euler nonhydrostatic with a run-time hydrostatic option available. Conservative for scalar variables.
- *Prognostic Variables:* Velocity components u and v in Cartesian coordinate, vertical velocity w, perturbation potential temperature, perturbation geopotential, and perturbation surface pressure of dry air. Optionally, turbulent kinetic energy and any number of scalars such as water vapor mixing ratio, rain/snow mixing ratio, cloud water/ice mixing ratio, and chemical species and tracers.
- *Vertical Coordinate:* Terrain-following, dry hydrostatic-pressure, with vertical grid stretching permitted. Top of the model is a constant pressure surface.
- *Horizontal Grid:* Arakawa C-grid staggering.
- *Time Integration:* Time-split integration using a 2nd- or 3rd-order Runge-Kutta scheme with smaller time step for acoustic and gravity-wave modes. Variable time step capability.
- *Spatial Discretization:* 2nd- to 6th-order advection options in horizontal and vertical.
- *Turbulent Mixing and Model Filters:* Sub-grid scale turbulence formulation in both coordinate and physical space. Divergence damping, external-mode filtering, vertically implicit acoustic step off-centering. Explicit filter option.
- *Initial Conditions:* Three dimensional for real-data, and one-, two- and three-dimensional for idealized data. Digital filtering initialization (DFI) capability available (real-data cases).
- *Lateral Boundary Conditions:* Periodic, open, symmetric, and specified options available.
- *Top Boundary Conditions:* Gravity wave absorbing (diffusion, Rayleigh damping, or implicit Rayleigh damping for vertical velocity). Constant pressure level at top boundary along a material surface. Rigid lid option.
- *Bottom Boundary Conditions:* Physical or free-slip.
- *Earth's Rotation:* Full Coriolis terms included.
- *Mapping to Sphere:* Four map projections are supported for real-data simulation: polar stereographic, Lambert conformal, Mercator, and latitude-longitude (allowing rotated pole). Curvature terms included.
- *Nesting:* One-way interactive, two-way interactive, and moving nests. Multiple levels and integer ratios.
- *Nudging:* Grid (analysis) and observation nudging capabilities available.
- *Global Grid:* Global simulation capability using polar Fourier filter and periodic east-west conditions.

Model Physics

- *Microphysics:* Schemes ranging from simplified physics suitable for idealized studies to sophisticated mixed-phase physics suitable for process studies and NWP.
- *Cumulus parameterizations:* Adjustment and mass-flux schemes for mesoscale modeling.
- *Surface physics:* Multi-layer land surface models ranging from a simple thermal model to full vegetation and soil moisture models, including snow cover and sea ice.
- *Planetary boundary layer physics:* Turbulent kinetic energy prediction or non-local K schemes.
- *Atmospheric radiation physics:* Longwave and shortwave schemes with multiple spectral bands and a simple shortwave scheme suitable for climate and weather applications. Cloud effects and surface fluxes are included.

WRF-Var System

- WRF-Var merged into WRF software framework.
- Incremental formulation of the model-space cost function.
- Quasi-Newton or conjugate gradient minimization algorithms.
- Analysis increments on unstaggered Arakawa-A grid.
- Representation of the horizontal component of background error **B** via recursive filters (regional) or power spectra (global). The vertical component is applied through projection onto climatologically-averaged eigenvectors of vertical error. Horizontal/vertical errors are non-separable (horizontal scales vary with vertical eigenvector).
- Background cost function (J_b) preconditioning via a control variable transform U defined as $\mathbf{B} = \mathrm{U}\mathrm{U}^T$.
- Flexible choice of background error model and control variables.
- Climatological background error covariances estimated via either the NMC-method of averaged forecast differences or suitably averaged ensemble perturbations.
- Unified 3D-Var (4D-Var under development), global and regional, multi-model capability.

WRF-Chem

- Online (or "inline") model, in which the model is consistent with all conservative transport done by the meteorology model.
- Dry deposition, coupled with the soil/vegetation scheme.
- Aqueous phase chemistry coupled to some of the microphysics and aerosol schemes.
- Three choices for biogenic emissions: No biogenic emissions; Online calculation of biogenic emissions; Online modification of user specified biogenic emissions (e.g., EPA Biogenic Emissions Inventory System (BEIS)).
- Two choices for anthropogenic emissions: No anthropogenic emissions and user-specified anthropogenic emissions.
- Two choices for gas-phase chemical reaction calculations: RADM2 chemical mechanism and CBM-Z mechanism.
- Several choices for gas-phase chemical reaction calculations through the use of the Kinetic Pre-Processor (KPP).

- Three choices for photolysis schemes: Madronich scheme coupled with hydrometeors, aerosols, and convective parameterizations; Fast-J Photolysis scheme coupled with hydrometeors, aerosols, and convective parameterizations; FTUV scheme scheme coupled with hydrometeors, aerosols, and convective parameterizations.
- Choices for aerosol schemes: The Modal Aerosol Dynamics Model for Europe (MADE/SORGAM); Model for Simulating Aerosol Interactions and Chemistry (MOSAIC); and The GOCART aerosol model (experimental).
- A tracer transport option in which the chemical mechanism, deposition, etc., has been turned off.

WRF Software Framework

- Highly modular, single-source code for maintainability.
- Two-level domain decomposition for parallel and shared-memory generality.
- Portable across a range of available computing platforms.
- Support for multiple dynamics solvers and physics modules.
- Separation of scientific codes from parallelization and other architecture-specific issues.
- Input/Output Application Program Interface (API) enabling various external packages to be installed with WRF, thus allowing WRF to easily support various data formats.
- Efficient execution on a range of computing platforms (distributed and shared memory, vector and scalar types). Support for accelerators (e.g., GPUs).
- Use of Earth System Modeling Framework (ESMF) and interoperable as an ESMF component.
- Model coupling API enabling WRF to be coupled with other models such as ocean, and land models using ESMF, MCT, or MCEL.

Chapter 2

Governing Equations

The ARW dynamics solver integrates the compressible, nonhydrostatic Euler equations. The equations are cast in flux form using variables that have conservation properties, following the philosophy of Ooyama (1990). The equations are formulated using a terrain-following mass vertical coordinate (Laprise, 1992). In this chapter we define the vertical coordinate and present the flux form equations in Cartesian space, we extend the equations to include the effects of moisture in the atmosphere, and we further augment the equations to include projections to the sphere.

2.1   Vertical Coordinate and Variables

The ARW equations are formulated using a terrain-following hydrostatic-pressure vertical coordinate denoted by η and defined as

$$\eta = (p_h - p_{ht})/\mu \qquad \text{where} \quad \mu = p_{hs} - p_{ht}. \quad (2.1)$$

p_h is the hydrostatic component of the pressure, and p_{hs} and p_{ht} refer to values along the surface and top boundaries, respectively. The coordinate definition (2.1), proposed by Laprise (1992), is the traditional σ coordinate used in many hydrostatic atmospheric models. η varies from a value of 1 at the surface to 0 at the upper boundary of the model domain (Fig. 2.1). This vertical coordinate is also called a mass vertical coordinate.

Since $\mu(x, y)$ represents the mass per unit area within the column in the model domain at (x, y), the appropriate flux form variables are

$$\mathbf{V} = \mu\mathbf{v} = (U, V, W), \quad \Omega = \mu\dot{\eta}, \quad \Theta = \mu\theta. \quad (2.2)$$

$\mathbf{v} = (u, v, w)$ are the covariant velocities in the two horizontal and vertical directions, respectively, while $\omega = \dot{\eta}$ is the contravariant 'vertical'

Figure 2.1: ARW η coordinate.

7
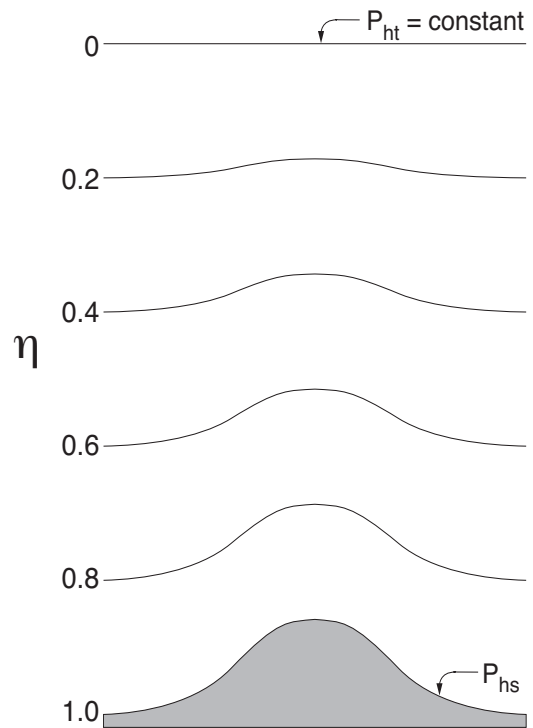
velocity. θ is the potential temperature. Also appearing in the governing equations of the ARW are the non-conserved variables $\phi = gz$ (the geopotential), p (pressure), and $\alpha = 1/\rho$ (the inverse density).

2.2 Flux-Form Euler Equations

Using the variables defined above, the flux-form Euler equations can be written as

$$\partial_t U + (\nabla \cdot \mathbf{V} u) - \partial_x(p\phi_\eta) + \partial_\eta(p\phi_x) = F_U \tag{2.3}$$
$$\partial_t V + (\nabla \cdot \mathbf{V} v) - \partial_y(p\phi_\eta) + \partial_\eta(p\phi_y) = F_V \tag{2.4}$$
$$\partial_t W + (\nabla \cdot \mathbf{V} w) - g(\partial_\eta p - \mu) = F_W \tag{2.5}$$
$$\partial_t \Theta + (\nabla \cdot \mathbf{V} \theta) = F_\Theta \tag{2.6}$$
$$\partial_t \mu + (\nabla \cdot \mathbf{V}) = 0 \tag{2.7}$$
$$\partial_t \phi + \mu^{-1}[(\mathbf{V} \cdot \nabla \phi) - gW] = 0 \tag{2.8}$$

along with the diagnostic relation for the inverse density

$$\partial_\eta \phi = -\alpha\mu, \tag{2.9}$$

and the equation of state

$$p = p_0(R_d\theta/p_0\alpha)^\gamma. \tag{2.10}$$

In $(2.3) - (2.10)$, the subscripts x, y and η denote differentiation,

$$\nabla \cdot \mathbf{V} a = \partial_x(Ua) + \partial_y(Va) + \partial_\eta(\Omega a),$$

and

$$\mathbf{V} \cdot \nabla a = U\partial_x a + V\partial_y a + \Omega\partial_\eta a,$$

where a represents a generic variable. $\gamma = c_p/c_v = 1.4$ is the ratio of the heat capacities for dry air, R_d is the gas constant for dry air, and p_0 is a reference pressure (typically 10^5 Pascals). The right-hand-side (RHS) terms F_U, F_V, F_W, and F_Θ represent forcing terms arising from model physics, turbulent mixing, spherical projections, and the earth's rotation.

The prognostic equations $(2.3) - (2.8)$ are cast in conservative form except for (2.8) which is the material derivative of the definition of the geopotential. (2.8) could be cast in flux form but we find no advantage in doing so since $\mu\phi$ is not a conserved quantity. We could also use a prognostic pressure equation in place of (2.8) (see Laprise, 1992), but pressure is not a conserved variable and we could not use a pressure equation together with the conservation equation for Θ (2.6) because they are linearly dependent. Additionally, prognostic pressure equations have the disadvantage of possessing a mass divergence term multiplied by a large coefficient (proportional to the sound speed) which makes spatial and temporal discretization problematic. It should be noted that the relation for the hydrostatic balance (2.9) does not represent a constraint on the solution, rather it is a diagnostic relation that formally is part of the coordinate definition. In the hydrostatic counterpart to the nonhydrostatic equations, (2.9) replaces the vertical momentum equation (2.5) and it becomes a constraint on the solution.

2.3 Inclusion of Moisture

In formulating the moist Euler equations, we retain the coupling of dry air mass to the prognostic variables, and we retain the conservation equation for dry air (2.7), as opposed to coupling the variables to the full (moist) air mass and hence introducing source terms in the mass conservation equation (2.7). Additionally, we define the coordinate with respect to the dry-air mass. Based on these principles, the vertical coordinate can be written as

$$\eta = (p_{dh} - p_{dht})/\mu_d \tag{2.11}$$

where μ_d represents the mass of the dry air in the column and p_{dh} and p_{dht} represent the hydrostatic pressure of the dry atmosphere and the hydrostatic pressure at the top of the dry atmosphere. The coupled variables are defined as

$$\mathbf{V} = \mu_d\mathbf{v}, \quad \Omega = \mu_d\dot{\eta}, \quad \Theta = \mu_d\theta. \tag{2.12}$$

With these definitions, the moist Euler equations can be written as

$$\partial_t U + (\nabla \cdot \mathbf{V}u) + \mu_d\alpha\partial_x p + (\alpha/\alpha_d)\partial_\eta p\partial_x\phi = F_U \tag{2.13}$$
$$\partial_t V + (\nabla \cdot \mathbf{V}v) + \mu_d\alpha\partial_y p + (\alpha/\alpha_d)\partial_\eta p\partial_y\phi = F_V \tag{2.14}$$
$$\partial_t W + (\nabla \cdot \mathbf{V}w) - g[(\alpha/\alpha_d)\partial_\eta p - \mu_d] = F_W \tag{2.15}$$
$$\partial_t \Theta + (\nabla \cdot \mathbf{V}\theta) = F_\Theta \tag{2.16}$$
$$\partial_t \mu_d + (\nabla \cdot \mathbf{V}) = 0 \tag{2.17}$$
$$\partial_t \phi + \mu_d^{-1}[(\mathbf{V} \cdot \nabla\phi) - gW] = 0 \tag{2.18}$$
$$\partial_t Q_m + (\nabla \cdot \mathbf{V}q_m) = F_{Q_m} \tag{2.19}$$

with the diagnostic equation for dry inverse density

$$\partial_\eta \phi = -\alpha_d\mu_d \tag{2.20}$$

and the diagnostic relation for the full pressure (vapor plus dry air)

$$p = p_0(R_d\theta_m/p_0\alpha_d)^\gamma \tag{2.21}$$

In these equations, α_d is the inverse density of the dry air $(1/\rho_d)$ and α is the inverse density taking into account the full parcel density $\alpha = \alpha_d(1 + q_v + q_c + q_r + q_i + ...)^{-1}$ where q_* are the mixing ratios (mass per mass of dry air) for water vapor, cloud, rain, ice, etc. Additionally, $\theta_m = \theta(1 + (R_v/R_d)q_v) \approx \theta(1 + 1.61q_v)$, and $Q_m = \mu_d q_m$; $q_m = q_v, q_c, q_i, ...$.

2.4 Map Projections, Coriolis and Curvature Terms

The ARW solver currently supports four projections to the sphere— the Lambert conformal, polar stereographic, Mercator, and latitude-longitude projections. These projections are described in Haltiner and Williams (1980). The transformation is isotropic for three of these projections – the Lambert conformal, polar stereographic, and Mercator grids. An isotropic

transformation requires $(\Delta x/\Delta y)|_{earth} = $ constant everywhere on the grid. Only isotropic transformations were supported in the previous ARW releases. Starting with the ARWV3 release, we now support anisotropic projections, in this case the latitude-longitude grid, and with it the full latitude-longitude global model. The ARW implements the projections using map factors, and the generalization to anisotropic transformations introduced in ARW V3 requires that there be map factors for both the x and y components of the transformation from computational to physical space in order to accomodate the anisotropy.

In the ARW's computational space, Δx and Δy are constants. Orthogonal projections to the sphere require that the physical distances between grid points in the projection vary with position on the grid. To transform the governing equations, map scale factors m_x and m_y are defined as the ratio of the distance in computational space to the corresponding distance on the earth's surface:

$$(m_x, m_y) = \frac{(\Delta x, \Delta y)}{\text{distance on the earth}}. \tag{2.22}$$

The ARW solver includes the map-scale factors in the governing equations by redefining the momentum variables as

$$U = \mu_d u/m_y, \quad V = \mu_d v/m_x, \quad W = \mu_d w/m_y, \quad \Omega = \mu_d \dot{\eta}/m_y.$$

Using these redefined momentum variables, the governing equations, including map factors and rotational terms, can be written as

$$\partial_t U + m_x[\partial_x(Uu) + \partial_y(Vu)]$$
$$+ \quad \partial_\eta(\Omega u) + (m_x/m_y)[\mu_d \alpha \partial_x p + (\alpha/\alpha_d)\partial_\eta p \partial_x \phi] = F_U \tag{2.23}$$
$$\partial_t V + m_y[\partial_x(Uv) + \partial_y(Vv)]$$
$$+ (m_y/m_x)\partial_\eta(\Omega v) + (m_y/m_x)[\mu_d \alpha \partial_y p + (\alpha/\alpha_d)\partial_\eta p \partial_y \phi] = F_V \tag{2.24}$$
$$\partial_t W + (m_x m_y/m_y)[\partial_x(Uw) + \partial_y(Vw)] + \partial_\eta(\Omega w) - m_y^{-1}g[(\alpha/\alpha_d)\partial_\eta p - \mu_d] = F_W \tag{2.25}$$
$$\partial_t \Theta + m_x m_y[\partial_x(U\theta) + \partial_y(V\theta)] + m_y\partial_\eta(\Omega\theta) = F_\Theta \tag{2.26}$$
$$\partial_t \mu_d + m_x m_y[U_x + V_y] + m_y\partial_\eta(\Omega) = 0 \tag{2.27}$$
$$\partial_t \phi + \mu_d^{-1}[m_x m_y(U\partial_x\phi + V\partial_y\phi) + m_y\Omega\partial_\eta\phi - m_y gW] = 0 \tag{2.28}$$
$$\partial_t Q_m + m_x m_y \partial_x(Uq_m) + \partial_y(Vq_m)] + m_y\partial_\eta(\Omega q_m) = F_{Q_m}, \tag{2.29}$$

and, for completeness, the diagnostic relation for the dry inverse density

$$\partial_\eta \phi = -\alpha_d \mu_d, \tag{2.30}$$

and the diagnostic equation for full pressure (vapor plus dry air)

$$p = p_0(R_d\theta_m/p_0\alpha_d)^\gamma. \tag{2.31}$$

The right-hand-side terms of the momentum equations (2.23) – (2.25) contain the Coriolis and curvature terms along with mixing terms and physical forcings. For the isotropic projections (Lambert conformal, polar stereographic, and Mercator), where $m_x = m_y = m$, the Coriolis and

curvature terms are cast in the following form:

$$F_{U_{cor}} = + \left(f + u\frac{\partial m}{\partial y} - v\frac{\partial m}{\partial x} \right) V - eW \cos\alpha_r - \frac{uW}{r_e} \tag{2.32}$$

$$F_{V_{cor}} = - \left(f + u\frac{\partial m}{\partial y} - v\frac{\partial m}{\partial x} \right) U + eW \sin\alpha_r - \frac{vW}{r_e} \tag{2.33}$$

$$F_{W_{cor}} = +e(U \cos\alpha_r - V \sin\alpha_r) + \left(\frac{uU + vV}{r_e} \right), \tag{2.34}$$

where α_r is the local rotation angle between the y-axis and the meridians, ψ is the latitude, $f = 2\Omega_e \sin\psi$, $e = 2\Omega_e \cos\psi$, Ω_e is the angular rotation rate of the earth, and r_e is the radius of the earth. In this formulation we have approximated the radial distance from the center of the earth as the mean earth radius r_e, and we have not taken into account the change in horizontal grid distance as a function of the radius. The terms containing m are the horizontal curvature terms, those containing r_e relate to vertical (earth-surface) curvature, and those with e and f are the Coriolis force.

The curvature and Coriolis terms for the momentum equations are cast in the following form for the anisotropic latitude-longitude grid:

$$F_{U_{cor}} = \frac{m_x}{m_y}\left[fV + \frac{uV}{r_e}\tan\psi \right] - \frac{uW}{r_e} - eW\cos\alpha_r \tag{2.35}$$

$$F_{V_{cor}} = \frac{m_y}{m_x}\left[-fU - \frac{uU}{r_e}\tan\psi - \frac{vW}{r_e} + eW\sin\alpha_r \right] \tag{2.36}$$

$$F_{W_{cor}} = +e(U\cos\alpha_r - (m_x/m_y)V\sin\alpha_r) + \left(\frac{uU + (m_x/m_y)vV}{r_e} \right), \tag{2.37}$$

For idealized cases on a Cartesian grid, the map scale factor $m_x = m_y = 1$, f is specified, and e and r_e^{-1} should be zero to remove the curvature terms.

2.5   Perturbation Form of the Governing Equations

Before constructing the discrete solver, it is advantageous to recast the governing equations using perturbation variables to reduce truncation errors in the horizontal pressure gradient calculations in the discrete solver and machine rounding errors in the vertical pressure gradient and buoyancy calculations. For this purpose, new variables are defined as perturbations from a hydrostatically-balanced reference state, and we define reference state variables (denoted by overbars) that are a function of height only and that satisfy the governing equations for an atmosphere at rest. That is, the reference state is in hydrostatic balance and is strictly only a function of $\bar{z}$. In this manner, $p = \bar{p}(\bar{z}) + p'$, $\phi = \bar{\phi}(\bar{z}) + \phi'$, $\alpha = \bar{\alpha}_d(\bar{z}) + \alpha'_d$, and $\mu_d = \bar{\mu}_d(x, y) + \mu'_d$. Because the η coordinate surfaces are generally not horizontal, the reference profiles $\bar{p}$, $\bar{\phi}$, and $\bar{\alpha}$ are functions of (x, y, η). The hydrostatically balanced portion of the pressure gradients in the reference sounding can be removed without approximation to the equations using these

perturbation variables. The momentum equations $(2.23) - (2.25)$ are written as

$$\partial_t U + m_x \left[\partial_x(Uu) + \partial_y(Vu)\right] + \partial_\eta(\Omega u)$$
$$+ (m_x/m_y)(\alpha/\alpha_d)\left[\mu_d(\partial_x\phi' + \alpha_d\partial_x p' + \alpha'_d\partial_x\overline{p}) + \partial_x\phi(\partial_\eta p' - \mu'_d)\right] = F_U \qquad (2.38)$$
$$\partial_t V + m_y\left[\partial_x(Uv) + \partial_y(Vv)\right] + (m_y/m_x)\partial_\eta(\Omega v)$$
$$+ (m_x/m_y)(\alpha/\alpha_d)\left[\mu_d(\partial_x\phi' + \alpha_d\partial_x p' + \alpha'_d\partial_x\overline{p}) + \partial_x\phi(\partial_\eta p' - \mu'_d)\right] = F_U \qquad (2.39)$$
$$\partial_t W + (m_x m_y/m_y)[\partial_x(Uw) + \partial_y(Vw)] + \partial_\eta(\Omega w)$$
$$- m_y^{-1}g(\alpha/\alpha_d)[\partial_\eta p' - \bar{\mu}_d(q_v + q_c + q_r)] + m_y^{-1}\mu'_d g = F_W, \qquad (2.40)$$

and the mass conservation equation (2.27) and geopotential equation (2.28) become

$$\partial_t\mu'_d + m_x m_y[\partial_x U + \partial_y V] + m_y\partial_\eta\Omega = 0 \qquad (2.41)$$
$$\partial_t\phi' + \mu_d^{-1}[m_x m_y(U\partial_x\phi + V\partial_y\phi) + m_y\Omega\partial_\eta\phi - m_y gW] = 0. \qquad (2.42)$$

Remaining unchanged are the conservation equations for the potential temperature and scalars

$$\partial_t\Theta + m_x m_y[\partial_x(U\theta) + \partial_y(V\theta)] + m_y\partial_\eta(\Omega\theta) = F_\Theta \qquad (2.43)$$
$$\partial_t Q_m + m_x m_y[\partial_x(Uq_m) + \partial_y(Vq_m)] + m_y\partial_\eta(\Omega q_m) = F_{Q_m}. \qquad (2.44)$$

In the perturbation system the hydrostatic relation (2.30) becomes

$$\partial_\eta\phi' = -\bar{\mu}_d\alpha'_d - \alpha_d\mu'_d. \qquad (2.45)$$

Equations $(2.38) - (2.44)$, together with the equation of state (2.21), represent the equations solved in the ARW. The RHS terms in these equations include the Coriolis terms $(2.32) - (2.34)$, mixing terms (described in Chapter 4), and parameterized physics (described in Chapter 8). Also note that the equation of state (2.21) cannot be written in perturbation form because of the exponent in the expression. For small perturbation simulations, accuracy for perturbation variables can be maintained by linearizing (2.21) for the perturbation variables.

Chapter 3

Model Discretization

3.1 Temporal Discretization

The ARW solver uses a time-split integration scheme. Generally speaking, slow or low-frequency (meteorologically significant) modes are integrated using a third-order Runge-Kutta (RK3) time integration scheme, while the high-frequency acoustic modes are integrated over smaller time steps to maintain numerical stability. The horizontally propagating acoustic modes (including the external mode present in the mass-coordinate equations using a constant-pressure upper boundary condition) and gravity waves are integrated using a forward-backward time integration scheme, and vertically propagating acoustic modes and buoyancy oscillations are integrated using a vertically implicit scheme (using the acoustic time step). The time-split integration for the flux-form equations is described and analyzed in Klemp et al. (2007). The time-splitting is similar to that first developed by Klemp and Wilhelmson (1978) for leapfrog time integration and analyzed by Skamarock and Klemp (1992). This time-split approach was extended to the RK3 scheme as described in Wicker and Skamarock (2002). The primary differences between the earlier implementations described in the references and the ARW implementation are associated with our use of the mass vertical coordinate and a flux-form set of equations, as described in Klemp et al. (2007), along with our use of perturbation variables for the acoustic component of the time-split integration. The acoustic-mode integration is cast in the form of a correction to the RK3 integration.

3.1.1 Runge-Kutta Time Integration Scheme

The RK3 scheme, described in Wicker and Skamarock (2002), integrates a set of ordinary differential equations using a predictor-corrector formulation. Defining the prognostic variables in the ARW solver as $\Phi = (U, V, W, \Theta, \phi', \mu', Q_m)$ and the model equations as $\Phi_t = R(\Phi)$, the RK3 integration takes the form of 3 steps to advance a solution $\Phi(t)$ to $\Phi(t + \Delta t)$:

$$\Phi^* = \Phi^t + \frac{\Delta t}{3} R(\Phi^t) \tag{3.1}$$

$$\Phi^{**} = \Phi^t + \frac{\Delta t}{2} R(\Phi^*) \tag{3.2}$$

$$\Phi^{t+\Delta t} = \Phi^t + \Delta t R(\Phi^{**}) \tag{3.3}$$

where Δt is the time step for the low-frequency modes (the model time step). In (3.1) – (3.3), superscripts denote time levels. This scheme is not a true Runge-Kutta scheme *per se* because, while it is third-order accurate for linear equations, it is only second-order accurate for nonlinear equations. With respect to the ARW equations, the time derivatives Φ_t are the partial time derivatives (the leftmost terms) in equations (2.38) – (2.44), and $R(\Phi)$ are the remaining terms in (2.38) – (2.44).

3.1.2 Acoustic Integration

The high-frequency but meteorologically insignificant acoustic modes would severely limit the RK3 time step Δt in (3.1) – (3.3). To circumvent this time step limitation we use the time-split approach described in Wicker and Skamarock (2002). Additionally, to increase the accuracy of the splitting, we integrate a perturbation form of the governing equations using smaller acoustic time steps within the RK3 large-time-step sequence. To form the perturbation equations for the RK3 time-split acoustic integration, we define small time step variables that are deviations from the most recent RK3 predictor (denoted by the superscript t^* and representing either Φ^t, Φ^*, or Φ^{**} in (3.1) – (3.3)):

$$\mathbf{V}'' = \mathbf{V} - \mathbf{V}^{t^*}, \qquad \Omega'' = \Omega - \Omega^{t^*}, \qquad \Theta'' = \Theta - \Theta^{t^*},$$
$$\phi'' = \phi' - \phi'^{t^*}, \qquad \alpha_d'' = \alpha_d' - \alpha_d'^{t^*}, \qquad \mu_d'' = \mu_d' - \mu_d'^{t^*}.$$

The hydrostatic relation (i.e., the vertical coordinate definition) becomes

$$\alpha_d'' = -\frac{1}{\mu_d^{t^*}}\left(\partial_\eta \phi'' + \alpha_d^{t^*}\mu_d''\right). \tag{3.4}$$

Additionally, we also introduce a version of the equation of state that is linearized about t^*,

$$p'' = \frac{c_s^2}{\alpha_d^{t^*}}\left(\frac{\Theta''}{\Theta^{t^*}} - \frac{\alpha_d''}{\alpha_d^{t^*}} - \frac{\mu_d''}{\mu_d^{t^*}}\right), \tag{3.5}$$

where $c_s^2 = \gamma p^{t^*}\alpha_d^{t^*}$ is the square of the sound speed. The linearized state equation (3.5) and the vertical coordinate definition (3.4) are used to cast the vertical pressure gradient in (2.40) in terms of the model's prognostic variables. By combining (3.5) and (3.4), the vertical pressure gradient can be expressed as

$$\partial_\eta p'' = \partial_\eta(C\partial_\eta \phi'') + \partial_\eta\left(\frac{c_s^2}{\alpha_d^{t^*}}\frac{\Theta''}{\Theta^{t^*}}\right), \tag{3.6}$$

where $C = c_s^2/\mu^{t^*}\alpha_d^{t^* \, 2}$. This linearization about the most recent large time step should be highly accurate over the time interval of the several small time steps.

These variables along with (3.6) are substituted into the prognostic equations (2.38) – (2.44)

14

and lead to the acoustic time-step equations:

$$\partial_t U'' + (m_x/m_y)(\alpha^{t^*}/\alpha_d^{t^*}) \left[\mu_d^{t^*} \left(\alpha_d^{t^*} \partial_x p''^\tau + \alpha_d''^\tau \partial_x \overline{p} + \partial_x \phi''^\tau \right) + \partial_x \phi^{t^*} \left(\partial_\eta p'' - \mu_d'' \right)^\tau \right] = R_U^{t^*} \tag{3.7}$$

$$\partial_t V'' + (m_y/m_x)(\alpha^{t^*}/\alpha_d^{t^*}) \left[\mu_d^{t^*} \left(\alpha_d^{t^*} \partial_y p''^\tau + \alpha_d''^\tau \partial_y \overline{p} + \partial_y \phi''^\tau \right) + \partial_y \phi^{t^*} \left(\partial_\eta p'' - \mu_d'' \right)^\tau \right] = R_V^{t^*} \tag{3.8}$$

$$\delta_\tau \mu_d'' + m_x m_y [\partial_x U'' + \partial_y V'']^{\tau+\Delta\tau} + m_y \partial_\eta \Omega''^{\tau+\Delta\tau} = R_\mu{}^{t^*} \tag{3.9}$$

$$\delta_\tau \Theta'' + m_x m_y [\partial_x (U'' \theta^{t^*}) + \partial_y (V'' \theta^{t^*})]^{\tau+\Delta\tau} + m_y \partial_\eta (\Omega''^{\tau+\Delta\tau} \theta^{t^*}) = R_\Theta{}^{t^*} \tag{3.10}$$

$$\delta_\tau W'' - m_y^{-1} g \overline{\left\{ (\alpha/\alpha_d)^{t^*} \left[\partial_\eta (C \partial_\eta \phi'') + \partial_\eta \left(\frac{c_s^2}{\alpha^{t^*}} \frac{\Theta''}{\Theta^{t^*}} \right) \right] - \mu_d'' \right\}}^\tau = R_W{}^{t^*} \tag{3.11}$$

$$\delta_\tau \phi'' + \frac{1}{\mu_d^{t^*}} [m_y \Omega''^{\tau+\Delta\tau} \delta_\eta \phi^{t^*} - m_y \overline{g W''}^\tau] = R_\phi{}^{t^*}. \tag{3.12}$$

The RHS terms in (3.7) – (3.12) are fixed for the acoustic steps that comprise the time integration of each RK3 sub-step (i.e., (3.1) – (3.3)), and are given by

$$R_U^{t^*} = - m_x \left[\partial_x (Uu) + \partial_y (Vu) \right] - \partial_\eta (\Omega u)$$
$$\quad - (m_x/m_y)(\alpha/\alpha_d) \left[\mu_d (\partial_x \phi' + \alpha_d \partial_x p' + \alpha_d' \partial_x \overline{p}) + \partial_x \phi (\partial_\eta p' - \mu_d') \right] \tag{3.13}$$

$$R_V^{t^*} = - m_y \left[\partial_x (Uv) + \partial_y (Vv) \right] - (m_y/m_x) \partial_\eta (\Omega v)$$
$$\quad - (m_y/m_x)(\alpha/\alpha_d) \left[\mu_d (\partial_y \phi' + \alpha_d \partial_y p' + \alpha_d' \partial_y \overline{p}) + \partial_y \phi (\partial_\eta p' - \mu_d') \right] \tag{3.14}$$

$$R_{\mu_d}^{t^*} = - m_x m_y [\partial_x U + \partial_y V] - m_y \partial_\eta \Omega \tag{3.15}$$

$$R_\Theta^{t^*} = - m_x m_y [\partial_x (U\theta) + \partial_y (V\theta)] - m_y \partial_\eta (\Omega \theta) + F_\Theta \tag{3.16}$$

$$R_W^{t^*} = - (m_x m_y/m_y)[\partial_x (Uw) + \partial_y (Vw)] - \partial_\eta (\Omega w)$$
$$\quad + m_y^{-1} g (\alpha/\alpha_d)[\partial_\eta p' - \overline{\mu}_d (q_v + q_c + q_r)] - m_y^{-1} \mu_d' g + F_W \tag{3.17}$$

$$R_\phi^{t^*} = - \mu_d^{-1} [m_x m_y (U \partial_x \phi + V \partial_y \phi) + m_y \Omega \partial_\eta \phi - m_y g W], \tag{3.18}$$

where all variables in (3.13) – (3.18) are evaluated at time t^* (i.e., using Φ^t, Φ^*, or Φ^{**} for the appropriate RK3 sub-step in (3.1) – (3.3)). Equations (3.7) – (3.12) utilize the discrete acoustic time-step operator

$$\delta_\tau a = \frac{a^{\tau+\Delta\tau} - a^\tau}{\Delta\tau},$$

where $\Delta\tau$ is the acoustic time step, and an acoustic time-step averaging operator

$$\overline{a}^\tau = \frac{1+\beta}{2} a^{\tau+\Delta\tau} + \frac{1-\beta}{2} a^\tau, \tag{3.19}$$

where β is a user-specified parameter (see Section 4.3.3).

The integration over the acoustic time steps proceeds as follows. Beginning with the small time-step variables at time τ, (3.7) and (3.8) are stepped forward to obtain $U''^{\tau+\Delta\tau}$ and $V''^{\tau+\Delta\tau}$. Both $\mu''^{\tau+\Delta\tau}$ and $\Omega''^{\tau+\Delta\tau}$ are then calculated from (3.9). This is accomplished by first integrating (3.9) vertically from the surface to the material surface at the top of the domain, which removes the $\partial_\eta \Omega''$ term such that

$$\delta_\tau \mu_d = m_x m_y \int_1^0 [\partial_x U'' + \partial_y V'']^{\tau+\Delta\tau} d\eta. \tag{3.20}$$

15

After computing $\mu_d''^{\tau+\Delta\tau}$ from (3.20), $\Omega''^{\tau+\Delta\tau}$ is recovered by using (3.9) to integrate the $\partial_\eta\Omega''$ term vertically using the lower boundary condition $\Omega'' = 0$ at the surface. Equation (3.10) is then stepped forward to calculate $\Theta''^{\tau+\Delta\tau}$. Equations (3.11) and (3.12) are combined to form a vertically implicit equation that is solved for $W''^{\tau+\Delta\tau}$ subject to the boundary condition $\Omega = \Omega'' = 0$ at the surface ($z = h(x,y)$) and $p' = 0$ along the model top. $\phi''^{\tau+\Delta\tau}$ is then obtained from (3.12), and $p''^{\tau+\Delta\tau}$ and $\alpha_d''^{\tau+\Delta\tau}$ are recovered from (3.5) and (3.4).

Begin Time Step

      Begin RK3 Loop: Steps 1, 2, and 3

          (1) If RK3 step 1, compute and store F_Φ
                (i.e., physics tendencies for RK3 step, including mixing).
          (2) Compute R^{t^*}, (3.13)–(3.18)

          Begin Acoustic Step Loop: Steps $1 \rightarrow n$,
            RK3 step 1, $n = 1$, $\Delta\tau = \Delta t/3$;
            RK3 step 2, $n = n_s/2$, $\Delta\tau = \Delta t/n_s$;
            RK3 step 3, $n = n_s$, $\Delta\tau = \Delta t/n_s$.

          (3) Advance horizontal momentum, (3.7) and (3.8)
             Global: Apply polar filter to $U''^{\tau+\Delta\tau}$ and $V''^{\tau+\Delta\tau}$.
          (4) Advance μ_d (3.9) and compute $\Omega''^{\tau+\Delta\tau}$ then advance Θ (3.10)
             Global: Apply polar filter to $\mu_d^{\tau+\Delta\tau}$ and $\Theta''^{\tau+\Delta\tau}$.
          (5) Advance W and ϕ (3.11) and (3.12)
             Global: Apply polar filter to $W''^{\tau+\Delta\tau}$ and $\phi''^{\tau+\Delta\tau}$.
          (6) Diagnose p'' and α'' using (3.5) and (3.4)

          End Acoustic Step Loop

          (7) Scalar transport: Advance scalars (2.44)
             over RK3 substep (3.1), (3.2) or (3.3)
             (using mass fluxes U, V and Ω time-averaged over the acoustic steps).
             Global: Apply polar filter to scalars.
          (8) Compute p' and α' using updated prognostic variables in (2.31) and (2.45)

      End RK3 Loop

      (9) Compute non-RK3 physics (currently microphysics), advance variables.
         Global: Apply polar filter to updated variables.

End Time Step

Figure 3.1: Time step integration sequence. Here n represents the number of acoustic time steps for a given substep of the RK3 integration, and n_s is the ratio of the RK3 time step to the acoustic time step for the second and third RK3 substeps.

16

3.1.3 Full Time-Split Integration Sequence

The time-split RK3 integration technique is summarized in Figure 3.1. It consists of two primary loops— an outer loop for the large-time-step Runge-Kutta integration, and an inner loop for the acoustic mode integration.

In the RK3 scheme, physics can be integrated within the RK3 time integration (using a time forward step, i.e., step (1) in Fig. 3.1, or the RK3 time integration if higher temporal accuracy is desired, i.e., in step (2)— implying a physics evaluation every RK3 substep) or external to it using additive timesplitting, i.e., step (9).

Within the acoustic integration, the acoustic time step $\Delta\tau$ is specified by the user through the choice of n_s (see Section 3.3.2). Within the first RK3 substep, however, a single acoustic time step is used to advance the solution regardless of n_s. Within the full RK3-acoustic timesplit integration, this modified acoustic time step does not impose any additional stability constraints (see Wicker and Skamarock, 2002).

The major costs in the model arise from the evaluation of the right hand side terms R^{t^*} in (3.7) – (3.12). The efficiency of the RK3 timesplit scheme arises from the fact that the RK3 time step Δt is much larger than the acoustic time step $\Delta\tau$, hence the most costly evaluations are only performed in the less-frequent RK3 steps.

3.1.4 Diabatic Forcing

Within the RK3 integration sequence outlined in Fig. 3.1, the RHS term $R_\Theta^{t^*}$ in the thermo-dynamic equation (3.10) contains contributions from the diabatic physics tendencies that are computed in step (1) at the beginning of the first RK3 step. This diabatic forcing is integrated within the acoustic steps (specifically, in step 4 in the time integration sequence shown in Fig. 3.1). Additional diabatic contributions are integrated in an additive-time-split manner in step (9) after the RK3 update is complete. Thus, the diabatic forcing computed in step (9) (the microphysics in the current release of the ARW) does not appear in $R_\Theta^{t^*}$ from (3.10) in the acoustic integration. We have discovered that this time splitting can excite acoustic waves and can give rise to noise in the solutions for some applications. Note that the non-RK3 physics are integrated in step (9) because balances produced in the physics are required at the end of the time step (e.g., the saturation adjustment in the microphysics). So while moving these non-RK3 physics into step (1) would eliminate the noise, the balances produced by these physics would be altered.

We have found that the excitation of the acoustic modes can be circumvented while leaving the non-RK3 physics in step (9) by using the following procedure that is implemented in the ARW. In step (1) of the integration procedure (Fig. 3.1), an estimate of the diabatic forcing of Θ arising from the non-RK3 physics in step (9) is included in the diabatic forcing term $R_\Theta^{t^*}$ in (3.10) (which is advanced in step 4). This estimated diabatic forcing is then removed from the updated Θ after the RK3 integration is complete and before the evaluation of the non-RK3 physics in step (9). We use the diabatic forcing from the previous time step as the estimated forcing; hence this procedure results in few additional computations outside of saving the diabatic forcing between time steps.

3.1.5 Hydrostatic Option

A hydrostatic option is available in the ARW solver. The time-split RK3 integration technique summarized in Fig. 3.1 is retained, including the acoustic step loop. Steps (5) and (6) in the acoustic-step loop, where W and ϕ are advanced and p'' and α'' are diagnosed, are replaced by the following three steps. (1) Diagnose the hydrostatic pressure using the definition of the vertical coordinate

$$\delta_\eta p_h = \frac{\alpha_d}{\alpha}\mu_d = \left(1 + \sum q_m\right)\mu_d.$$

(2) Diagnose α_d using the equation of state (2.31) and the prognosed θ. (3) Diagnose the geopotential using the hydrostatic equation

$$\delta_\eta \phi' = -\bar{\mu}_d \alpha'_d - \mu'_d \alpha_d.$$

The vertical velocity w can be diagnosed from the geopotential equation, but it is not needed in the solution procedure. The acoustic step loop advances gravity waves, including the external mode, and the Lamb wave when the hydrostatic option is used.

3.2 Spatial Discretization

The spatial discretization in the ARW solver uses a C grid staggering for the variables as shown in Fig. 3.2. That is, normal velocities are staggered one-half grid length from the thermo-dynamic variables. The variable indices, (i, j, k) indicate variable locations with $(x, y, \eta) = (i\Delta x, j\Delta y, k\Delta\eta)$. We will denote the points where θ is located as being *mass* points, and likewise we will denote locations where u, v, and w are defined as u points, v points, and w points, respectively. Not shown in Fig. 3.2 are the column mass μ, defined at the (i, j) points (mass points) on the discrete grid, the geopotential ϕ that is defined at the w points, and the moisture variables q_m are defined at the mass points. The diagnostic variables used in the model, the pressure p and inverse density α, are computed at mass points. The grid lengths Δx and Δy are constants in the model formulation; changes in the physical grid lengths associated with the various projections to the sphere are accounted for using the map factors introduced in Section 2.4. The vertical grid length $\Delta\eta$ is not a fixed constant; it is specified in the initialization. The user is free to specify the η values of the model levels subject to the constraint that $\eta = 1$ at the surface, $\eta = 0$ at the model top, and η decreases monotonically between the surface and model top. Using these grid and variable definitions, we can define the spatial discretization for the ARW solver.

3.2.1 Acoustic Step Equations

We begin by defining the column-mass-coupled variables relative to the uncoupled variables. The vertical velocity is staggered only in k, so it can be coupled directly to the column mass with no averaging or interpolation. The horizontal velocities are horizontally staggered relative to the column mass such that the continuous variables are represented discretely as

$$U = \frac{\mu_d u}{m_y} \rightarrow \frac{\overline{\mu_d}^x u}{\overline{m_y}^x}, \quad V = \frac{\mu_d v}{m_x} \rightarrow \frac{\overline{\mu_d}^y v}{\overline{m_x}^y},$$

18
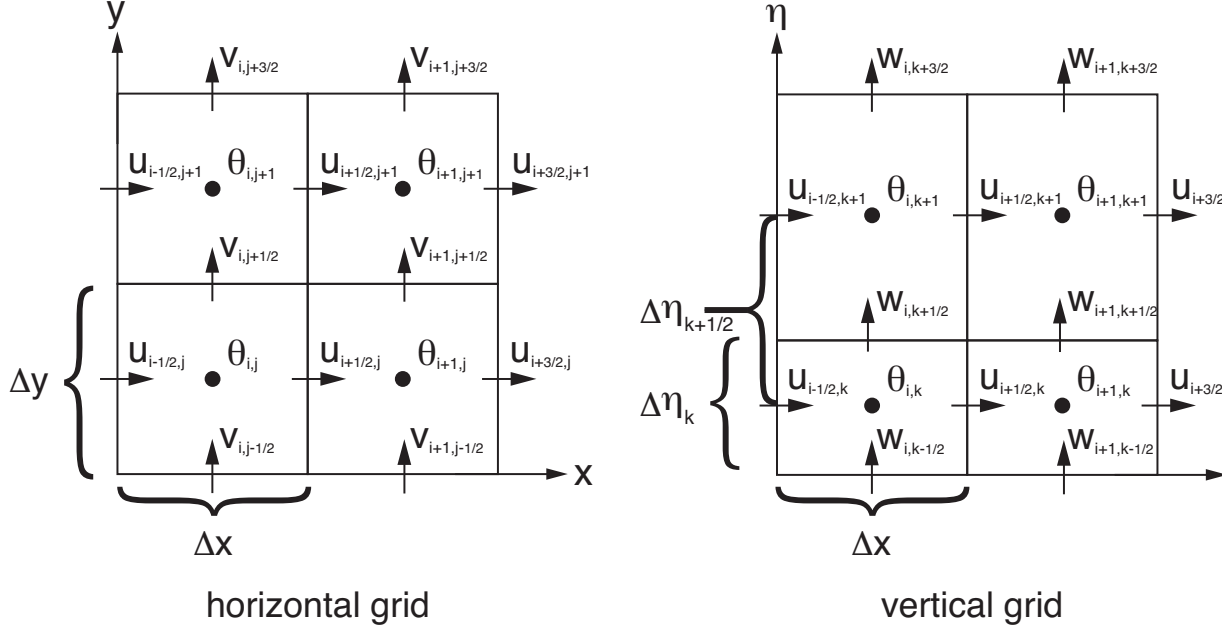
Figure 3.2: Horizontal and vertical grids of the ARW

where the discrete operator $\overline{a}^x$ denotes a linear interpolation operator. The grid lengths Δx and Δy are constant, hence in this case the operator reduces to $\overline{a}^x = (a_{i+1/2} + a_{i-1/2})/2$.

Using these definitions, we can write the spatially discrete acoustic step equations (3.7) – (3.12) as

$$\partial_t U'' + (m_x/m_y)\overline{(\alpha^{t^*}/\alpha_d^{t^*})}^x \left[\overline{\mu_d^{t^*}}^x \left(\overline{\alpha_d^{t^*}}^x \partial_x p''^\tau + \overline{\alpha_d''^\tau}^x \partial_x \overline{p} + \partial_x \overline{\phi''^\tau}^\eta\right)\right.$$
$$\left. + \partial_x \overline{\phi^{t^*}}^\eta \left(\partial_\eta \overline{\overline{p''}^x}^\eta - \overline{\mu_d''}^x\right)^\tau\right] = R_U^{t^*} \tag{3.21}$$

$$\partial_t V'' + (m_y/m_x)\overline{(\alpha^{t^*}/\alpha_d^{t^*})}^y \left[\overline{\mu_d^{t^*}}^y \left(\overline{\alpha_d^{t^*}}^y \partial_y p''^\tau + \overline{\alpha_d''^\tau}^y \partial_y \overline{p} + \partial_y \overline{\phi''^\tau}^\eta\right)\right.$$
$$\left. + \partial_y \overline{\phi^{t^*}}^\eta \left(\partial_\eta \overline{\overline{p''}^y}^\eta - \overline{\mu_d''}^y\right)^\tau\right] = R_V^{t^*} \tag{3.22}$$

$$\delta_\tau \mu_d'' + m_x m_y [\delta_x U'' + \delta_y V'']^{\tau+\Delta\tau} + m_y \delta_\eta \Omega''^{\tau+\Delta\tau} = R_\mu^{t^*} \tag{3.23}$$

$$\delta_\tau \Theta'' + m_x m_y [\delta_x(U''\overline{\theta^{t^*}}^x) + \delta_y(V''\overline{\theta^{t^*}}^y)]^{\tau+\Delta\tau} + m_y \delta_\eta(\Omega''^{\tau+\Delta\tau}\overline{\theta^{t^*}}) = R_\Theta^{t^*} \tag{3.24}$$

$$\delta_\tau W'' - m_y^{-1}g\overline{\left\{\overline{(\alpha/\alpha_d)^{t^*}}^\eta \left[\delta_\eta(C\delta_\eta \phi'') + \delta_\eta\left(\frac{c_s^2}{\alpha^{t^*}}\frac{\Theta''}{\Theta^{t^*}}\right)\right] - \mu_d''\right\}}^\tau = R_W^{t^*} \tag{3.25}$$

$$\delta_\tau \phi'' + \frac{1}{\mu_d^{t^*}}[m_y\Omega''^{\tau+\Delta\tau}\delta_\eta\overline{\phi^{t^*}}^\eta - m_y\overline{gW''}^\tau] = R_\phi^{t^*}, \tag{3.26}$$

where the discrete operator

$$\delta_x a = \Delta x^{-1}(a_{i+1/2} - a_{i-1/2}) \tag{3.27}$$

with the operators δ_y and δ_η similarly defined. Additionally, the operator $\overline{a}^\eta$ is a vertical interpolation operator. Using the notation given for the vertically stretched grid depicted in

19

Fig. 3.2, it is defined as

$$\overline{a}^\eta|_{k+1/2} = \frac{1}{2}\left(\frac{\Delta\eta_k}{\Delta\eta_{k+1/2}}a_{k+1} + \frac{\Delta\eta_{k+1}}{\Delta\eta_{k+1/2}}a_k\right). \tag{3.28}$$

This operator vertically interpolates variables on mass levels k to the w levels $(k+\frac{1}{2})$. It should be noted that the vertical grid is defined such that vertical interpolation from w levels to mass levels reduces to $\overline{a}^\eta_k = (a_{k+1/2} + a_{k-1/2})/2$ (see Fig. 3.2).

The RHS terms in the discrete acoustic step equations for momentum (3.21), (3.22) and (3.25) are discretized as

$$R_U^{t*} = -(m_x/m_y)\overline{(\alpha/\alpha_d)}^x\left[\overline{\mu_d}^x(\partial_x\overline{\phi'}^\eta + \overline{\alpha_d}^x\partial_x p' + \overline{\alpha_d'}^x\partial_x\overline{p}) + \partial_x\overline{\phi}^\eta(\partial_\eta\overline{\overline{p'}^x}^\eta - \overline{\mu_d'}^x)\right]$$
$$+ F_{U_{cor}} + \text{advection} + \text{mixing} + \text{physics}, \tag{3.29}$$

$$R_V^{t*} = -(m_y/m_x)\overline{(\alpha/\alpha_d)}^y\left[\overline{\mu_d}^y(\partial_y\overline{\phi'}^\eta + \overline{\alpha_d}^y\partial_y p' + \overline{\alpha_d'}^y\partial_y\overline{p}) + \partial_y\overline{\phi}^\eta(\partial_\eta\overline{\overline{p'}^y}^\eta - \overline{\mu_d'}^y)\right]$$
$$+ F_{V_{cor}} + \text{advection} + \text{mixing} + \text{physics}, \tag{3.30}$$

$$R_W^{t*} = m_y^{-1}g\overline{(\alpha/\alpha_d)}^\eta[\delta_\eta p' + \overline{\mu}_d\overline{q_m}^\eta] - m_y^{-1}\mu_d'g$$
$$+ F_{W_{cor}} + \text{advection} + \text{mixing} + \text{buoyancy} + \text{physics}. \tag{3.31}$$

3.2.2 Coriolis and Curvature Terms

The terms $F_{U_{cor}}$, $F_{V_{cor}}$, and $F_{W_{cor}}$ in (3.29) – (3.31) represent Coriolis and curvature effects in the equations using the isotropic map projections (Lambert conformal, polar stereographic, and Mercator) where $m_x = m_y = m$. These terms in continuous form are given in (2.32) – (2.34). Their spatial discretization is

$$F_{U_{cor}} = +\left(\overline{f}^x + \overline{\overline{u}^x\delta_y m - \overline{v}^y\delta_x m}^x\right)\overline{V}^{xy} - \overline{e}^x\overline{W}^{x\eta}\overline{\cos\alpha_r}^x - \frac{u\overline{W}^{x\eta}}{r_e}, \tag{3.32}$$

$$F_{V_{cor}} = -\left(\overline{f}^y + \overline{\overline{u}^x\delta_y m - \overline{v}^y\delta_x m}^y\right)\overline{U}^{xy} + \overline{e}^y\overline{W}^{y\eta}\overline{\sin\alpha_r}^y - \frac{v\overline{W}^{y\eta}}{r_e}, \tag{3.33}$$

$$F_{W_{cor}} = +e(\overline{U}^{x\eta}\cos\alpha_r - \overline{V}^{y\eta}\sin\alpha_r) + \left(\frac{\overline{u}^{x\eta}\overline{U}^{x\eta} + \overline{v}^{y\eta}\overline{V}^{y\eta}}{r_e}\right). \tag{3.34}$$

Here the operators $\overline{()}^{xy} = \overline{\overline{()}^x}^y$, and likewise for $\overline{()}^{x\eta}$ and $\overline{()}^{y\eta}$.

For the non-isotropic latitude longitude projection, the Coriolis and curvature terms given in (2.35) and (2.36) are discretized as

$$F_{U_{cor}} = \frac{m_x}{m_y}\left[\overline{f}^x\overline{V}^{xy} + \frac{u\overline{V}^{xy}}{r_e}\tan\psi\right] - \overline{e}^x\overline{W}^{x\eta}\overline{\cos\alpha_r}^x - \frac{u\overline{W}^{x\eta}}{r_e}, \tag{3.35}$$

$$F_{V_{cor}} = \frac{m_y}{m_x}\left[-\overline{f}^y\overline{U}^{xy} - \frac{\overline{u}^{xy}\overline{U}^{xy}}{r_e}\tan\psi + \overline{e}^y\overline{W}^{y\eta}\overline{\sin\alpha_r}^y - \frac{v\overline{W}^{y\eta}}{r_e}\right], \tag{3.36}$$

$$F_{W_{cor}} = +e(\overline{U}^{x\eta}\cos\alpha_r - (m_x/m_y)\overline{V}^{y\eta}\sin\alpha_r) + \left(\frac{\overline{u}^{x\eta}\overline{U}^{x\eta} + (m_x/m_y)\overline{v}^{y\eta}\overline{V}^{y\eta}}{r_e}\right). \tag{3.37}$$

3.2.3 Advection

The advection terms in the ARW solver are in the form of a flux divergence and are a subset of the RHS terms in equations (3.13) – (3.18):

$$R_{U_{adv}}^{t^*} = -m_x[\partial_x(Uu) + \partial_y(Vu)] + \qquad \partial_\eta(\Omega u) \qquad (3.38)$$

$$R_{V_{adv}}^{t^*} = -m_y[\partial_x(Uv) + \partial_y(Vv)] + (m_x/m_y)\partial_\eta(\Omega v) \qquad (3.39)$$

$$R_{\mu_{adv}}^{t^*} = -m_x m_y[\partial_x U + \partial_y V] + m_y\partial_\eta\Omega \qquad (3.40)$$

$$R_{\Theta_{adv}}^{t^*} = -m_x m_y[\partial_x(U\theta) + \partial_y(V\theta)] - m_y\partial_\eta(\Omega\theta) \qquad (3.41)$$

$$R_{W_{adv}}^{t^*} = -(m_x m_y/m_y)[\partial_x(Uw) + \partial_y(Vw)] + \partial_\eta(\Omega w) \qquad (3.42)$$

$$R_{\phi_{adv}}^{t^*} = -\mu_d^{-1}[m_x m_y(U\partial_x\phi + V\partial_y\phi) + m_y\Omega\partial_\eta\phi]. \qquad (3.43)$$

For the mass conservation equation, the flux divergence is discretized using a 2nd-order centered approximation:

$$R_{\mu_{adv}}^{t^*} = -m_x m_y[\delta_x U + \delta_y V]^{t^*} + m_y\delta_\eta\Omega^{t^*}. \qquad (3.44)$$

In the current version of the ARW, the advection of vector quantities (momentum) and scalars is performed using the RK3 time integration as outlined in Fig. 3.1. The spatial discretization used in this approach is outlined in the next section. For many applications it is desirable to use positive definite or monotonic advection schemes for scalar transport.

RK3 Advection

2nd through 6th order accurate spatial discretizations of the flux divergence are available in the ARW for momentum, scalars and geopotential using the RK3 time-integration scheme (scalar advection option 1, step 7 in the time-split integration sequence in Fig. 3.1). The discrete operators can be illustrated by considering the flux divergence equation for a scalar q in its discrete form:

$$R_{q_{adv}}^{t^*} = -m_x m_y[\delta_x(U\overline{q}^{x_{adv}}) + \delta_y(V\overline{q}^{y_{adv}})] - m_y\delta_\eta(\Omega\overline{q}^{\eta_{adv}}). \qquad (3.45)$$

As in the pressure gradient discretization, the discrete operator is defined as

$$\delta_x(U\overline{q}^{x_{adv}}) = \Delta x^{-1}\big[(U\overline{q}^{x_{adv}})_{i+1/2} - (U\overline{q}^{x_{adv}})_{i-1/2}\big]. \qquad (3.46)$$

The different order advection schemes correspond to different definitions for the operator $\overline{q}^{x_{adv}}$. The even order operators (2nd, 4th, and 6th) are

2nd order: $\quad (\overline{q}^{x_{adv}})_{i-1/2} = \dfrac{1}{2}(q_i + q_{i-1})$

4th order: $\quad (\overline{q}^{x_{adv}})_{i-1/2} = \dfrac{7}{12}(q_i + q_{i-1}) - \dfrac{1}{12}(q_{i+1} + q_{i-2})$

6th order: $\quad (\overline{q}^{x_{adv}})_{i-1/2} = \dfrac{37}{60}(q_i + q_{i-1}) - \dfrac{2}{15}(q_{i+1} + q_{i-2}) + \dfrac{1}{60}(q_{i+2} + q_{i-3}),$

and the odd order operators (3rd and 5th) are

3rd order: $(\overline{q}^{x_{adv}})_{i-1/2} = (\overline{q}^{x_{adv}})_{i-1/2}^{4^{th}}$

$$+ \, \text{sign}(U)\frac{1}{12}\big[(q_{i+1} - q_{i-2}) - 3(q_i - q_{i-1})\big]$$

5th order: $(\overline{q}^{x_{adv}})_{i-1/2} = (\overline{q}^{x_{adv}})_{i-1/2}^{6^{th}}$

$$- \, \text{sign}(U)\frac{1}{60}\big[(q_{i+2} - q_{i-3}) - 5(q_{i+1} - q_{i-2}) + 10(q_i - q_{i-1})\big].$$

The even-order advection operators are spatially centered and thus contain no implicit diffusion outside of the diffusion inherent in the RK3 time integration. The odd-order schemes are upwind-biased, and the spatial discretization is inherently diffusive. The behavior of the upwind schemes is easily understood by expanding (3.46) using the 5th order operator, assuming a constant mass flux U and multiplying by the timestep Δt:

$$\Delta t \delta_x(U\overline{q}^{x_{adv}}) = \Delta t \delta(Uq)|^{6th} - \left|\frac{U\Delta t}{\Delta x}\right|\frac{1}{60}\left(-q_{i-3} + 6q_{i-2} - 15q_{i-1} + 20q_i - 15q_{i+1} + 6q_{i+2} - q_{i+3}\right)$$

$$= \Delta t \delta(Uq)|^{6th} - \frac{Cr}{60}\Delta x^6 \frac{\partial^6 q}{\partial x^6} + \text{higher order terms}$$

Similarly, we can expand (3.46) using the 3rd order operator:

$$\Delta t \delta_x(U\overline{q}^{x_{adv}}) = \Delta t \delta(Uq)|^{4th} + \frac{Cr}{12}\Delta x^4 \frac{\partial^4 q}{\partial x^4} + \text{higher order terms}$$

As is evident in their formulation, the odd-order schemes are comprised of the next higher (even) order centered scheme plus an upwind term that, for a constant transport mass flux, is a diffusion term of that next higher (even) order with a hyper-viscosity proportional to the Courant number (Cr). The diffusion term is the leading order error term in the flux divergence discretization. Further details concerning RK3 advection can be found in Wicker and Skamarock (2002)

Positive-Definite Limiter for RK3 Advection

Mixing ratios of moisture, chemical species or other tracer species should remain positive-definite, that is, negative masses should not be permitted. The Runge-Kutta transport integration defined by the timestepping algorithm (3.1) – (3.3), combined with the flux divergence operator (3.45), is conservative but it does not guarantee positive definiteness; any negative values will be offset by positive mass such that mass is conserved. In many physics options, negative mixing ratios will be set to zero, and this will result in an increase in mass of that species. A positive-definite flux renormalization, applied on the final Runge-Kutta transport step (3.1), can be used to remove this unphysical effect from the RK3 scalar transport scheme. This scheme is described in Skamarock and Weisman (2008) and Skamarock (2005), and we briefly outline the ARW implementation here.

The final RK3 time integration step for transport of a scalar can be expressed as

$$(\mu\phi)^{t+\Delta t} = (\mu\phi)^t - \Delta t\big\{m_x m_y[\delta_x(U\overline{q}^{x_{adv}}) + \delta_y(V\overline{q}^{y_{adv}})] + m_y\delta_\eta(\Omega\overline{q}^{\eta_{adv}})\big\} + \Delta t\mu S_\phi^t \qquad (3.47)$$

where the flux divergence is evaluated using the (**) time level predicted in RK3 step (3.2). The positive-definite flux renormalization replaces (3.2) with the following two steps. First, the scalar mixing ratio is updated using the tendency derived from the model physics and source/sink terms.

$$(\mu\phi)^{***} = (\mu\phi)^t + \Delta t \mu S_\phi^t \tag{3.48}$$

where we denote this new predictor as $(\mu\phi)^{***}$. Second, the full update is computed using a flux divergence composed of a first-order upwind flux plus a higher order correction:

$$\begin{aligned}(\mu\phi)^{t+\Delta t} = (\mu\phi)^{***} - \Delta t\{\ &m_x m_y(\delta_x\left[(U\overline{q}^{x_{adv}})^1 + R(U\overline{q}^{x_{adv}})'\right] \\ &+\delta_y\left[(V\overline{q}^{y_{adv}})^1 + R(V\overline{q}^{y_{adv}})'\right]) \\ &+m_y\delta_\eta\left[(\Omega\overline{q}^{\eta_{adv}})^1 + R(\Omega\overline{q}^{\eta_{adv}})'\right]\ \}.\end{aligned} \tag{3.49}$$

In (3.49), $()^1$ denotes a first-order upwind flux and $R()'$ denotes a renormalized higher-order correction flux. The higher-order correction flux is the difference between the full RK3 flux and the first-order upwind flux, that is,

$$(U\overline{q}^{x_{adv}}) = (U\overline{q}^{x_{adv}})^1 + (U\overline{q}^{x_{adv}})', \tag{3.50}$$

with similar definitions for $(V\overline{q}^{y_{adv}})'$ and $(\Omega\overline{q}^{\eta_{adv}})'$. The correction flux is then renormalized as follows. First, the upwind fluxes are used to perform a partial update of the scalar mass.

$$(\tilde{\mu\phi}) = (\mu\phi)^{***} - \Delta t\{m_x m_y[\delta_x(U\overline{q}^{x_{adv}})^1 + \delta_y(V\overline{q}^{y_{adv}})^1] + m_y\delta_\eta(\Omega\overline{q}^{\eta_{adv}})^1\}$$

This update is positive definite (and monotonic) by design because it is the first-order upwind scheme. Next, a prediction of the minimum possible values of the new-time-level species mass is computed at each point by using only the outward directed fluxes (fluxes that remove mass from the control volume),

$$(\mu\phi)_{min}^{t+\Delta t} = (\tilde{\mu\phi}) - \Delta t\{m_x m_y[\delta_x(U_+\overline{q}^{x_{adv}})' + \delta_y(V_+\overline{q}^{y_{adv}})'] + m_y\delta_\eta(\Omega_+\overline{q}^{\eta_{adv}})'\} \tag{3.51}$$

where U_+, V_+ and Ω_+ indicated the use of fluxes out of a control volume only, that is, only those that contribute to lowering the scalar mass. As is obvious from (3.51), the scalar mass $(\mu\phi)_{min}^{t+\Delta t} < 0$ if

$$(\tilde{\mu\phi}) < \Delta t\{m_x m_y[\delta_x(U_+\overline{q}^{x_{adv}})' + \delta_y(V_+\overline{q}^{y_{adv}})'] + m_y\delta_\eta(\Omega_+\overline{q}^{\eta_{adv}})'\}$$

For each volume where negative mass is indicated by (3.51), the fluxes are renormalized such that the outgoing fluxes and mass in the volume are equivalent.

$$R\left(U_+\overline{q}^{x_{adv}}\right)' = (U_+\overline{q}^{x_{adv}})'\ \frac{\tilde{\mu\phi}}{\Delta t\{m_x m_y[\delta_x(U_+\overline{q}^{x_{adv}})' + \delta_y(V_+\overline{q}^{y_{adv}})'] + m_y\delta_\eta(\Omega_+\overline{q}^{\eta_{adv}})'\}} \tag{3.52}$$

with a similar renormalization applied to the $(V\overline{q}^{y_{adv}})'$ and $(\Omega\overline{q}^{\eta_{adv}})'$. If no negative mass is indicated in (3.51), the correction flux is equal to the

$$R\left(U_+\overline{q}^{x_{adv}}\right)' = (U_+\overline{q}^{x_{adv}})',\ \ R\left(V_+\overline{q}^{y_{adv}}\right)' = (V_+\overline{q}^{y_{adv}})',\ \ R\left(\Omega_+\overline{q}^{\eta_{adv}}\right)' = (\Omega_+\overline{q}^{\eta_{adv}})'. \tag{3.53}$$

The renormalized fluxes (3.52) and (3.53), along with the first order fluxes, are then used in the update equation (3.49). Note that if no renormalization is needed, the scheme (3.49) reverts to the standard RK3 update because the definition of the correction (3.50).
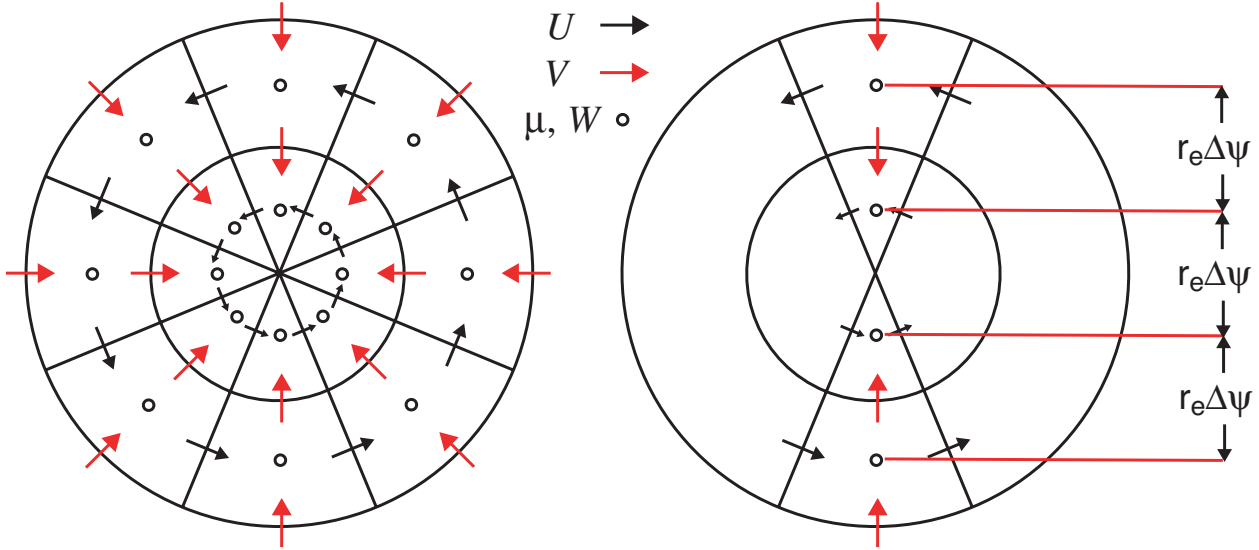
Figure 3.3: Latitude-longitude grid structure in the pole region. In the ARW formulation, $r_e\Delta\psi = \Delta y/m_y$.

3.2.4   Pole Conditions for the Global Latitude-Longitude Grid

The latitude-longitude grid has a singularity at the two poles where the latitude $\psi = \pm 90°$, as illustrated in Figure 3.3. By design, no variable is defined at the pole point. The area of the control volume face at the pole is zero, thus a flux at the pole point is not needed in the solution of any of the prognostic variables. For example, in the finite volume discretization of the mass conservation equation (3.23) for μ in a control volume closest to the pole, the meridional gradient (y gradient) of the mass flux $\delta_y V''$ will use zero for the pole contribution to this term.

The stencils for advection operators higher than 2nd order, described in Section 3.2.3, cross the poles for flux calculations at the control volume faces located $r_e\Delta\psi$ and $2r_e\Delta\psi$ from the pole point (Figure 3.3, the V flux is indicated in red). In the current implementation of the ARW, we reduce the order of the flux operator at these faces so that their stencils do not extend across the pole point. While this formally reduces the accuracy of the scheme, we have not been able to identify any significant degradation in the ARW solutions.

Coriolis and curvature terms are computed for the vertical momentum equation (3.37) and the horizontal momentum equation for U (3.35). For the W and U points that lie $r_e\Delta\psi/2$ from the pole, the stencils for these terms require a value of V at the pole point. We set the value of V at the pole equal to the value of V at $\Delta\psi$ to evaluate these operators. This approximation is also used for the meridional advection of V, combined with a lowering of the flux-operator order to avoid differencing across the pole (as with the flux divergence terms for the other prognostic variables).

3.3   Stability Constraints

There are two time steps that a user must specify when running the ARW: the model time step (the time step used by the RK3 scheme, see Section 3.1.1) and the acoustic time step (used

in the acoustic sub-steps of the time-split integration procedure, see Section 3.1.2). Both are limited by Courant numbers. In the following sections we describe how to choose time steps for applications.

3.3.1   RK3 Time Step Constraint

The RK3 time step is limited by the advective Courant number $u\Delta t/\Delta x$ and the user's choice of advection schemes— users can choose 2nd through 6th order discretizations for the advection terms. The time-step limitations for 1D advection in the RK3 scheme using these advection schemes is given in Wicker and Skamarock (2002), and is reproduced here.

Time Scheme	Spatial order			
	3rd	4th	5th	6th
Leapfrog	*Unstable*	0.72	*Unstable*	0.62
RK2	0.88	*Unstable*	0.30	*Unstable*
RK3	1.61	1.26	1.42	1.08

Table 3.1: Maximum stable Courant numbers for one-dimensional linear advection. From Wicker and Skamarock (2002).

As is indicated in the table, the maximum stable Courant numbers for advection in the RK3 scheme are almost a factor of two greater than those for the leapfrog time-integration scheme. For advection in three spatial dimensions, the maximum stable Courant number is $1/\sqrt{3}$ times the Courant numbers given in Table 3.1. For stability, the time step used in the ARW should produce a maximum Courant number less than that given by theory. Thus, for 3D applications, the time step should satisfy the following equation:

$$\Delta t_{max} < \frac{Cr_{theory}}{\sqrt{3}} \cdot \frac{\Delta x}{u_{max}}, \tag{3.54}$$

where Cr_{theory} is the Courant number taken from the RK3 entry in Table 3.1 and u_{max} is the maximum velocity expected in the simulation. For example in real-data applications, where jet stream winds may reach as high as 100 ms^{-1}, the maximum time step would be approximately 80 s on a $\Delta x = 10$ km grid using 5th order advection. For convection-permitting resolutions (typically $\Delta x \leq 5$ km), the vertical velocities in convective updrafts produce the stability-limiting Courant numbers. Given additional constraint from the time splitting, and to provide a safety buffer, we usually choose a time step that is approximately 25% less than that given by (3.54). This time step is typically a factor of two greater than that used in leapfrog-based models. For those users familiar with the MM5 model, the rule of thumb for choosing a time step is that the time step, in seconds, should be approximately 3 times the horizontal grid distance, in kilometers. For the ARW, the time step (in seconds) should be approximately 6 times the grid distance (in kilometers).

3.3.2   Acoustic Time Step Constraint

The forward-backward time integration scheme used in the ARW's 2D explicit acoustic step integration allows a maximum Courant number $Cr_{max} = c_s\Delta\tau/\Delta x < 1/\sqrt{2}$, where c_s is the

speed of sound. We typically use a more conservative estimate for this by replacing the limiting value $1/\sqrt{2}$ with $1/2$. Thus, the acoustic time step used in the model is

$$\Delta\tau < 2 \cdot \frac{\Delta x}{c_s}. \tag{3.55}$$

For example, on a $\Delta x = 10$ km grid, using a sound speed $c_s = 300$ ms^{-1}, the acoustic time step given in (3.55) is approximately 17 s. In the ARW, the ratio of the RK3 time step to the acoustic time step must be an even integer. For our example using a $\Delta x = 10$ km grid in a real-data simulation, we would specify the RK3 time step $\Delta t = 60s$ (i.e., 25% less than the 80 s step given by (3.54), and an acoustic time step $\Delta\tau = 15$ s (i.e., 1/4 of the RK3 step, rounding down the $\Delta\tau = 17$ s step given by (3.55)). Note that it is the ratio of the RK3 time step to the acoustic time step that is the required input in the ARW.

3.3.3 Adaptive Time Step

The ARW model is typically integrated with a fixed timestep, that is chosen to produce a stable integration. During any time in the integration, the maximum stable timestep is likely to be larger than the fixed timestep. In ARWV3, an adaptive timestepping capability has been introduced that chooses the RK3 timestep based on the temporally-evolving wind fields. The adaptively-chosen timestep is usually larger than the typical fixed timestep, hence the dynamics integrates faster and physics are called less often, and the time-to-completion of the simulation can be substantially reduced.

In the adaptive timestep scheme, a target maximum Courant number Cr_{target} is chosen, where typically $1.1 \leq Cr_{target} \leq 1.2$. The maximum Courant number in the domain at a given time (Cr_{domain}), computed for all the velocity components (u, v, w), is then used to compute a new timestep. When the maximum Courant number in the domain is less than the target maximum Courant number ($Cr_{domain} < Cr_{target}$), then the timestep can be increased and the new timestep is computed using

$$\Delta t_{current} = min\left(1 + f_i, \frac{Cr_{target}}{Cr_{domain}}\right) \cdot \Delta t_{previous}, \tag{3.56}$$

where a typical value for the regulated increase is $f_i \leq 5\%$. When the computed maximum domain-wide Courant number exceeds the targeted maximum allowable Courant number ($Cr_{domain} > Cr_{target}$), then the time step is decreased to insure model stability:

$$\Delta t_{current} = max\left(1 - f_d, \frac{Cr_{target} - 0.5(Cr_{domain} - Cr_{target})}{Cr_{domain}}\right) \cdot \Delta t_{previous}, \tag{3.57}$$

where typically the factor to decrease the time step $f_d = 25\%$. Both a lower bound and an upper bound on the time step are enforced based on the initial settings of the time step suggested in section 3.3.1:

$$\Delta t_{init} = 6 \cdot \Delta x, \tag{3.58}$$

$$\Delta t_{min} = 0.5 \cdot \Delta t_{init}, \tag{3.59}$$

$$\Delta t_{max} = 3.0 \cdot \Delta t_{init}, \tag{3.60}$$

$$\Delta t = min(max(\Delta t, \Delta t_{min}), \Delta t_{max}), \tag{3.61}$$

to guard the time step from becoming too small or too large. The computation of the number of acoustic time steps n_a, described in section 3.3.2, is handled during the first of each of the RK3 model integration steps:

$$n_a = max\left(2 \cdot \lfloor 300 \cdot \frac{\Delta t}{\Delta x} + 1\rfloor, 4\right). \tag{3.62}$$

For a simulation using nests, the fine-grid domain must maintain an integer number of time steps within a single model integration step from the parent. At each of the starting model integration steps for the child grid, those integration steps when the time on the fine-grid domain equals the time on the parent's domain, the adaptive time step algorithm is conducted for the fine grid. Note that the ratio of the nominal grid distance between the parent and the child does not necesarily imply that same ratio between the model integration time steps.

3.3.4 Map Projection Considerations

For ARW configurations using the Lambert conformal, polar stereographic, or Mercator projections, the timestep constraints is determined by the smallest physical horizontal grid spacing, i.e. $min(\Delta x/m_x, \Delta y/m_y)$. For global applications, the grid distance used to determine the timestep should be $\Delta x/m_x$ evaluated at the computational latitude at which the polar filters are activated. Polar filtering is discussed in section 4.1.

Chapter 4

Turbulent Mixing and Model Filters

A number of formulations for turbulent mixing and filtering are available in the ARW solver. Some of these filters are used for numerical reasons. For example, divergence damping is used to filter acoustic modes from the solution and polar filtering is used to reduce the timestep restriction arising from the converging gridlines of the latitude-longitude grid. Other filters are meant to represent sub-grid turbulence processes that cannot be resolved on the chosen grid. These filters remove energy from the solution and are formulated in part on turbulence theory and observations, or represent energy sink terms in some approximation to the Euler equation. In this section, we begin by outlining the formulation and discretization of turbulent mixing processes in the ARW solver commonly associated with sub-gridscale turbulence as parameterized in cloud-scale models— the second-order horizontal and vertical mixing. In large-scale models and most NWP models, vertical mixing is parameterized within the planetary boundary layer (PBL) physics. Vertical mixing parameterized within the PBL physics is described later in Chapter 8. Here we note that, when a PBL parameterization is used, all other vertical mixing is disabled. Following the outline of turbulent mixing parameterizations in this chapter, other numerical filters available in the ARW solver are described.

4.1   Latitude-Longitude Global Grid and Polar Filtering

Polar filtering is used to reduce the timestep restriction associated with the gridlines that converge as they approach the poles of the latitude-longitude grid; the converging gridlines reduce the longitudinal gridlength, and thus the stable timestep for transport, discussed in Section 3.3.1, and for acoustic waves, discussed in Section 3.3.2, will be reduced.

Polar filtering a given variable is accomplished by first applying a 1D Fourier transform to the variable on a constant computational-grid latitude circle (the forward transform), where the field is periodic. The Fourier coefficients with wavenumbers above a prescribed threshold are truncated, after which a transformation back to physical space is applied (the backward transform), completing the filter step.

A filter application can be written as

$$\hat{\phi}(k)_{filtered} = a(k)\, \hat{\phi}(k), \quad \text{for all } k,$$

where $\hat{\phi}(k)$ and $\hat{\phi}(k)_{filtered}$ are the Fourier coefficients for the generic variable ϕ before and after filtering, and $a(k)$ are the filter coefficients defined as a function of the dimensionless wavenumber

29

k. The ARW polar filter coefficients $a(k)$ for the Fourier amplitudes are

$$a(k) = \min\left[1., \max\left(0., \left(\frac{\cos\psi}{\cos\psi_o}\right)^2 \frac{1}{\sin^2(\pi k/n)}\right)\right]$$

where ψ is the latitude on the computational grid, ψ_o is the latitude above which the polar filter is applied (the filter is applied for $|\psi| > \psi_o$), and n is the number of grid points in the latitude circle. For even n, the grid admits wavenumber $k = 0$ and dimensionless wavenumbers $\pm k$ for $k = 1 \to n/2 - 1$, and the 2Δ wave $k = n/2$. For odd n, the grid admits wavenumber $k = 0$, and dimensionless wavenumbers $\pm k$ for $k = 1 \to (n-1)/2$.

Polar filter applications within the split-explicit RK3 time integration scheme are given in Figure 3.1. Within the acoustic steps, the filter is applied to $U''^{\tau+\Delta\tau}$ and $V''^{\tau+\Delta\tau}$ immediately after the horizontal momentum is advanced, to $\mu_d^{\tau+\Delta\tau}$ and $\Theta''^{\tau+\Delta\tau}$ immediately after the column mass and the potential temperature are advanced, and to $W''^{\tau+\Delta\tau}$ and $\phi''^{\tau+\Delta\tau}$ after the vertically implicit part of the acoustic step is complete. The polar filter is also applied to the scalars after they are advanced every RK3 sub-step (3.1)-(3.3) and after the microphysics step.

The prognostic variables are coupled with the column mass μ when filtered, and in this way mass is conserved. An exception to this is the geopotential ϕ which is filtered without being coupled. The Fourier filtering is conservative, but it is not monotonic or positive definite. As noted in the ARW stability discussion in Section 3.3.4, timestep stability should be based on the longitudinal gridlength where the polar filters are activated, $(\Delta x/m_x)|_{\psi_o}$. The positive definite transport option, presented in Section 3.2.3, will not necessarily produce positive-definite results because of the converging gridlines and should not be used.

4.2   Explicit Spatial Diffusion

The ARW solver has three formulations for spatial dissipation— diffusion along coordinate surfaces, diffusion in physical (x, y, z) space, and a sixth-order diffusion applied on horizontal coordinate surfaces. In the following sections we present the diffusion operators for the the first two formulations, followed by the four separate formulations that can be used to compute the eddy viscosities and a description of the prognostic turbulent kinetic energy (TKE) equation used in one set of these formulations. The sixth order spatial filter is described at the end of this section. In these formulations, the horizontal (K_h) and vertical (K_v) eddy viscosities are defined at scalar points on the staggered model grid.

4.2.1   Horizontal and Vertical Diffusion on Coordinate Surfaces

For any model variable, horizontal and vertical second order spatial filtering on model coordinate surfaces is considered part of the RHS terms in the continuous equations (2.38) – (2.44) and can be expressed as follows for a model variable a:

$$\partial_t(\mu_d a) = \ldots + \mu_d\left[m_x\partial_x(m_x K_h\partial_x a) + m_y\partial_y(m_y K_h\partial_y a)\right] + g^2(\mu_d\alpha)^{-1}\partial_\eta(K_v\alpha^{-1}\partial_\eta a). \quad (4.1)$$

For the horizontal and vertical momentum equations, (4.1) is spatially discretized as

$$\partial_t U = ... \ + \overline{\mu_d}^x \overline{m_x}^x \big[\delta_x(m_x K_h \delta_x u) + \delta_y(\overline{m_y}^{xy} \overline{K_h}^{xy} \delta_y u)\big] + m_y^{-1} g^2 (\overline{\mu_d}^x \overline{\alpha}^x)^{-1} \delta_\eta(\overline{K_v}^{x\eta}(\overline{\alpha}^{x\eta})^{-1}\delta_\eta u)$$

$$\partial_t V = ... \ + \overline{\mu_d}^y \overline{m_y}^y \big[\delta_x(\overline{m_x}^{xy} \overline{K_h}^{xy} \delta_x v) + \delta_y(m_y K_h \delta_y v)\big] + m_x^{-1} g^2 (\overline{\mu_d}^y \overline{\alpha}^y)^{-1} \delta_\eta(\overline{K_v}^{y\eta}(\overline{\alpha}^{y\eta})^{-1}\delta_\eta v)$$

$$\partial_t W = ... \ + \mu_d m_x \big[\delta_x(\overline{m_x}^x \overline{K_h}^{x\eta} \delta_x w) + \delta_y(\overline{m_y}^y \overline{K_h}^{y\eta} \delta_y w)\big] + m_y^{-1} g^2 (\mu_d \overline{\alpha}^\eta)^{-1} \delta_\eta(K_v \alpha^{-1} \delta_\eta w).$$

The spatial discretization for a scalar q, defined at the mass points, is

$$\partial_t(\mu_d q) = ... \ + \mu_d m_x m_y \big[\delta_x(\overline{m_x}^x P_r^{-1} \overline{K_h}^x \delta_x q) + \delta_y(\overline{m_y}^y P_r^{-1} \overline{K_h}^y \delta_y q)\big] + g^2 (\mu_d \alpha)^{-1} \delta_\eta(\overline{K_v}^\eta (\overline{\alpha}^\eta)^{-1} \delta_\eta q).$$

In the current ARW formulation for mixing on coordinate surfaces, the horizontal eddy viscosity K_h is allowed to vary in space, whereas the vertical eddy viscosity does not vary in space; hence there is no need for any spatial averaging of K_v. Additionally, note that the horizontal eddy viscosity K_h is multiplied by the inverse turbulent Prandtl number P_r^{-1} for horizontal scalar mixing.

4.2.2 Horizontal and Vertical Diffusion in Physical Space

Coordinate Metrics

We use the geometric height coordinate in this physical space formulation. The coordinate metrics are computed using the prognostic geopotential in the ARW solver. At the beginning of each Runge-Kutta time step, the coordinate metrics are evaluated as part of the overall algorithm. The definitions of the metrics are

$$z_x = g^{-1}\delta_x \phi \ \text{ and } \ z_y = g^{-1}\delta_y \phi.$$

These metric terms are defined on w levels, and (z_x, z_y) are horizontally coincident with (u,v) points. Additionally, the vertical diffusion terms are evaluated directly in terms of the geometric height, avoiding the need for metric terms in the vertical.

Continuous Equations

The continuous equations for evaluating diffusion in physical space, using the velocity stress tensor, are as follows for horizontal and vertical momentum:

$$\partial_t U = ... \ - m_x \big[\partial_x \tau_{11} + \partial_y \tau_{12} - \partial_z(z_x \tau_{11} + z_y \tau_{12})\big] - \partial_z \tau_{13} \tag{4.2}$$

$$\partial_t V = ... \ - m_y \big[\partial_x \tau_{12} + \partial_y \tau_{22} - \partial_z(z_x \tau_{12} + z_y \tau_{22})\big] - \partial_z \tau_{23} \tag{4.3}$$

$$\partial_t W = ... \ - m_y \big[\partial_x \tau_{13} + \partial_y \tau_{23} - \partial_z(z_x \tau_{13} + z_y \tau_{23})\big] - \partial_z \tau_{33}. \tag{4.4}$$

The stress tensor τ can be written as follows:

$$\tau_{11} = -\mu_d K_h D_{11}$$
$$\tau_{22} = -\mu_d K_h D_{22}$$
$$\tau_{33} = -\mu_d K_v D_{33}$$
$$\tau_{12} = -\mu_d K_h D_{12}$$
$$\tau_{13} = -\mu_d K_v D_{13}$$
$$\tau_{23} = -\mu_d K_v D_{23}.$$

Symmetry sets the remaining tensor values; $\tau_{21} = \tau_{12}$, $\tau_{31} = \tau_{13}$, and $\tau_{32} = \tau_{23}$. The stress tensor τ is calculated from the deformation tensor D. The continuous deformation tensor is defined as

$$D_{11} = 2\,m_x m_y\left[\partial_x(m_y^{-1}u) - z_x\partial_z(m_y^{-1}u)\right]$$
$$D_{22} = 2\,m_x m_y\left[\partial_y(m_x^{-1}v) - z_y\partial_z(m_x^{-1}v)\right]$$
$$D_{33} = 2\,\partial_z w$$
$$D_{12} = m_x m_y\left[\partial_y(m_y^{-1}u) - z_y\partial_z(m_y^{-1}u) + \partial_x(m_x^{-1}v) - z_x\partial_z(m_x^{-1}v)\right]$$
$$D_{13} = m_x m_y\left[\partial_x(m_y^{-1}w) - z_x\partial_z(m_y^{-1}w)\right] + \partial_z(u)$$
$$D_{23} = m_x m_y\left[\partial_y(m_y^{-1}w) - z_y\partial_z(m_y^{-1}w)\right] + \partial_z(v).$$

The deformation tensor is symmetric, hence $D_{21} = D_{12}$, $D_{31} = D_{13}$, and $D_{32} = D_{23}$.

The diffusion formulation for scalars is

$$\partial_t(\mu_d q) = \ldots + \left[m_x(\partial_x - \partial_z z_x)(\mu_d m_x K_h(\partial_x - z_x \partial_z)) + \right.$$
$$\left. m_y(\partial_y - \partial_z z_y)(\mu_d m_y K_h(\partial_y - z_y \partial_z)) + \partial_z \mu_d K_v \partial_z\right]q. \tag{4.5}$$

Spatial Discretization

Using the definition of the stress tensor, the spatial discretization of the ARW physical-space diffusion operators for the horizontal and vertical momentum equations (4.2) - (4.4) are

$$\partial_t U = \ldots - \overline{m_x}^x\left[\delta_x\tau_{11} + \delta_y\tau_{12} - \delta_z(z_x\overline{\tau_{11}}^{x\eta} + \overline{z_y}^{xy}\overline{\tau_{12}}^{y\eta})\right] - \delta_z\tau_{13}$$
$$\partial_t V = \ldots - \overline{m_y}^y\left[\delta_y\tau_{22} + \delta_x\tau_{12} - \delta_z(z_y\overline{\tau_{22}}^{y\eta} + \overline{z_x}^{xy}\overline{\tau_{12}}^{x\eta})\right] - \delta_z\tau_{23}$$
$$\partial_t W = \ldots - m_x\left[\delta_x\tau_{13} + \delta_y\tau_{23} - \delta_z(\overline{z_x}^{x\eta}\overline{\tau_{13}}^{x\eta} + \overline{z_y}^{y\eta}\overline{\tau_{23}}^{y\eta})\right] - \delta_z\tau_{33}.$$

The discrete forms of the stress tensor and deformation tensor are

$$\tau_{11} = -\mu_d K_h D_{11}$$
$$\tau_{22} = -\mu_d K_h D_{22}$$
$$\tau_{33} = -\mu_d K_v D_{33}$$
$$\tau_{12} = -\overline{\mu_d}^{xy}\overline{K_h}^{xy} D_{12}$$
$$\tau_{13} = -\overline{\mu_d}^{x}\overline{K_v}^{x\eta} D_{13}$$
$$\tau_{23} = -\overline{\mu_d}^{y}\overline{K_v}^{y\eta} D_{23},$$

and

$$D_{11} = 2\,m_x m_y\left[\delta_x(\overline{m_y^{-1}}^x u) - \overline{z_x}^{x\eta}\delta_z(\overline{m_y^{-1}}^x u)\right]$$
$$D_{22} = 2\,m_x m_y\left[\delta_y(\overline{m_x^{-1}}^y v) - \overline{z_y}^{x\eta}\delta_z(\overline{m_x^{-1}}^y v)\right]$$
$$D_{33} = 2\,\delta_z w$$
$$D_{12} = (\overline{m_x m_y}^{xy})\left[\delta_y(\overline{m_y^{-1}}^x u) - \overline{z_y}^{x\eta}\delta_z\overline{(\overline{m_y^{-1}}^x u)}^{y\eta} + \delta_x(\overline{m_x^{-1}}^y v) - \overline{z_x}^{y\eta}\delta_z\overline{(\overline{m_x^{-1}}^y v)}^{x\eta}\right]$$
$$D_{13} = m_x m_y\left[\delta_x(m_y^{-1}w) - z_x\delta_z\overline{(m^{-1}w)}^{x\eta}\right] + \delta_z u$$
$$D_{23} = m_x m_y\left[\delta_y(m_y^{-1}w) - z_y\delta_z\overline{(m_y^{-1}w)}^{y\eta}\right] + \delta_z v.$$

The spatial discretization for the scalar diffusion (4.5) is

$$\partial_t(\mu_d q) = \ldots + m_x\left[\delta_x\left(\overline{\mu_d}^x H_1(q)\right) - \mu_d\delta_z\left(\overline{z_x}^x\overline{H_1(q)}^{x\eta}\right)\right]$$
$$+ m_y\left[\delta_y\left(\overline{\mu_d}^y H_2(q)\right) - \mu_d\delta_z\left(\overline{z_y}^y\overline{H_2(q)}^{y\eta}\right)\right]$$
$$+ \mu_d\delta_z\left(\overline{K_v}^\eta\delta_z q\right),$$

where

$$H_1(q) = \overline{m_x}^x\overline{K_h}^x\left(\delta_x q - z_x\delta_z(\overline{q}^{x\eta})\right),$$
$$H_2(q) = \overline{m_y}^y\overline{K_h}^y\left(\delta_y q - z_y\delta_z(\overline{q}^{y\eta})\right).$$

4.2.3 Computation of the Eddy Viscosities

There are four options for determining the eddy viscosities K_h and K_v in the ARW solver.

External specification of K_h and K_v

Constant values for K_h and K_v can be input in the ARW namelist.

K_h determined from the horizontal deformation

The horizontal eddy viscosity K_h can be determined from the horizontal deformation using a Smagorinsky first-order closure approach. In this formulation, the eddy viscosity is defined and discretized as

$$K_h = C_s^2\, l^2\left[0.25(D_{11} - D_{22})^2 + \overline{D_{12}^2}^{xy}\right]^{\frac{1}{2}}.$$

The deformation tensor components have been defined in the previous section. The length scale $l = (\Delta x\Delta y)^{1/2}$ and C_s is a constant with a typical value $C_s = 0.25$. For scalar mixing, the eddy viscosity is divided by the turbulent Prandtl number P_r that typically has a value of $1/3$ (Deardorff, 1972). This option is most often used with a planetary boundary layer scheme that independently handles the vertical mixing.

3D Smagorinsky Closure

The horizontal and vertical eddy viscosities can be determined using a 3D Smagorinsky turbulence closure. This closure specifies the eddy viscosities as

$$K_{h,v} = C_s^2\, l_{h,v}^2 \max\left[0., \left(D^2 - P_r^{-1}N^2\right)^{1/2}\right], \tag{4.6}$$

where

$$D^2 = \frac{1}{2}\left[D_{11}^2 + D_{22}^2 + D_{33}^2\right] + \left(\overline{D_{12}}^{xy}\right)^2 + \left(\overline{D_{13}}^{x\eta}\right)^2 + \left(\overline{D_{23}}^{y\eta}\right)^2,$$

and N is the Brunt-Väisälä frequency; the computation of N, including moisture effects, is outlined in Section 4.2.4.

Two options are available for calculating the mixing length $l_{h,v}$ in (4.6). An isotropic length scale (appropriate for $\Delta x, \Delta y \simeq \Delta z$) can be chosen where $l_{h,v} = (\Delta x \Delta y \Delta z)^{1/3}$ and thus $K_h = K_v = K$. The anisotropic option (appropriate for $\Delta x, \Delta y \gg \Delta z$) sets the horizontal mixing length $l_h = \sqrt{\Delta x \Delta y}$ in the calculation of the horizontal eddy viscosity K_h using (4.6), and $l_v = \Delta z$ for the calculation of the vertical eddy viscosity K_v using (4.6).

Additionally, the eddy viscosities for scalar mixing are divided by the turbulent Prandtl number $P_r = 1/3$.

Prognostic TKE Closure

For the predicted turbulent kinetic energy option (TKE; see section 4.2.4), the eddy viscosities are computed using

$$K_{h,v} = C_k l_{h,v} \sqrt{e},$$

where e is the turbulent kinetic energy (a prognostic variable in this scheme), C_k is a constant (typically $0.15 < C_k < 0.25$), and l is a length scale.

If the isotropic mixing option is chosen,

$$l_{h,v} = \min\left[(\Delta x \Delta y \Delta z)^{1/3}, 0.76\sqrt{e}/N\right] \qquad \text{for } N^2 > 0,$$
$$l_{h,v} = (\Delta x \Delta y \Delta z)^{1/3} \qquad \text{for } N^2 \leq 0$$

(see section 4.2.4 for the calculation of N^2). Both the horizontal and vertical eddy viscosities are multiplied by an inverse turbulent Prandtl number $P_r^{-1} = 1 + 2l/(\Delta x \Delta y \Delta z)^{1/3}$ for scalar mixing. In this case ($l_{cr} > \Delta x$) the horizontal and vertical eddy viscosities are equivalent.

If the anisotropic mixing option is chosen, then $l_h = \sqrt{\Delta x \Delta y}$ for the calculation of K_h. For calculating K_v,

$$l_v = \min\left[\Delta z, 0.76\sqrt{e}/N\right] \qquad \text{for } N^2 > 0,$$
$$l_v = \Delta z \qquad \text{for } N^2 \leq 0.$$

The eddy viscosity used for mixing scalars is divided by a turbulent Prandtl number P_r. The Prandtl number is $1/3$ for the horizontal eddy viscosity K_h, and $P_r^{-1} = 1 + 2l/\Delta z$ for the vertical eddy viscosity K_v.

4.2.4 TKE equation for the 1.5 Order Turbulence Closure

The prognostic equation governing the evolution of the turbulent kinetic energy e is

$$\partial_t(\mu_d e) + (\nabla \cdot \mathbf{V} e)_\eta = \mu_d(\text{ shear production } + \text{ buoyancy } + \text{ dissipation }). \qquad (4.7)$$

The time integration and the transport terms in (4.7) are integrated in the same manner as for other scalars (as described in Chapter 3). The right-hand side source and sink terms for e are given as follows.

Shear Production

The shear production term in (4.7) can be written as

$$\text{shear production} = K_h D_{11}^2 + K_h D_{22}^2 + K_v D_{33}^2 + K_h \overline{D_{12}^2}^{xy} + K_v \overline{D_{13}^2}^{x\eta} + K_v \overline{D_{23}^2}^{y\eta}.$$

Buoyancy

The buoyancy term in the TKE equation (4.7) is written as

$$\text{buoyancy} = -K_v N^2,$$

where the Brunt-Väisälä frequency N is computed using either the formula for a moist saturated or unsaturated environment:

$$N^2 = g\big[A\partial_z\theta_e - \partial_z q_w\big] \qquad \text{if } q_v \geq q_{vs} \text{ or } q_c \geq 0.01 \text{ g/Kg;}$$

$$N^2 = g\left[\frac{1}{\theta}\partial_z\theta + 1.61\partial_z q_v - \partial_z q_w\right] \qquad \text{if } q_v < q_{vs} \text{ or } q_c < 0.01 \text{ g/Kg.}$$

The coefficient A is defined as

$$A = \theta^{-1}\frac{1 + \frac{1.61\epsilon L q_v}{R_d T}}{1 + \frac{\epsilon L^2 q_v}{C_p R_v T^2}},$$

where q_w represents the total water (vapor + all liquid species + all ice species), L is the latent heat of condensation and ϵ is the ratio of the molecular weight of water vapor to the molecular weight of dry air. θ_e is the equivalent potential temperature and is defined as

$$\theta_e = \theta\left(1 + \frac{L q_{vs}}{C_p T}\right),$$

where q_{vs} is the saturation vapor mixing ratio.

Dissipation

The dissipation term in (4.7) is

$$\text{dissipation} = -\frac{C e^{3/2}}{l},$$

where

$$C = 1.9\, C_k + \frac{(0.93 - 1.9\, C_k)\, l}{\Delta s},$$

$\Delta s = (\Delta x \Delta y \Delta z)^{1/3}$, and

$$l = min\big[(\Delta x \Delta y \Delta z)^{1/3}, 0.76\sqrt{e}/N\big].$$

4.2.5   Sixth-Order Spatial Filter on Coordinate Surfaces

A sixth order spatial filter is available that is applied on horizontal coordinate surfaces. The diffusion scheme is that proposed by Xue (2000). Its application in the ARW is described by Knievel et al. (2007). The filter can be expressed as

$$\partial_t(\mu_d a) = ...\frac{\beta\, 2^{-6}}{2\Delta t}\big[\Delta x^6 \delta_x(\overline{\mu_d}^x F_x) + \Delta y^6 \delta_y(\overline{\mu_d}^y F_y)\big] \qquad (4.8)$$

The diffusive fluxes $F_x = \delta_x^5(a)$ and $F_y = \delta_y^5(a)$. β is a user-specified filtering coefficient representing the damping applied to 2Δ waves for each filter application.

The user can choose to enforce monotonicity in the filtering. In the monotonic option, the diffusive fluxes are set to zero if up-gradient diffusion is indicated – $F_x = 0$ if $F_x \, \delta_x(a) < 0$ and $F_y = 0$ if $F_y \, \delta_y(a) < 0$. Note that the filter is applied in computational space; map factors are not taken into account and the filter parameter β is dimensionless. Thus, the filter scales with the timestep and gridsize and it does not conserve scalar mass. This explicit diffusion acts on all three components of wind, potential temperature, all moisture variables and passive scalars, and subgrid turbulence kinetic energy. Further details can be found in Knievel et al. (2007).

4.3 Filters for the Time-split RK3 scheme

Three filters are used in the ARW time-split RK3 scheme apart from those in the model physics: three-dimensional divergence damping (an acoustic model filter); an external-mode filter that damps vertically-integrated horizontal divergence; and off-centering of the vertically implicit integration of the vertical momentum equation and geopotential equation. Each of these is described in the following sections.

4.3.1 Three-Dimensional Divergence Damping

The damping of the full mass divergence is a filter for acoustic modes in the ARW solver. This 3D mass divergence damping is described in Skamarock and Klemp (1992). The filtering is accomplished by forward weighting the pressure update in the acoustic step loop described in Section 3.1.3, step (6). The linearized equation of state (3.5) is used to diagnose the pressure at the new time τ after the U'', V'', μ''_d, and Θ'' have been advanced. Divergence damping consists of using a modified pressure in the computation of the pressure gradient terms in the horizontal momentum equations in the acoustic steps (Equations (3.7) and (3.8)). Denoting the updated value as p^τ, the modified pressure $p^{*\tau}$ used in (3.7) and (3.8) can be written as

$$p^{*\tau} = p^\tau + \gamma_d\big(p^\tau - p^{\tau-\Delta\tau}\big), \tag{4.9}$$

where γ_d is the damping coefficient. This modification is equivalent to inserting a horizontal diffusion term into the equation for the 3D mass divergence, hence the name *divergence damping*. A divergence damping coefficient $\gamma_d = 0.1$ is typically used in the ARW applications, independent of time step or grid size.

4.3.2 External Mode Filter

The external modes in the solution are damped by filtering the vertically-integrated horizontal divergence. This damping is accomplished by adding a term to the horizontal momentum equations. The additional term added to (3.7) and (3.8) are

$$\delta_\tau U'' = ... \ - \gamma_e \delta_x(\delta_{\tau-\Delta\tau} \mu''_d) \tag{4.10}$$

and

$$\delta_\tau V'' = ... \ - \gamma_e \delta_y(\delta_{\tau-\Delta\tau} \mu''_d). \tag{4.11}$$

36

The quantity $\delta_{\tau-\Delta\tau}\mu$ is the vertically-integrated mass divergence (i.e., (3.20)) from the previous acoustic step (that is computed using the time τ values of U and V), and γ_e is the external mode damping coefficient. An external mode damping coefficient $\gamma_e = \beta\frac{\Delta x^2}{\Delta t}$, $\beta = 0.01$, is typically used in the ARW applications, independent of time step or grid size.

4.3.3 Semi-Implicit Acoustic Step Off-centering

Forward-in-time weighting of the vertically-implicit acoustic-time-step terms damps instabilities associated vertically-propagating sound waves. The forward weighting also damps instabilities associated with sloping model levels and horizontally propagating sound waves (see Durran and Klemp, 1983; Dudhia, 1995). The off-centering is accomplished by using a positive (non-zero) coefficient β (3.19) in the acoustic time-step vertical momentum equation (3.11) and geopotential equation (3.12). An off-centering coefficient $\beta = 0.1$ is typically used in the ARW applications, independent of time step or grid size.

4.4 Formulations for Gravity Wave Absorbing Layers

There are three formulations for absorbing vertically-propagating gravity waves so as to prevent unphysical wave reflection off the domain upper boundary from contaminating ARW solutions.

4.4.1 Absorbing Layer Using Spatial Filtering

This formulation of the absorbing layer increases the second-order horizontal and vertical eddy viscosities in the absorbing layer using the following formulation:

$$K_{dh} = \frac{\Delta x^2}{\Delta t}\gamma_g \cos\left(\frac{\pi}{2}\frac{z_{top}-z}{z_d}\right),$$

and

$$K_{dv} = \frac{\Delta z^2}{\Delta t}\gamma_g \cos\left(\frac{\pi}{2}\frac{z_{top}-z}{z_d}\right).$$

Here γ_g is a user-specified damping coefficient, z_{top} is the height of the model top for a particular grid column, z_d is the depth of the damping layer (from the model top), and K_{dh} and K_{dv} are the horizontal and vertical eddy viscosities for the wave absorbing layer. If other spatial filters are being used, then the eddy viscosities that are used for the second-order horizontal and vertical eddy viscosities are the maximum of (K_h, K_{dh}) and (K_v, K_{dv}). The effect of this filter on gravity waves is discussed in Klemp and Lilly (1978), where guidance on the choice of the damping coefficient γ_g can also be found.

4.4.2 Implicit Rayleigh Damping for the Vertical Velocity

Implicitly damping the vertical velocity within the implicit solution algorithm for the vertically propagating acoustic modes has been found to be a very effective and robust absorbing layer formulation by Klemp et al. (2008). We recommend its use in both large-scale and small-scale applications, and in idealized and real-data applications. It has proven more effective than the

spatial-filter-based absorbing layer described in Section 4.4.1, and it is more effective and more generally applicable than traditional Rayleigh damping because of its implicit nature and the fact that it does not need a reference state. This formulation has been introduced in WRFV3. It can only be used with the nonhydrostatic dynamics option.

In the vertically-implicit solution procedure for $W''^{\tau+\Delta\tau}$ and $\phi''^{\tau+\Delta\tau}$ in the acoustic step (step 5 in Figure 3.1), equation (3.12) is used to eliminate $\phi''^{\tau+\Delta\tau}$ from (3.11) after which the tridiagonal equation in the vertical direction for $W''^{\tau+\Delta\tau}$ is solved. Afterwards $\phi''^{\tau+\Delta\tau}$ is recovered using (3.12). In the solution procedure that includes the implicit Rayleigh damping for W, after the tridiagonal equation for W'' is solved and before the geopotential ϕ is updated, the implicit Rayleigh damping is included by calculating $W''^{\tau+\Delta\tau}$ using

$$W''^{\tau+\Delta\tau} = \tilde{W}''^{\tau+\Delta\tau} - \tau(z)\Delta\tau W''^{\tau+\Delta\tau} \qquad (4.12)$$

where $\tilde{W}''^{\tau+\Delta\tau}$ is the solution to (3.11). The geopotential is then updated as usual using (3.12) with the updated damped vertical velocity from (4.12). The perturbation pressure and specific volume are computed as before using (3.5) and (3.4).

The variable $\tau(z)$ defines the vertical structure of the damping layer, and has a form similar to the Rayleigh damper in Durran and Klemp (1983) and also used in the traditional Rayleigh damping formulation discussed in Section 4.4.3

$$\tau(z) = \begin{cases} \gamma_r \sin^2\left[\frac{\pi}{2}\left(1 - \frac{z_{top}-z}{z_d}\right)\right] & \text{for } z \geq (z_{top} - z_d); \\ 0 & \text{otherwise,} \end{cases}$$

where γ_r is a user specified damping coeficient, z_{top} is the height of the model top for a particular grid column, and z_d is the depth of the damping layer (from the model top). A typical value for the damping coefficient for this formulation is $\gamma_r = 0.2\,s^{-1}$ ($\sim 10N$ for typical stratospheric values of the Brunt-Väisällä frequency). A complete analysis of this filter can be found in Klemp et al. (2008).

4.4.3   Traditional Rayleigh Damping Layer

A traditional Rayleigh damping layer is also available in the ARW solver. This scheme applies a tendency to u, v, w, and θ to gradually relax the variable back to a predetermined reference state value,

$$\begin{aligned} \partial_t u &= -\tau(z)\left(u - \overline{u}\right), \\ \partial_t v &= -\tau(z)\left(v - \overline{v}\right), \\ \partial_t w &= -\tau(z)w, \\ \partial_t \theta &= -\tau(z)\left(\theta - \overline{\theta}\right). \end{aligned}$$

Overbars indicate the reference state fields, which are functions of z only and are typically defined as the initial horizontally homogeneous fields in idealized simulations. The reference state vertical velocity is assumed to be zero. The vertical structure of the damping layer is the same as that used for the implicit vertical velocity damping described in Section 4.4.2. Because the model surfaces change height with time in the ARW solver, the reference state values at each grid point need to be recalculated at every time step. Thus, a linear interpolation scheme

38

is used to calculate updated reference state values based on the height of the model levels at each time step.

The effect of this filter on gravity waves is discussed in Klemp and Lilly (1978), where guidance on the choice of the damping coefficeint γ_r can also be found.

4.5 Other Damping

4.5.1 Vertical-Velocity Damping

This is also called w-damping. In semi-operational or operational NWP applications, the model robustness can be improved by detecting locations where the vertical motion approaches the limiting Courant number for stability, and applying a Rayleigh damping term in the vertical momentum equation to stabilize the motion. This term is non-physical and should only be used in the situation where many, or long, model runs are being done, and there is no option for a re-run with a shorter time-step if a failure occurs due to an excessively strong updraft. This might be the case, for example, in an operational setting where real-time forecasts have to be produced on time to be useful. However, if this term activates frequently, consideration should be given to reducing the model time-step.

The term is calculated from

$$Cr = \left| \frac{\Omega dt}{\mu d\eta} \right|.$$

If $Cr > Cr_\beta$, then

$$\partial_t W = ... - \mu_d \operatorname{sign}(W)\gamma_w(Cr - Cr_\beta),$$

where γ_w is the damping coefficient (typically 0.3 ms^{-2}), and Cr_β is the activation Courant number (typically 1.0). The ARW outputs the location of this damping when it is active.

Chapter 5

Initial Conditions

The ARW may be run with user-defined initial conditions for idealized simulations, or it may be run using interpolated data from either an external analysis or forecast for real-data cases. Both 2D and 3D tests cases for idealized simulations are provided. Several sample cases for real-data simulations are provided, which rely on pre-processing from an external package (usually the WRF Preprocessor System, referred to as WPS) that converts the large-scale GriB data into a format suitable for ingest by the ARW's real-data processor.

The programs that generate the specific initial conditions for the selected idealized or real-data case function similarly. They provide the ARW with:

- input data that is on the correct horizontal and vertical staggering;
- hydrostatically balanced reference state and perturbation fields; and
- metadata specifying such information as the date, grid physical characteristics, and projection details.

For neither the idealized nor the real-data cases are the initial conditions enhanced with observations. However, output from the ARW system initial condition programs is suitable as input to the WRF variational assimilation package (see Chapter 9).

5.1 Initialization for Idealized Conditions

The ARW comes with a number of test cases using idealized environments, including large eddy simulations (em_les), sea breezes (em_seabreeze2d_x), mountain waves (em_hill2d_x), squall lines (em_squall2d_x, em_squall2d_y), supercell thunderstorms (em_quarter_ss), gravity currents (em_grav2d_x), baroclinic waves (em_b_wave), and global domains (em_heldsuarez). A brief description of these test cases can be found in the README_test_cases file provided in the ARW release. The test cases include examples of atmospheric flows at fine scales (e.g., the LES example has a grid-spacing of 100 meters and a time step of 1 second) and examples of flow at large scales (e.g., the Held Suarez global test case uses a grid-spacing around 600 km and a time step of 1800 s), in addition to the traditional mesoscale and cloudscale model simulations. The test suite allows an ARW user to easily reproduce these known solutions. The test suite is also the starting point for constructing idealized flow simulations by modifying initializations that closely resemble a desired initialization.

Most of these tests use as input a 1D sounding specified as a function of geometric height z (except for the baroclinic wave case that uses a 2D profile specified in $[y, z]$), and, with the

exception of the baroclinic wave test case, the sounding files are in text format that can be directly edited by the user. The 1D specification of the sounding in these test files requires the surface values of pressure, potential temperature, and water vapor mixing ratio, followed by the potential temperature, vapor mixing ratio, and horizontal wind components at some heights above the surface. The initialization programs for each case assume that this moist sounding represents an atmosphere in hydrostatic balance.

Two sets of thermodynamic fields are needed for the model— the reference state and the perturbation state (see Chapter 2 for discussion of the equations). The reference state used in the idealized initializations is computed using the input sounding from which the moisture is discarded (because the reference state is dry). The perturbation state is computed using the full moist input sounding. The procedure for computing the hydrostatically-balanced ARW reference and perturbation state variables from the input sounding is as follows. First, density and both a dry and full hydrostatic pressure are computed from the input sounding at the input sounding levels z. This is accomplished by integrating the hydrostatic equation vertically up the column using the surface pressure and potential temperature as the lower boundary condition. The hydrostatic equation is

$$\delta_z p = -\overline{\rho}^z g (1 + (R_d/R_v)\overline{q}_v{}^z),\tag{5.1}$$

where $\overline{\rho}^z$ is a two point average between input sounding levels, and $\delta_z p$ is the difference of the pressure between input sounding levels divided by the height difference. Additionally, the equation of state is needed to close the system:

$$\alpha_d = \frac{1}{\rho_d} = \frac{R_d\theta}{p_o}\left(1 + \frac{R_d}{R_v}q_v\right)\left(\frac{p}{p_o}\right)^{-\frac{c_v}{c_p}},\tag{5.2}$$

where q_v and θ are given in the input sounding. (5.1) and (5.2) are a coupled set of nonlinear equations for p and ρ in the vertical integration, and they are solved by iteration. The dry pressure on input sounding levels is computed by integrating the hydrostatic relation down from the top, excluding the vapor component.

Having computed the full pressure (dry plus vapor) and dry air pressure on the input sounding levels, the pressure at the model top (p_{dht}) is computed by linear interpolation in height (or possibly extrapolation) given the height of the model top (an input variable). The column mass μ_d is computed by interpolating the dry air pressure to the surface and subtracting from it p_{dht}. Given the column mass, the dry-air pressure at each η level is known from the coordinate definition (2.1), repeated here

$$\eta = (p_{dh} - p_{dht})/\mu_d \qquad \text{where} \quad \mu_d = p_{dhs} - p_{dht},$$

and the pressures p_{dhs} and p_{dht} refer to the dry atmosphere. The potential temperature from the input sounding is interpolated to each of the model pressure levels, and the equation of state (5.2) is used to compute the inverse density α_d. Finally, the ARW's hydrostatic relation (2.9), in discrete form

$$\delta_\eta \phi = -\alpha_d \mu_d$$

is used to compute the geopotential. This procedure is used to compute the reference state (assuming a dry atmosphere) and the full state (using the full moist sounding). The perturbation variables are computed as the difference between the reference and full state. It should also be

noted that in the nonhydrostatic model integration, the inverse density α_d is diagnosed from the geopotential using this equation of state, and the pressure is diagnosed from the equation of state using the inverse density α_d and the prognostic potential temperature θ. Thus, the ARW's prognostic variables μ_d, θ, and ϕ are in exact hydrostatic balance for the model equations (to machine roundoff).

5.2   Initialization for Real-Data Conditions

The initial conditions for the real-data cases are pre-processed through a separate package called the WRF Preprocessing System (WPS, see Fig. 5.1). The output from WPS is passed to the real-data pre-processor in the ARW— program *real*— which generates initial and lateral boundary conditions. This section is primarily about the steps taken to build the initial and the lateral boundary conditions for a real-data case. Even though the WPS is outside of the ARW system, a brief description is appropriate to see how the raw meteorological and static terrestrial data are brought into the model for real-data cases.

5.2.1   Use of the WRF Preprocessing System by the ARW

The WPS is a set of programs that takes terrestrial and meteorological data (typically in GriB format) and transforms them for input to the ARW pre-processor program for real-data cases (*real*). Figure 5.1 shows the flow of data into and out of the WPS system. The first step for the WPS is to define a physical grid (including the projection type, location on the globe, number of grid points, nest locations, and grid distances) and to interpolate static fields to the prescribed domain. Independent of the domain configuration, an external analysis or forecast is processed by the WPS GriB decoder, which diagnoses required fields and reformats the GriB data into an internal binary format. With a specified domain, WPS horizontally interpolates the meteorological data onto the projected domain(s). The output data from WPS supplies a complete 3-dimensional snapshot of the atmosphere on the selected model grid's horizontal staggering at the selected time slices, which is sent to the ARW pre-processor program for real-data cases.

The input to the ARW real-data processor from WPS contains 3-dimensional fields (including the surface) of temperature (K), relative humidity (and the horizontal components of momentum (m/s, already rotated to the model projection). The 2-dimensional static terrestrial fields include: albedo, Coriolis parameters, terrain elevation, vegetation/land-use type, land/water mask, map scale factors, map rotation angle, soil texture category, vegetation greenness fraction, annual mean temperature, and latitude/longitude. The 2-dimensional time-dependent fields from the external model, after processing by WPS, include: surface pressure and sea-level pressure (Pa), layers of soil temperature (K) and soil moisture (kg/kg, either total moisture, or binned into total and liquid content), snow depth (m), skin temperature (K), sea surface temperature (K), and a sea ice flag.

5.2.2   Reference State

Identical to the idealized initializations, there is a partitioning of some of the meteorological data into reference and perturbation fields. For real-data cases, the reference state is defined by
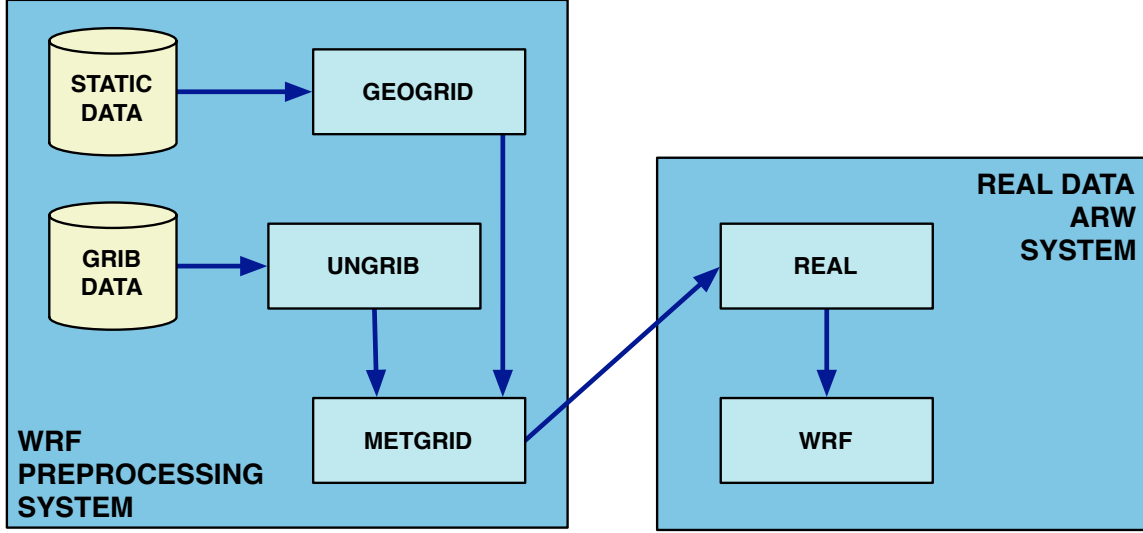
Figure 5.1: Schematic showing the data flow and program components in WPS, and how WPS feeds initial data to the ARW. Letters in the rectangular boxes indicate program names. GEOGRID: defines the model domain and creates static files of terrestrial data. UNGRIB: decodes GriB data. METGRID: interpolates meteorological data to the model domain.

terrain elevation and three constants:

- p_0 (10^5 Pa) reference sea level pressure;
- T_0 (usually 270 to 300 K) reference sea level temperature; and
- A (50 K) temperature difference between the pressure levels of p_0 and p_0/e.

Using these parameters, the dry reference state surface pressure is

$$p_{dhs} = p_0 \ exp\left(\frac{-T_0}{A} + \sqrt{\left(\frac{T_0}{A}\right)^2 - \frac{2\phi_{sfc}}{A \ R_d}}\right). \tag{5.3}$$

From (5.3), the 3-dimensional reference pressure (dry hydrostatic pressure p_{dh}) is computed as a function of the vertical coordinate η levels and the model top p_{dht}:

$$p_{dh} = \overline{p}_d = \eta \ (p_{dhs} - p_{dht}) + p_{dht}. \tag{5.4}$$

With (5.4), the reference temperature is a straight line on a skew-T plot, defined as

$$T = T_0 + A \ ln\frac{\overline{p}_d}{p_0}.$$

From the reference temperature and pressure, the reference potential temperature is then defined as

$$\overline{\theta}_d = \left(T_0 + A \ ln\frac{\overline{p}_d}{p_0}\right)\left(\frac{p_0}{\overline{p}_d}\right)^{\frac{R_d}{C_p}}, \tag{5.5}$$

44

and the reciprocal of the reference density using (5.4) and (5.5) is given by

$$\overline{\alpha}_d = \frac{1}{\overline{\rho}_d} = \frac{R_d \,\overline{\theta}_d}{p_0} \left(\frac{\overline{p}_d}{p_0} \right)^{-\frac{C_v}{C_p}}.$$ (5.6)

The base state difference of the dry surface pressure from (5.3) and the model top is given as

$$\overline{\mu}_d = p_{dhs} - p_{dht}.$$ (5.7)

From (5.6) and (5.7), the reference state geopotential defined from the hydrostatic relation is

$$\delta_\eta \overline{\phi} = -\overline{\alpha}_d \,\overline{\mu}_d.$$

5.2.3 Vertical Interpolation and Extrapolation

The ARW real-data preprocessor vertically interpolates using functions of dry pressure. The input data from WPS contains both a total pressure and a moisture field (typically relative humidity). Starting at the top each column of input pressure data, the integrated moisture is subtracted from the pressure field step-wise down to the surface. Then, by removing the pressure at the model lid, the total dry surface pressure p_{sd} diagnosed from WPS defines the model total dry column pressure

$$\mu_d = \overline{\mu}_d + \mu_d' = p_{sd} - p_{dht}.$$ (5.8)

With the ARW vertical coordinate η, the model lid p_{dht}, and the column dry pressure known at each (i, j, k) location, the 3-dimensional arrays are interpolated.

In the free atmosphere up to the model lid, the vertical calculations are always interpolations. However, near the model surface, it is possible to have an inconsistency between the input surface pressure (based largely on the input surface elevation) and the ARW surface pressure (possibly with a much higher resolution topography). These inconsistencies may lead to an extrapolation. The default behavior for extrapolating the horizontal winds and the relative humidity below the known surface is to keep the values constant, with zero vertical gradient. For the potential temperature, by default a -6.5 K/km lapse rate for the temperature is applied. The vertical interpolation of the geopotential field is optional and is handled separately. Since a known lower boundary condition exists (the geopotential is defined as zero at the pressure at sea-level), no extrapolation is required.

5.2.4 Perturbation State

In the real-data preprocessor, first a topographically defined reference state is computed, then the input 3-dimensional data are vertically interpolated in dry pressure space. With the potential temperature θ and mixing ratio q_v available on each η level, the pressure, density, and height diagnostics are handled. The perturbation dry column pressure field given the reference dry column pressure (5.7) is

$$\mu_d' = \mu_d - \overline{\mu}_d,$$ (5.9)

where μ_d is the column total dry pressure. Starting with the reference state fields (5.4, 5.6, and (5.7)) and the dry surface pressure perturbation (5.9), the perturbation fields for pressure and

inverse density are diagnosed. The pressure perturbation includes moisture and is diagnosed from the hydrostatic equation

$$\delta_\eta p' = \mu'_d \left(1 + \overline{q_v}^\eta\right) + \overline{q_v}^\eta\, \overline{\mu}_d,$$

which is integrated down from at the model top (where $p' = 0$) to recover p'. The total dry inverse density is given as

$$\alpha_d = \frac{R_d}{p_0}\, \theta\, \left(1 + \frac{R_v}{R_d} q_v\right) \left(\frac{p'_d + \overline{p}_d}{p_0}\right)^{-\frac{C_v}{C_p}},$$

which defines the perturbation field for inverse density

$$\alpha'_d = \alpha_d - \overline{\alpha}_d.$$

The perturbation geopotential is diagnosed from the hydrostatic relation

$$\delta_\eta \phi' = -\left(\mu_d \alpha'_d + \mu'_d \overline{\alpha}_d\right)$$

by upward integration using the terrain elevation as the lower boundary condition.

5.2.5   Generating Lateral Boundary Data

This section deals with generating the separate lateral boundary condition file used exclusively for the real-data cases. For information on which lateral boundary options are available for both the idealized and real-data cases, see Chapter (6).

   The specified lateral boundary condition for the coarse grid for real-data cases is supplied by an external file that is generated by program *real*. This file contains records for the fields u, v, θ, q_v, ϕ', and μ'_d that are used by the ARW to constrain the lateral boundaries (other fields are in the boundary file, but are not used). The lateral boundary file holds one less time period than was processed by WPS. Each of these variables has both a valid value at the initial time of the lateral boundary time and a tendency term to get to the next boundary time period. For example, assuming a 3-hourly availability of data from WPS, the first time period of the lateral boundary file for u would contain data for both coupled u (map scale factor and μ_d interpolated to the variable's staggering) at the 0 h time

$$U_{0h} = \left.\frac{\overline{\mu_d}^x u}{\overline{m}^x}\right|_{0h},$$

and a tendency value defined as

$$U_t = \frac{U_{3h} - U_{0h}}{3h},$$

which would take a grid point from the initial value to the value at the next large-scale time during 3 simulation hours. The horizontal momentum fields are coupled both with μ_d and the inverse map factor. The other 3-dimensional fields (θ, q_v, and ϕ') are coupled only with μ_d. The 2-dimensional μ'_d lateral boundary field is not coupled.

Each lateral boundary field is defined along the four sides of the rectangular grid (loosely referred to as the north, south, east, and west sides). The boundary values and tendencies for vertical velocity and the non-vapor moisture species are included in the external lateral boundary file, but act as place-holders for the nested boundary data for the fine grids. The width of the lateral boundary along each of the four sides is user selectable at run-time.

5.2.6   Masking of Surface Fields

Some of the meteorological and static fields are "masked". A masked field is one in which the values are typically defined only over water (e.g., sea surface temperature) or defined only over land (e.g., soil temperature). The need to match all of the masked fields consistently to each other requires additional steps for the real-data cases due to the masked data's presumed use in various physics packages in the soil, at the surface, and in the boundary layer. If the land/water mask for a location is flagged as a water point, then the vegetation and soil categories must also recognize the location as the special water flag for each of their respective categorical indices. Similarly, if the land/water mask is flagged as a land point, the vegetation and soil categories must be assigned to one of the available land indices.

The values for the soil temperature and soil moisture come from WPS on the native levels originally defined for those variables by an external model. WPS does no vertical interpolation for the soil data. While it is typical to try to match the ARW soil scheme with the incoming data, that is not a requirement. Pre-processor *real* will vertically interpolate (linear in depth below the ground) from the incoming levels to the requested soil layers to be used within the model.

5.3   Digital Filtering Initialization

Version 3 of the ARW provides a digital filtering initialization (DFI) to remove noise, which results from imbalances between mass and wind fields, from the model initial state. DFI is applied to the output of the *real* preprocessor before the model simulation begins. If data assimilation is performed using WRF-Var, DFI is applied to the analysis produced by the WRF-Var system, rather than the output of program *real*.

Under the assumption that any noise is of higher frequency than meteorologically significant modes, DFI attempts to remove this noise by filtering all oscillations above a specified cutoff frequency. Accordingly, the filters in the ARW DFI are low-pass digital filters, which are applied to time series of model fields; the *initialized* model state is the output of the filter at some prescribed time, e.g., the analysis time. Time series of model states are generated through combinations of adiabatic, backward integration and diabatic, forward integration in the model, with the choice of DFI scheme determining the specific combination of integrations. Three DFI schemes — digital filter launch (DFL; Lynch and Huang (1994)), diabatic DFI (DDFI; Huang and Lynch (1993)), and twice DFI (TDFI; Lynch and Huang (1994)) — are available.

5.3.1 Filter Design

In the ARW DFI, either nonrecursive (i.e., finite impulse response) digital filters or a recursive (i.e., infinite impulse response) digital filter may be used. The coefficients for the nonrecursive digital filters may be computed according to one of two methods, while the coefficients for the recursive filter are computed according to a single method.

A general nonrecursive digital filter is of the form

$$y_n = \sum_{k=-N}^{N} h_k x_{n-k}, \tag{5.10}$$

where y_n is the output of the filter at time n, the h_k are the coefficients of the filter, and $\{\ldots, x_{n-1}, x_n, x_{n+1}, \ldots\}$ is the sequence of input values to be filtered; such a filter is said to have span $2N + 1$.

One method for deriving the coefficients of a nonrecursive digital filter is the windowed-sinc method, described in the context of DFI by Lynch and Huang (1992). In the ARW DFI, either the Lanczos, Hamming, Blackman, Kaiser, Potter, or Dolph-Chebyshev windows may be used; the Dolph-Chebyshev window is described by Lynch (1997). However, when a filter with a shorter span is desired, another nonrecursive digital filter, the Dolph filter, may be used. Lynch (1997) describes the construction of the Dolph filter, and demonstrates that this filter has properties nearly indistinguishable from those of an optimal filter, which minimizes the maximum difference between a filter's transfer function and an ideal transfer function in the pass and stop bands.

The only recursive filter in the ARW DFI is the second-order Quick-Start filter of Lynch and Huang (1994). In general, a recursive digital filter that depends only on past and present values of the input, and on past values of the output, is of the form

$$y_n = \sum_{k=0}^{N} h_k x_{n-k} + \sum_{k=1}^{N} b_k y_{n-k}. \tag{5.11}$$

However, this form is inconvenient when the inputs to the filter consist of model states, and we wish to avoid storing many such states. Lynch and Huang (1994) show how this type of recursive filter can be reformulated to have the same form as a nonrecursive filter, and thus, we can think of the second-order Quick-Start filter as having the same form as (5.10).

5.3.2 DFI Schemes

The ARW supports three different DFI schemes, illustrated graphically in Fig. 5.2. The DFL scheme produces an initialized model state valid some time after the model analysis time, while the DDFI and TDFI schemes produce initialized states valid at the analysis time.

DFL

In the DFL scheme, forward integration with full model physics and diffusion begins at the initial time and continues for $2N$ time steps, during which time a filtered model state valid N time steps beyond the analysis time is computed as in (5.10). Then, the initialized simulation
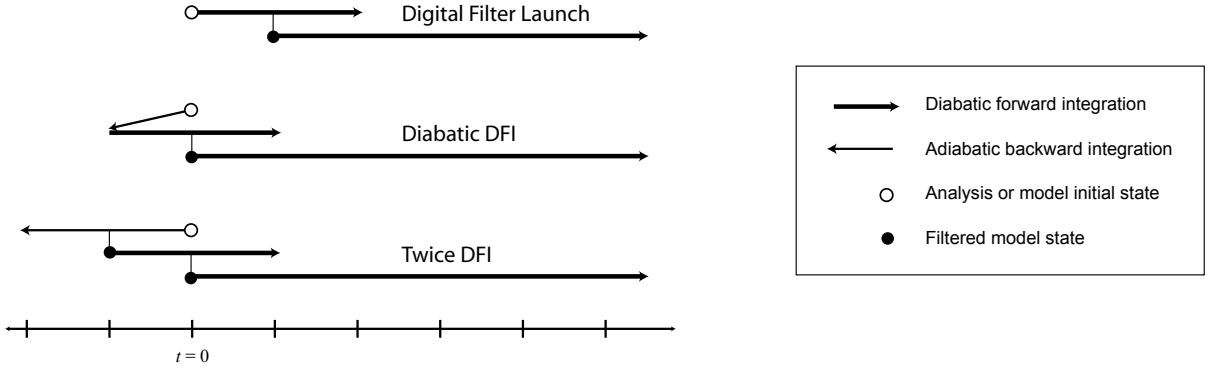
Figure 5.2: An illustration showing the three available DFI schemes: digital filter launch, diabatic digital filter initialization, and twice digital filter initialization.

is launched from the midpoint of the filtering period. For any model state $\mathbf{X}$, let $[\mathbf{X}]_n^D$ give the model state after diabatically integrating n time steps forward in time; we emphasize that the superscript D indicates diabatic integration, in contrast to adiabatic integration. Then, the DFL scheme is expressed as

$$\mathbf{X}_{ini} = \sum_{n=0}^{2N} h_n \left[\mathbf{X}_{ana}\right]_n^D ,$$

(5.12)

where $\mathbf{X}_{ini}$ is the initialized model state, $\mathbf{X}_{ana}$ is the model analysis or model initial state generated by the *real* preprocessor, and the h_n are the filter coefficients.

DDFI

To produce an initialized state valid at the model analysis time, the DDFI scheme begins with an adiabatic, backward integration for N time steps, followed by a diabatic, forward integration for $2N$ time steps, during which filtering takes place. This filtered state is valid at the model analysis time. Letting $\left[\mathbf{X}_{ana}\right]_{-n}^A$ denote the model state after adiabatic, backward integration for n time steps from the model analysis or model initial state, $\mathbf{X}_{ana}$, the DDFI scheme is expressed as

$$\mathbf{X}_{ini} = \sum_{n=0}^{2N} h_n \left[\left[\mathbf{X}_{ana}\right]_{-n}^A\right]_n^D ,$$

(5.13)

where $\mathbf{X}_{ini}$ is the initialized model state valid at the model analysis time.

TDFI

The TDFI scheme involves two applications of the digital filter. Adiabatic, backward integration proceeds from the model initial time for $2N$ time steps, during which a filter is applied. The filtered state is valid at time $-N\Delta t$; from this filtered state, a forward, diabatic integration is

49

launched. The second integration proceeds for $2N$ time steps, during which a second filter is applied, giving a filtered model state valid at this model analysis time. The TDFI scheme is expressed as

$$\mathbf{X}_{ini} = \sum_{n=0}^{2N} h_n \left[\sum_{n'=0}^{2N} h_{n'} \left[\mathbf{X}_{ana}\right]_{-n}^{A} \right]_{n}^{D}. \tag{5.14}$$

5.3.3 Backward Integration

To diabatically integrate backward in time, it suffices to disable all diabatic processes and to negate the model time step, Δt, as well as the sign of the horizontal velocity, U, in the odd-order advection operators of Section 3.2.3, which become

3rd order: $(\overline{q}^{x_{adv}})_{i-1/2} = (\overline{q}^{x_{adv}})_{i-1/2}^{4th}$

$$- \operatorname{sign}(U) \frac{1}{12} \left[(q_{i+1} - q_{i-2}) - 3(q_i - q_{i-1}) \right]$$

5th order: $(\overline{q}^{x_{adv}})_{i-1/2} = (\overline{q}^{x_{adv}})_{i-1/2}^{6th}$

$$+ \operatorname{sign}(U) \frac{1}{60} \left[(q_{i+2} - q_{i-3}) - 5(q_{i+1} - q_{i-2}) + 10(q_i - q_{i-1}) \right].$$

When specified boundary conditions are used, as in Section 6.4, the model boundaries before the model initial time are taken to be the same as those valid at the model initial time. We note that, with a negated time step, the linear ramping functions F_1 and F_2 of (6.1) change sign, and, consequently, so does the sign of the tendency for a prognostic variable ψ.

Chapter 6

Lateral Boundary Conditions

Several lateral boundary condition options exist for the ARW that are suitable for idealized flows, and a specified lateral boundary condition for real-data simulations is available. These choices are handled via a run-time option in the Fortran namelist file. For nesting, all fine domains use the nest time-dependent lateral boundary condition where the outer row and column of the fine grid is specified from the parent domain, described in Section 7.3. The remaining lateral boundary options are exclusively for use by the most coarse/parent domain.

6.1 Periodic Lateral Boundary Conditions

Periodic lateral boundary conditions in the ARW can be specified as periodic in x (west-east), y (south-north), or doubly periodic in (x, y). The periodic boundary conditions constrain the solutions to be periodic; that is, a generic model state variable ψ will follow the relation

$$\psi(x + nL_x, y + mL_y) = \psi(x, y)$$

for all integer (n, m). The periodicity lengths (L_x, L_y) are
[(dimension of the domain in x) - 1]Δx and [(dimension of the domain in y) - 1]Δy.

6.2 Open Lateral Boundary Conditions

Open lateral boundary conditions, also referred to as gravity-wave radiating boundary conditions, can be specified for the west, east, north, or south boundary, or any combination thereof. The gravity wave radiation conditions follow the approach of Klemp and Lilly (1978) and Klemp and Wilhelmson (1978).

There are a number of changes in the base numerical algorithm described in Chapter 3 that accompany the imposition of these conditions. First, for the normal horizontal velocities along a boundary on which the condition is specified, the momentum equation for the horizontal velocity, (3.7) or (3.8), is replaced by

$$\delta_\tau U'' = -U^* \delta_x u,$$

where $U^* = \min(U - c_b, 0)$ at the $x = 0$ (western) boundary, $U^* = \max(U + c_b, 0)$ at the $x = L$ (eastern) boundary, and likewise for the south and north boundaries for the V momentum. The

horizontal difference operator δ_x is evaluated in a one-sided manner using the difference between the boundary value and the value one grid-point into the grid from the boundary. c_b is the phase speed of the gravity waves that are to be radiated; it is specified as a model constant (for more details see Klemp and Lilly, 1978; Klemp and Wilhelmson, 1978).

For scalars and non-normal momentum variables, the boundary-perpendicular flux divergence term is replaced with

$$\delta_x(U\psi) = U^*\delta_x\psi + \psi\ \delta_x U,$$

where $U^* = \min(U, 0)$ at the $x = 0 + \Delta x/2$ (western) scalar boundary, $U^* = \max(U, 0)$ at the $x = L - \Delta x/2$ (eastern) boundary, and likewise for the south and north boundaries using V. As was the case for the momentum equations, the horizontal difference operator δ_x is evaluated in a one-sided manner using the difference between the boundary value and the value one grid-point into the grid from the boundary.

6.3 Symmetric Lateral Boundary Conditions

Symmetry lateral boundary conditions can be specified for the west, east, north, or south boundary, or any combination thereof. The symmetry boundaries are located on the normal-velocity planes at the lateral edges of the grids. The normal velocities are zero at these boundaries, and on either side of the boundary the normal velocity satisfies the relation

$$U_\perp(x_b - x) = -U_\perp(x_b + x),$$

where x_b is the location of the symmetry boundary. All other variables satisfy the relation

$$\psi(x_b - x) = \psi(x_b + x).$$

6.4 Specified Lateral Boundary Conditions

Primarily for real-data cases, the specified boundary condition is also referred to as a relaxation, or nudging, boundary condition. There are two uses of the specified boundaries in the ARW: for the outer-most coarse grid or for the time-dependent boundaries supplied to a nested grid. The specified lateral boundary conditions for the nest are automatically selected for all of the fine grids, even if the coarse grid is using combinations of the symmetry, periodic, or open options. If the specified lateral boundary condition is selected for the coarse grid, then all four grid sides (west, east, north, and south) use specified lateral conditions. However, in tropical channel mode, where the domain wraps completely around the equator, it is possible to combine specified boundary conditions with periodic conditions in the x direction. Note that care is needed in setting the domain up such that the points exactly match longitude at the east and west boundaries when periodic conditions are used in real-data cases. Also note that a Mercator projection is needed to make this possible.

The coarse grid specified lateral boundary is comprised of both a specified and a relaxation zone (as shown in Fig. 6.1). For the coarse grid, the specified zone is determined entirely by temporal interpolation from an external forecast or analysis (supplied by WPS). The width of the specified zone is run-time configurable, but is typically set to 1 (i.e., the last row and column

Figure 6.1: Specified and relaxation zones for a grid with a single specified row and column, and four rows and columns for the relaxation zone. These are typical values used for a specified lateral boundary condition for a real-data case.

along the outer edge of the most coarse grid is entirely specified by temporal interpolation using data from an external model). The second region of the lateral boundary for the coarse grid is the relaxation zone. The relaxation zone is where the model is nudged or relaxed towards the large-scale forecast (e.g., rows and columns 2 through 5 in Fig. 6.1). The size of the relaxation zone is a run-time option.

The specified lateral boundary condition for the coarse grid requires an external file, generated during the same pre-processing as the initial condition file. Let ψ be any prognostic value having a lateral boundary entry, after Davies and Turner (1977),

$$\partial_t \psi \big|_n = F_1(\psi_{LS} - \psi) - F_2 \Delta^2 (\psi_{LS} - \psi), \qquad (6.1)$$

where n is the number of grid points in from the outer row or column along the boundary ($SpecZone + 1 \leq n \leq SpecZone + RelaxZone - 1$; see Fig. 6.1) and ψ_{LS} is the large-scale value obtained by spatial and temporal interpolation from the external analysis or model forecast by WPS . Δ^2 is a 5-point horizontal smoother applied along η-surfaces. The weighting function coefficients F_1 and F_2 in (6.1) are given by

$$F_1 = \frac{1}{10\Delta t} \frac{SpecZone + RelaxZone - n}{RelaxZone - 1},$$

$$F_2 = \frac{1}{50\Delta t} \frac{SpecZone + RelaxZone - n}{RelaxZone - 1},$$

where n extends only through the relaxation zone ($SpecZone + 1 \leq n \leq SpecZone + RelaxZone - 1$). F_1 and F_2 are linear ramping functions with a maximum at the first relaxation row or column

nearest the coarse grid boundary (just inside of the specified zone). In Version 3.0 these linear functions can optionally be multiplied by an exponential function for smoother behavior when broad boundary zones are needed. This is achieved through an additional multiplier.

$$F_1 = \frac{1}{10\Delta t} \frac{SpecZone + RelaxZone - n}{RelaxZone - 1} \exp[-SpecExp(n - SpecZone - 1)]$$

$$F_2 = \frac{1}{50\Delta t} \frac{SpecZone + RelaxZone - n}{RelaxZone - 1} \exp[-SpecExp(n - SpecZone - 1)]$$

where $SpecExp$ is an inverse length scale in grid lengths.

On the coarse grid, the specified boundary condition applies to the horizontal wind components, potential temperature, ϕ', μ_d', and water vapor. The lateral boundary file contains enough information to update the boundary zone values through the entire simulation period. The momentum fields are coupled with μ_d and the inverse map factor (both at the specific variable's horizontal staggering location), and the other 3-dimensional fields are coupled with μ_d. The μ_d' field is not coupled in the lateral boundary file.

Vertical velocity has a zero gradient boundary condition applied in the specified zone (usually the outer-most row and column). Microphysical variables, except vapor, and all other scalars have flow-dependent boundary conditions applied in the specified zone. This boundary condition specifies zero on inflow and zero-gradient on outflow. Since these boundary conditions require only information from the interior of the grid, these variables are not in the specified boundary condition file. However, for nested boundaries, microphysical variables and scalars are also available from the parent domain, and use same relaxation towards interpolated variables as the dynamic variables.

6.5 Polar Conditions

See subsection for details on how the polar boundary condition is applied.

Chapter 7

Nesting

The ARW supports horizontal nesting that allows resolution to be focused over a region of interest by introducing an additional grid (or grids) into the simulation. In the current implementation, only horizontal refinement is available: there is no vertical nesting option. The nested grids are rectangular and are aligned with the parent (coarser) grid within which they are nested. Additionally, the nested grids allow any integer spatial ($\Delta x_{coarse}/\Delta x_{fine}$) and temporal refinements of the parent grid (the spatial and temporal refinements are usually, but not necessarily the same). This nesting implementation is in many ways similar to the implementations in other mesoscale and cloudscale models (e.g. MM5, ARPS, COAMPS). The major improvement in the ARW's nesting infrastruture compared with techniques used in other models is the ability to compute nested simulations efficiently on parallel distributed-memory computer systems, which includes support for moving nested grids. The WRF Software Framework, described in Michalakes et al. (2004), makes these advances possible. In this chapter we describe the various nesting options available in the ARW and the numerical coupling between the grids.

7.1 Nesting Options

1-Way and 2-Way Grid Nesting

Nested grid simulations can be produced using either 1-way nesting or 2-way nesting as outlined in Fig. 7.1. The 1-way and 2-way nesting options refer to how a coarse grid and the fine grid interact. In both the 1-way and 2-way simulation modes, the fine grid boundary conditions (i.e., the lateral boundaries) are interpolated from the coarse grid forecast. In a 1-way nest, this is the only information exchange between the grids (from the coarse grid to the fine grid). Hence, the name *1-way nesting*. In the 2-way nest integration, the fine grid solution replaces the coarse grid solution for coarse grid points that lie inside the fine grid. This information exchange between the grids is now in both directions (coarse-to-fine for the fine-grid lateral boundary computation and fine-to-coarse during the feedback at each coarse-grid time step). Hence, the name *2-way nesting*.

The 1-way nest set-up may be run in one of two different methods. One option is to produce the nested simulation as two separate ARW simulations as described in the leftmost box in Fig. 7.1. In this mode, the coarse grid is integrated first and the coarse grid forecast is completed. Output from the coarse grid integration is then processed to provide boundary conditions for the nested run (usually at a much lower temporal frequency than the coarse grid time step), and
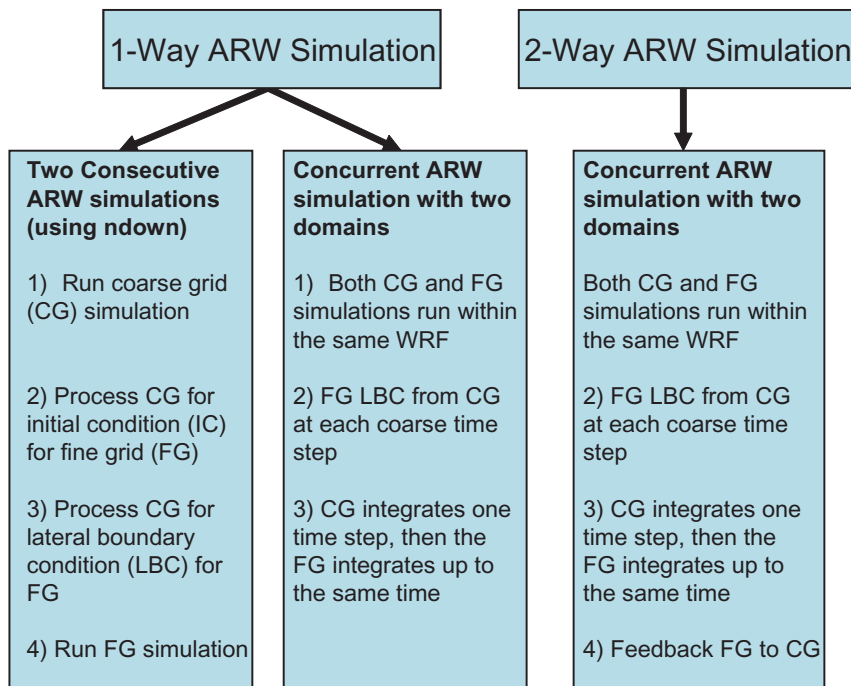
Figure 7.1: 1-way and 2-way nesting options in the ARW.

this is followed by the complete time integration of fine (nested) grid. Hence, this 1-way option is equivalent to running two separate simulations with a processing step in between. Also with separate grid simulations, an intermediate re-analysis (such as via 3D-Var, see Section 9) can be included.

The second 1-way option (lockstep with no feedback), depicted in the middle box in Fig. 7.1, is run as a traditional simulation with two (or more) grids integrating concurrently, except with the feedback runtime option shut off. This option provides lateral boundary conditions to the fine grid at each coarse grid time step, which is an advantage of the concurrent 1-way method (no feedback).

Fine Grid Initialization Options

The ARW supports several strategies to refine a coarse-grid simulation with the introduction of a nested grid. When using concurrent 1-way and 2-way nesting, several options for initializing the fine grid are provided.

- All of the fine grid variables (both meteorological and terrestrial) can be interpolated from the coarse grid (useful when a fine grid starts later in the coarse-grid forecast).
- All of the fine grid variables can be input from an external file which has high-resolution information for both the meteorological and the terrestrial fields (a standard set-up when the fine-grid terrestrial fields are expected to impact the forecast).
- The fine grid can have some of the variables initialized with a high-resolution external data set, while other variables are interpolated from the coarse grid (for example this would permit the improved analysis from the 3D-Var initialization of the coarse grid's
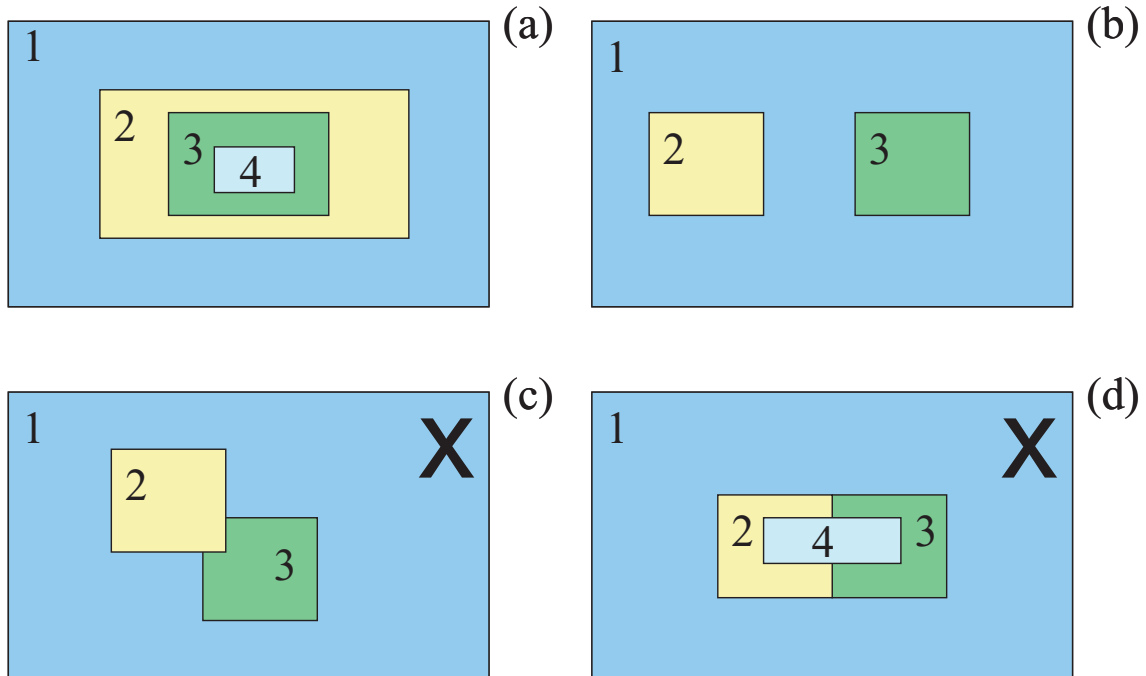
Figure 7.2: Various nest configurations for multiple grids. (a) Telescoping nests. (b) Nests at the same level with respect to a parent grid. (c) Overlapping grids: not allowed (d) Inner-most grid has more than one parent grid: not allowed

  meteorological fields to remain consistent with the fine grid). This option allows the fine grid to start later in the coarse-grid's forecast, but with the advantage of higher-resolution static fields.

- For a moving nest, an external orography file may be used to update the fine grid terrain elevation.

These fine grid initialization settings are user specified at run-time, and the ARW allows nested grids to instantiate and cease during any time that the fine grid's parent is still integrating.

Possible Grid Configurations

A simulation involves one outer grid and may contain multiple inner nested grids. In the ARW, each nested region is entirely contained within a single coarser grid, referred to as the *parent* grid. The finer, nested grids are referred to as *child* grids. Using this terminology, children are also parents when multiple levels of nesting are used. The fine grids may be telescoped to any depth (i.e., a parent grid may contain one or more child grids, each of which in turn may successively contain one or more child grids; Fig. 7.2a), and several fine grids may share the same parent at the same level of nesting (Fig. 7.2b). Any valid fine grid may either be a static domain or it may be a moving nest (with either prescribed incremental shifts or with automatic moves via a vortex following algorithm, such as tracking the minimum of the 500 mb height). The ARW does not permit overlapping grids, where a coarse grid point is contained within more than a single child grid (i.e., both of which are at the same nest level with respect to the parent;

Fig. 7.2c). In addition, no grid can have more than a single parent (Fig. 7.2d). For global domains, a fine grid domain cannot cross the periodic lateral boundary of the parent domain.

For both 1-way and 2-way nested grid simulations, the ratio of the parent horizontal grid distance to the child horizontal grid distance (the spatial refinement ratio) must be an integer. For 2-way and concurrent 1-way nesting, this is also true for the time steps (the temporal refinement ratio). The model does allow the time step refinement ratio to differ from the spatial refinement ratio. Also, nested grids on the same level (i.e., children who have the same parent) may have different spatial and temporal refinement ratios. For example, in Fig. 7.2b, the horizontal grid resolution for domain 1 could be 90 km, for domain 2 could be 45 km, and for domain 3 could be 30 km.

Moving Nests

The moving nest capabilities in ARW are simply extensions to the suite of nesting options. All descriptions covering the specifics for the fine-grid domains (initialization, feedback, configurations, staggering, lateral boundaries, etc.) apply also to moving nests. In general, all nests in an ARW forecast are eligible to be moving nests. The ARW provides two methods to have nests move during the model integration: specified and automatic.

For a specified move, the timing of a nest move and the extent of the lateral move is defined entirely by the user. For the automatically moving nest, the fine grid is initialized to cover a well defined vortex, and the nest moves to maintain this vortex in the center of the fine grid. For both types of moving nests, multiple levels of domains may move. However, most of the instances where a moving nest is utilized are during tropical cyclone tracking via the vortex following technique.

After a nested domain has moved a parent grid-cell distance, the majority of the data in the domain is still valid. The data that is not along the outer row or column of the nested domain is shifted to the new location in that domain. Once a domain moves, the data in the outer row or column falls into two categories: discarded data on the trailing edge, and horizontally interpolated data on the leading edge in the direction of the nest move.

7.2 Staggering and Feedback

The ARW uses an Arakawa-C grid staggering. As shown in Fig. 7.3, the u and v components of horizontal velocity are normal to the respective faces of the grid cell, and the mass/thermodynamic/scalar/chemistry variables are located in the center of the cell.

The variable staggering has an additional column of u in the x-direction and an additional row of v in the y-direction because the normal velocity points define the grid boundaries. The horizontal momentum components reflect an average across each cell-face, while each mass/thermodynamic/scalar/chemistry variable is the representative mean value throughout the cell. Feedback is handled to preserve these mean values: the mass/thermodynamic/scalar/chemistry fields are fed back with an average from within the entire coarse grid point (Fig. 7.3), and the horizontal momentum variables are averaged along their respective normal coarse grid cell faces.

The horizontal interpolation (to instantiate a grid and to provide time-dependent lateral boundaries) does not conserve mass. The feedback mechanism, for most of the unmasked fields,
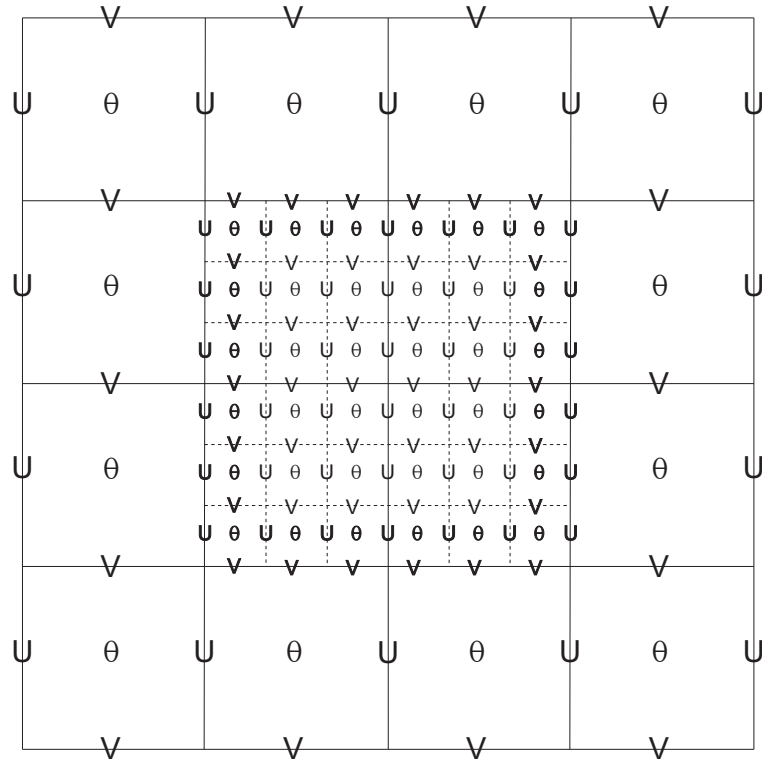
Figure 7.3: Arakawa-C grid staggering for a portion of a parent domain and an imbedded nest domain with a 3:1 grid size ratio. The solid lines denote coarse grid cell boundaries, and the dashed lines are the boundaries for each fine grid cell. The horizontal components of velocity ("U" and "V") are defined along the normal cell face, and the thermodynamic variables ("θ") are defined at the center of the grid cell (each square). The bold typeface variables along the interface between the coarse and the fine grid define the locations where the specified lateral boundaries for the nest are in effect.

uses cell averages (for mass/thermodynamic/scalar/chemistry quantities) and cell-face averages for the horizontal momentum fields.

The staggering defines the way that the fine grid is situated on top of the coarse grid. For all odd ratios there is a coincident point for each variable: a location that has the coarse grid and the fine grid at the same physical point. The location of this point depends on the variable. In each of the coarse-grid cells with an odd ratio, the middle fine-grid cell is the coincident point with the coarse grid for all of the mass-staggered fields (Fig. 7.3). For the horizontal momentum variables the normal velocity has coincident points along the grid boundaries for odd ratios.

For fields that are averaged back to the coarse grid in the feedback, the mean of the nine mass/thermodynamic/scalar/chemistry (for example, due to the 3:1 grid-distance ratio in the example shown in Fig. 7.3) fine grid points is fed back to the coarse grid. These fields include most 3-dimensional and 2-dimensional arrays. For the horizontal momentum fields averaged back to the coarse grid in the feedback, the mean of three (for example, due to the 3:1 grid-distance ratio in the example shown in Fig. 7.3) fine grid points is fed back to the coarse grid from along the coincident cell face. The fields that are masked due to the land/sea category are fed back directly from the coincident points for odd ratios. Masked fields include soil temperature and sea ice. It does not make sense to average neighboring locations of soil temperature on the fine grid if the coarse grid point being fedback to is a water value. Similarly, averaging several sea ice values on the fine grid does not make sense if some of the neighboring points included in the mean are fine grid land points. Only masked fields use the feedback method where a single point from the fine grid is assigned to the coarse grid.

A difference between the odd and even grid-distance ratios is in the feedback from the fine grid to the coarse grid. No coincident points exist for the single point feedback mechanisms for even grid distance ratios (such as used for the land/sea masked 2D fields). For a 2:1 even grid distance ratio, Figure 7.4 shows that each coarse grid point has four fine grid cells that are equally close, and therefore four equally eligible grid points for use as the single fine-grid point that feeds back to the coarse grid. The single-point feedback is arbitrarily chosen as the south-west corner of the four neighboring points. This arbitrary assignment to masked fields implies that even grid distance ratios are more suited for idealized simulations where masked fields are less important.

7.3   Nested Lateral Boundary Conditions

For the fine grid with 2-way nesting or 1-way nesting (using a concurrent ARW simulation, see Fig. 7.1), the boundary conditions are specified by the parent grid at every coarse-grid time step. The nest lateral boundary condition behaves similarly to the specified boundary condition for real-data cases (see Section 6.4), but the relaxation zone is not active. Prognostic variables are entirely specified in the outer row and column of the fine grid through spatial and temporal interpolation from the coarse grid (the coarse grid is stepped forward in time prior to advancement of any child grid of that parent).
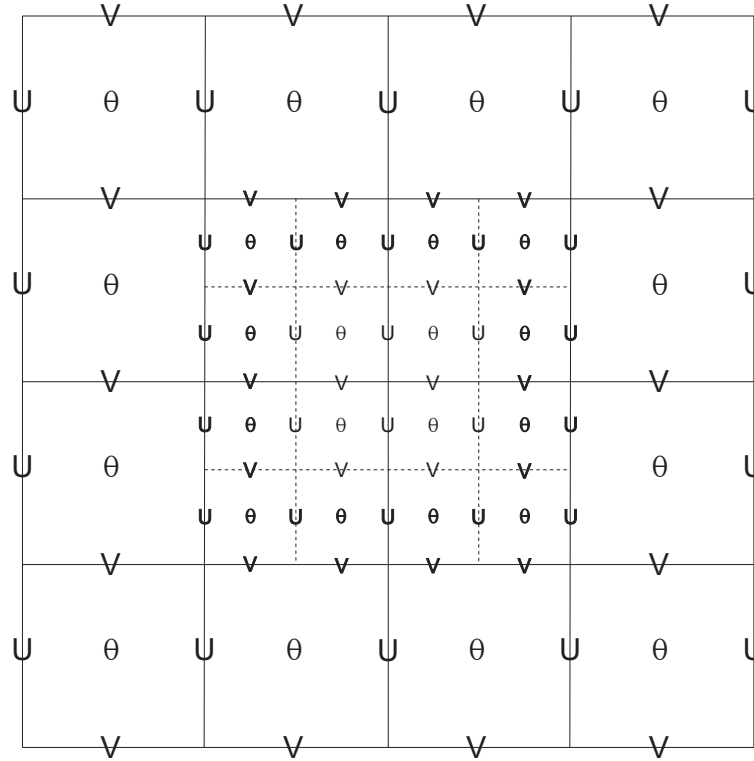
Figure 7.4: Similar to Fig. 7.3, but with a 2:1 grid-distance ratio.

7.4 Steps to Generate a Nest Grid

Only the concurrent 1-way nest option or the 2-way nest option are considered in this section. The 1-way nest option (using two consecutive ARW simulations, see Fig. 7.1) is functionally similar to two separate, single-grid simulations and does not fit the following description. For a multiple grid simulation within a single model run, there are some additional infrastructure steps that are required (briefly described in Fig. 7.5). While the following text details a simulation with a single coarse-grid and a single fine-grid, this implies no lack of generality when handling multiple grid levels or multiple grids on the same level.

Nest Instantiation

The fine grid is instantiated as a child of a parent grid at the requested start time. This initialization is within the integration step for the parent grid, so no child grid can begin if the parent is not active. To fill in the correct meteorological fields, an initialization routine is called to horizontally interpolate the coarse-grid data to the fine grid locations using a monotone interpolation scheme (described in Smolarkiewicz and Grell, 1992) for most fields (i.e., the same scheme employed for generating the fine grid lateral boundary conditions) and a simple linear interpolation or averaging scheme for masked or categorical fields. For fields that are masked with the land/sea background (such as land only fields (e.g., snow), or water only fields (e.g., sea ice)), the interpolator needs to know what field defines the template for the masking (such

```
Integrate Parent Grid One Time Step
        If Nest Grid Start Time
                (1) Horizontally Interpolate Parent to Child Grid
                (2) Optionally Input High-Resolution Child Data
                (3) Compute Child Reference State
                (4) Feedback Child Initial Data to Parent Grid
                (5) Re-Compute Parent Reference State
        End If Nest Grid Start Time

        Solve Time Step for Parent Grid (see Fig. 3.1)

        If Nest Grid Move Time
                (1) Move Nest Grid (Vortex Following or Prescribed)
                (2) Horizontally Interpolate Parent to Child Grid (Along New Boundary)
                (3) Optionally Input High-Resolution Child Topo Data
                (4) Compute Child Reference State
                (5) Feedback Child Initial Data to Parent Grid
                (6) Re-Compute Parent Reference State
        End If Nest Grid Move Time

        While Existing Nest Grids to Integrate
                (1) Lateral Forcing from Parent Grid to Child
                (2) Integrate Child Grid to Current Time of Parent Grid
                (3) Feedback Child Grid Information to Parent Grid
        End While Existing Nest Grids to Integrate
End Grid Integrate
```

Figure 7.5: Nest grid integration sequence.

as the land use category). Part of the automatic code generation handles calling each field with its associated interpolator.

Fine Grid Input

After the horizontal interpolation is completed, a few orographic-based variables are saved so that they may be used to blend the lateral boundaries along the coarse-grid/fine-grid interface. The terrain elevation, $\overline{\mu}_d$, and the reference geopotential $(\overline{\phi})$ are stored for later use. The fields selected as input from the fine grid input file (for the concurrent 1-way and 2-way forecast methods shown in Fig. 7.1) are ingested, and they overwrite the arrays that were horizontally interpolated from the coarse grid. No quality control for data consistency is performed for the fine grid input. All such masked checks are completed by the ARW real-data pre-processor *real*.
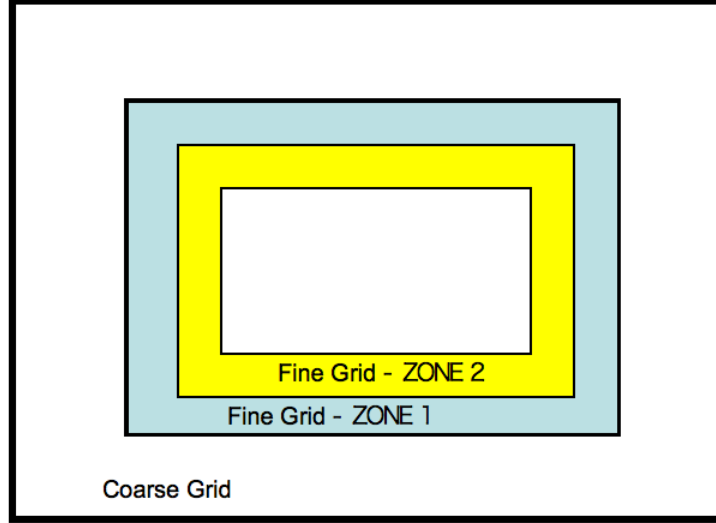
Figure 7.6: Zones of topographic blending for a fine grid. In the fine grid, the first zone is entirely interpolated from the coarse grid topography. In the second zone, the topography is linearly weighted between the coarse grid and the fine grid.

Interface Blended Orography

To reduce lateral boundary noise entering the fine grid, the fine grid topography has two zones of smoothing, as seen in Fig. 7.1. The first zone is along the outer edge of the fine domain and extends into the nest, with a width defined the same as the number of coarse grid points in the width of the lateral boundary file. In this first zone, the topography is horizontally interpolated from the coarse grid. The second zone extends inward from the first zone, with a user-defined width. The topography is linearly weighted between the interpolated coarse-grid topography and the fine-grid topography, and it ramps from 100% coarse-grid topography (at the interface between first and second zones) to 100% fine-grid topography interior to second zone. The weighting scheme in the second zone (assuming a width of 5 fine-grid cells) is given as:

- row/column 1: 100% interpolated coarse grid, 0% fine grid,
- row/column 2: 75% interpolated coarse grid, 25% fine grid,
- row/column 3: 50% interpolated coarse grid, 50% fine grid,
- row/column 4: 25% interpolated coarse grid, 75% fine grid, and
- row/column 5: 0% interpolated coarse grid, 100% fine grid,

where row=1 is the first row in the second zone, and where the row or column nearest the outer edge takes precedence in ambiguous corner zones. The reference variables computed from the topography, $\overline{\mu}_d$ and $\overline{\phi}$, are similarly treated. The blended arrays are required to compute the reference state for the fine grid. The blending along the inner rows and columns ramps the coarse grid reference state to the fine grid reference state for a smooth transition between the grids.

Feedback

So that the coarse grid and the fine grid are consistent at coincident points, the fine grid values are fed back to the coarse grid. There are two available options for feedback: either the mean of all fine grid cells contained within each coarse grid cell is fed back (or cell faces in the case of the horizontal momentum fields), or a single-point feedback is selected for the masked or categorical fields.

Subsequent to the feedback step, the coarse grid may be optionally smoothed in the area of the fine grid. Two smoothers are available: a 5-point 1-2-1 smoother and a smoother-desmoother with a similar stencil size. Both the feedback and the smoothers are run one row and column in from the interface row and column of the coarse grid that provides the lateral boundary conditions to the fine grid.

Reference State

The initial feedback when the nest is instantiated ensures that the coarse grid is consistent with the fine grid, particularly with regards to elevation and the reference state fields inside the blended region, and for such terrestrial features as coasts, lakes, and islands. The adjustment of the elevation in the coarse grid forces a base state recalculation. The fine-grid needs an initial base state calculation, and after the terrain feedback, the coarse grid is also in need of a base state recalculation.

Note that with the horizontal interpolation of the coarse grid to the fine grid and the feedback of the fine grid to the coarse grid, the coarse grid base state is recomputed even without a separate fine-grid initial data file, since the coarse grid topography is adjusted.

With the completed base state computations, which follow similarly to that described for the real-data initialization in section 5.2.2, the routines return back to the integration step for the coarse and fine grids. The fine grid data is now properly initialized for integration and can be advanced forward a time step.

Integration

The integration by grid is recursive. At the end of each grid's time step, a check is made to determine if a child grid exists for that parent and if the current time is bracketed by the child's start/end time. This is shown in Fig. 7.5. The integration process for the nest (step 2 under the while loop) is recursively calling the top step in the overall sequence as a coarse grid itself. This is a "depth first" traversal of the tree of grids. If a child grid does exist, that child grid is integrated up through the current time of the parent grid.

Chapter 8

Physics

This chapter outlines the physics options available in the ARW. The WRF physics options fall into several categories, each containing several choices. The physics categories are (1) microphysics, (2) cumulus parameterization, (3) planetary boundary layer (PBL), (4) land-surface model, and (5) radiation. Diffusion, which may also be considered part of the physics, is described in Chapter 4. The chapter will also address four-dimensional data assimilation (FDDA) methods that are available in ARW. These methods apply extra forcings to the model equations, and are internally treated similarly to physics.

The physics section is insulated from the rest of the dynamics solver by the use of physics drivers. These are between solver-dependent routines: a pre-physics preparation and post-physics modifications of the tendencies. The physics preparation involves filling arrays with physics-required variables that include the temperature, pressure, heights, layer thicknesses, and other state variables in MKS units at half-level grid points and on full levels. The velocities are also de-staggered so that the physics part is independent of the dynamical solver's velocity staggering. Physics packages compute tendencies for the velocity components (un-staggered), potential temperature, and moisture fields. The solver-dependent post-physics step will re-stagger these tendencies as necessary, couple tendencies with coordinate metrics, and convert to variables or units appropriate to the dynamics solver.

In the first Runge-Kutta step, prior to the acoustic steps (see Fig. 3.1, step(1)), tendencies are computed for radiation, surface, PBL, and cumulus physics. These tendencies are then held fixed through the Runge-Kutta steps. Microphysics is computed after the last Runge-Kutta step (see Fig. 3.1, step (9)) in order to maintain proper saturation conditions at the end of the time-step.

The initialization of the physics is called prior to the first model step. This initialization may include reading in data files for physics tables or calculating look-up tables of functions. Each physics module includes an initialization routine for this purpose. Often physics packages will have many of their own constants that should also be included in their own module, while common physical constants are passed in from the physics drivers.

8.1   Microphysics

Microphysics includes explicitly resolved water vapor, cloud, and precipitation processes. The model is general enough to accommodate any number of mass mixing-ratio variables, and other

Table 8.1: Microphysics Options

Scheme	Number of Variables	Ice-Phase Processes	Mixed-Phase Processes
Kessler	3	N	N
Purdue Lin	6	Y	Y
WSM3	3	Y	N
WSM5	5	Y	N
WSM6	6	Y	Y
Eta GCP	2	Y	Y
Thompson	7	Y	Y
Goddard	6	Y	Y
Morrison 2-Moment	10	Y	Y

quantities such as number concentrations. Four-dimensional arrays with three spatial indices and one species index are used to carry such scalars. Memory, i.e., the size of the fourth dimension in these arrays, is allocated depending on the needs of the scheme chosen, and advection of the species also applies to all those required by the microphysics option. In the current version of the ARW, microphysics is carried out at the end of the time-step as an adjustment process, and so does not provide tendencies. The rationale for this is that condensation adjustment should be at the end of the time-step to guarantee that the final saturation balance is accurate for the updated temperature and moisture. However, it is also important to have the latent heating forcing for potential temperature during the dynamical sub-steps, and this is done by saving the microphysical heating as an approximation for the next time-step as described in Section 3.1.4.

Currently, the sedimentation process is accounted for inside the individual microphysics modules, and, to prevent instability in the calculation of the vertical flux of precipitation, a smaller time step is allowed. The saturation adjustment is also included inside the microphysics. In the future, however, it might be separated into an individual subroutine to enable the remaining microphysics to be called less frequently than the model's advection step for efficiency.

Table 8.1 shows a summary of the options indicating the number of moisture variables, and whether ice-phase and mixed-phase processes are included. Mixed-phase processes are those that result from the interaction of ice and water particles, such as riming that produces graupel or hail. As a general rule, for grid sizes less than 10 km, where updrafts may be resolved, mixed-phase schemes should be used, particularly in convective or icing situations. For coarser grids the added expense of these schemes is not worth it because riming is not likely to be well resolved.

8.1.1 Kessler scheme

This scheme (Kessler, 1969), which was taken from the COMMAS model (Wicker and Wilhelmson, 1995), is a simple warm cloud scheme that includes water vapor, cloud water, and rain. The microphysical processes included are: the production, fall, and evaporation of rain; the accretion

and autoconversion of cloud water; and the production of cloud water from condensation.

8.1.2 Purdue Lin scheme

Six classes of hydrometeors are included: water vapor, cloud water, rain, cloud ice, snow, and graupel. All parameterization production terms are based on Lin et al. (1983) and Rutledge and Hobbs (1984) with some modifications, including saturation adjustment following Tao et al. (1989) and ice sedimentation. This is a relatively sophisticated microphysics scheme in WRF, and it is most suitable for use in research studies. The scheme is taken from the Purdue cloud model, and the details can be found in Chen and Sun (2002).

8.1.3 WRF Single-Moment 3-class (WSM3) scheme

The WRF single-moment microphysics scheme follows Hong et al. (2004) including ice sedimentation and other new ice-phase parameterizations. A major difference from other approaches is that a diagnostic relation is used for ice number concentration that is based on ice mass content rather than temperature. The computational procedures are described in Hong and Lim (2006). As with WSM5 and WSM6, the freezing/melting processes are computed during the fall-term sub-steps to increase accuracy in the vertical heating profile of these processes. The order of the processes is also optimized to decrease the sensitivity of the scheme to the time step of the model. The WSM3 scheme predicts three categories of hydrometers: vapor, cloud water/ice, and rain/snow, which is a so-called simple-ice scheme. It follows Dudhia (1989) in assuming cloud water and rain for temperatures above freezing, and cloud ice and snow for temperatures below freezing. This scheme is computationally efficient for the inclusion of ice processes, but lacks supercooled water and gradual melting rates.

8.1.4 WSM5 scheme

This scheme is similar to the WSM3 simple ice scheme. However, vapor, rain, snow, cloud ice, and cloud water are held in five different arrays. Thus, it allows supercooled water to exist, and a gradual melting of snow falling below the melting layer. Details can be found in Hong et al. (2004), and Hong and Lim (2006). As with WSM6, the saturation adjustment follows Dudhia (1989) and Hong et al. (1998) in separately treating ice and water saturation processes, rather than a combined saturation such as the Purdue Lin (above) and Goddard (Tao et al., 1989) schemes. This scheme is efficient in intermediate grids between the mesoscale and cloud-resolving grids.

8.1.5 WSM6 scheme

The six-class scheme extends the WSM5 scheme to include graupel and its associated processes. Some of the graupel-related terms follow Lin et al. (1983), but its ice-phase behavior is much different due to the changes of Hong et al. (2004). A new method for representing mixed-phase particle fall speeds for the snow and graupel particles by assigning a single fallspeed to both that is weighted by the mixing ratios, and applying that fallspeed to both sedimentation and accretion processes is introduced (Dudhia et al., 2008). The behavior of the WSM3, WSM5,

and WSM6 schemes differ little for coarser mesoscale grids, but they work much differently on cloud-resolving grids. Of the three WSM schemes, the WSM6 scheme is the most suitable for cloud-resolving grids, considering the efficiency and theoretical backgrounds (Hong and Lim, 2006).

8.1.6 Eta Grid-scale Cloud and Precipitation (2001) scheme

This is also known as EGCP01 or the Eta Ferrier scheme. The scheme predicts changes in water vapor and condensate in the forms of cloud water, rain, cloud ice, and precipitation ice (snow/graupel/sleet). The individual hydrometeor fields are combined into total condensate, and it is the water vapor and total condensate that are advected in the model. Local storage arrays retain first-guess information that extract contributions of cloud water, rain, cloud ice, and precipitation ice of variable density in the form of snow, graupel, or sleet. The density of precipitation ice is estimated from a local array that stores information on the total growth of ice by vapor deposition and accretion of liquid water. Sedimentation is treated by partitioning the time-averaged flux of precipitation saturation into a grid box between local storage in the box and fall out through the bottom of the box. This approach, together with modifications in the treatment of rapid microphysical processes, permits large time steps to be used with stable results. The mean size of precipitation ice is assumed to be a function of temperature following the observational results of Ryan (1996). Mixed-phase processes are now considered at temperatures warmer than -30°C (previously -10°C), whereas ice saturation is assumed for cloudy conditions at colder temperatures. Further description of the scheme can be found in Sec. 3.1 of the November 2001 Technical Procedures Bulletin (TPB) at http://www.emc.ncep.noaa.gov/mmb/mmbpll/eta12tpb/ and on the COMET page at http://meted.ucar.edu/nwp/pcu2/etapcp1.htm.

8.1.7 Thompson et al. scheme

A new bulk microphysical parameterization (BMP) has been developed for use with WRF or other mesoscale models. Compared to earlier single-moment BMPs, the new scheme incorporates a large number of improvements to both physical processes and computer coding plus employs many techniques found in far more sophisticated spectral/bin schemes using look-up tables. Unlike any other BMP, the assumed snow size distribution depends on both ice water content and temperature and is represented as a sum of exponential and gamma distributions. Furthermore, snow assumes a non-spherical shape with a bulk density that varies inversely with diameter as found in observations and in contrast to nearly all other BMPs that assume spherical snow with constant density.

New features specific to this version of the bulk scheme compared to the Thompson et al. (2004) paper description include:

- generalized gamma distribution shape for each hydrometeor species,
- non-spherical, variable density snow, and size distribution matching observations,
- y-intercept of rain depends on rain mixing ratio and whether apparent source is melted ice,
- y-intercept of graupel depends on graupel mixing ratio,
- a more accurate saturation adjustment scheme,

- variable gamma distribution shape parameter for cloud water droplets based on observations,
- look-up table for freezing of water drops,
- look-up table for transferring cloud ice into snow category,
- improved vapor deposition/sublimation and evaporation,
- variable collection efficiency for rain, snow, and graupel collecting cloud droplets,
- improved rain collecting snow and graupel.

8.1.8   Goddard Cumulus Ensemble Model scheme

The Goddard Cumulus Ensemble (GCE) models (Tao and Simpson, 1993) one-moment bulk microphysical schemes are mainly based on Lin et al. (1983) with additional processes from Rutledge and Hobbs (1984). However, the Goddard microphysics schemes have several modifications.

First, there is an option to choose either graupel or hail as the third class of ice (McCumber et al., 1991). Graupel has a relatively low density and a high intercept value (i.e., more numerous small particles). In contrast, hail has a relative high density and a low intercept value (i.e., more numerous large particles). These differences can affect not only the description of the hydrometeor population and formation of the anvil-stratiform region but also the relative importance of the microphysical-dynamical-radiative processes.

Second, new saturation techniques (Tao et al., 1989, 2003) were added. These saturation techniques are basically designed to ensure that super saturation (sub-saturation) cannot exist at a grid point that is clear (cloudy).

Third, all microphysical processes that do not involve melting, evaporation or sublimation (i.e., transfer rates from one type of hydrometeor to another) are calculated based on one thermodynamic state. This ensures that all of these processes are treated equally.

Fourth, the sum of all sink processes associated with one species will not exceed its mass. This ensures that the water budget will be balanced in the microphysical calculations .

The Goddard microphysics has a third option, which is equivalent to a two-ice (2ICE) scheme having only cloud ice and snow. This option may be needed for coarse resolution simulations (i.e., > 5 km grid size). The two-class ice scheme could be applied for winter and frontal convection.

8.1.9   Morrison et al. 2-Moment scheme

The Morrison et al. (2008) scheme is based on the two-moment bulk microphysics scheme of Morrison et al. (2005) and Morrison and Pinto (2006). Six species of water are included: vapor, cloud droplets, cloud ice, rain, snow, and graupel/hail. The code has a user-specified switch to include either graupel or hail. Prognostic variables include number concentrations and mixing ratios of cloud ice, rain, snow, and graupel/hail, and mixing ratios of cloud droplets and water vapor (total of 10 variables). The prediction of two-moments (i.e., both number concentration and mixing ratio) allows for a more robust treatment of the particle size distributions, which are a key for calculating the microphysical process rates and cloud/precipitation evolution. Several liquid, ice, and mixed-phase processes are included. Particle size distributions are treated using gamma functions, with the associated intercept and slope parameters derived from the predicted

Table 8.2: Cumulus Parameterization Options

Scheme	Cloud Detrainment	Type of scheme	Closure
Kain-Fritsch	Y	Mass flux	CAPE removal
Betts-Miller-Janjic	N	Adjustment	Sounding adjustment
Grell-Devenyi	Y	Mass flux	Various
Grell-3	Y	Mass flux	Various

mixing ratio and number concentration. The scheme has been extensively tested and compared with both idealized and real case studies covering a wide range of conditions.

8.2 Cumulus parameterization

These schemes are responsible for the sub-grid-scale effects of convective and/or shallow clouds. The schemes are intended to represent vertical fluxes due to unresolved updrafts and downdrafts and compensating motion outside the clouds. They operate only on individual columns where the scheme is triggered and provide vertical heating and moistening profiles. Some schemes additionally provide cloud and precipitation field tendencies in the column, and future schemes may provide momentum tendencies due to convective transport of momentum. The schemes all provide the convective component of surface rainfall.

Cumulus parameterizations are theoretically only valid for coarser grid sizes, (e.g., greater than 10 km), where they are necessary to properly release latent heat on a realistic time scale in the convective columns. While the assumptions about the convective eddies being entirely sub-grid-scale break down for finer grid sizes, sometimes these schemes have been found to be helpful in triggering convection in 5–10 km grid applications. Generally, they should not be used when the model can resolve the convective eddies itself (e.g., ≤ 5 km grid).

Table 8.2 summarizes the basic characteristics of the available cumulus parameterization options in the ARW.

8.2.1 Kain-Fritsch scheme

The modified version of the Kain-Fritsch scheme (Kain, 2004) is based on Kain and Fritsch (1990) and Kain and Fritsch (1993), but has been modified based on testing within the Eta model. As with the original KF scheme, it utilizes a simple cloud model with moist updrafts and downdrafts, including the effects of detrainment, entrainment, and relatively simple microphysics. It differs from the original KF scheme in the following ways:

- A minimum entrainment rate is imposed to suppress widespread convection in marginally unstable, relatively dry environments.

- Shallow (non precipitating) convection is allowed for any updraft that does not reach minimum cloud depth for precipitating clouds; this minimum depth varies as a function of cloud-base temperature.
- The entrainment rate is allowed to vary as a function of low-level convergence.
- Downdraft changes:
    - Source layer is the entire 150 – 200 mb deep layer just above cloud base.
    - Mass flux is specified as a fraction of updraft mass flux at cloud base. Fraction is a function of source layer RH rather than wind shear or other parameters, i.e., old precipitation efficiency relationship not used.
    - Detrainment is specified to occur in updraft source layer and below.

8.2.2 Betts-Miller-Janjic scheme

The Betts-Miller-Janjic (BMJ) scheme (Janjic, 1994, 2000) was derived from the Betts-Miller (BM) convective adjustment scheme (Betts, 1986; Betts and Miller, 1986). However, the BMJ scheme differs from the Betts-Miller scheme in several important aspects. The deep convection profiles and the relaxation time are variable and depend on the cloud efficiency, a non-dimensional parameter that characterizes the convective regime (Janjic, 1994). The cloud efficiency depends on the entropy change, precipitation, and mean temperature of the cloud. The shallow convection moisture profile is derived from the requirement that the entropy change be small and nonnegative (Janjic, 1994). The BMJ scheme has been optimized over years of operational application at NCEP, so that, in addition to the described conceptual differences, many details and/or parameter values differ from those recommended in Betts (1986) and Betts and Miller (1986). Recently, attempts have been made to refine the scheme for higher horizontal resolutions, primarily through modifications of the triggering mechanism. In particular:

- A floor value for the entropy change in the cloud is set up below which the deep convection is not triggered;
- In searching for the cloud top, the ascending particle mixes with the environment; and
- The work of the buoyancy force on the ascending particle is required to exceed a prescribed positive threshold.

8.2.3 Grell-Devenyi ensemble scheme

Grell and Devenyi (2002) introduced an ensemble cumulus scheme in which effectively multiple cumulus schemes and variants are run within each grid box and then the results are averaged to give the feedback to the model. In principle, the averaging can be weighted to optimize the scheme, but the default is an equal weight. The schemes are all mass-flux type schemes, but with differing updraft and downdraft entrainment and detrainment parameters, and precipitation efficiencies. These differences in static control are combined with differences in dynamic control, which is the method of determining cloud mass flux. The dynamic control closures are based on convective available potential energy (CAPE or cloud work function), low-level vertical velocity, or moisture convergence. Those based on CAPE either balance the rate of change of CAPE or relax the CAPE to a climatological value, or remove the CAPE in a convective time scale. The moisture convergence closure balances the cloud rainfall to the integrated vertical advection

of moisture. Another control is the trigger, where the maximum cap strength that permits convection can be varied. These controls typically provide ensembles of 144 members.

8.2.4 Grell-3 scheme

The Grell-3 scheme was first introduced in Version 3.0, and so is new, and not yet well tested in many situations. It shares a lot in common with the Grell-Devenyi in scheme, being based on an ensemble mean approach, but the quasi-equilibrium approach is no longer included among the ensemble members. The scheme is distinguished from other cumulus schemes by allowing subsidence effects to be spread to neighboring grid columns, making the method more suitable to grid sizes less than 10 km, while it can also be used at larger grid sizes where subsidence occurs within the same grid column as the updraft.

8.3 Surface Layer

The surface layer schemes calculate friction velocities and exchange coefficients that enable the calculation of surface heat and moisture fluxes by the land-surface models and surface stress in the planetary boundary layer scheme. Over water surfaces, the surface fluxes and surface diagnostic fields are computed in the surface layer scheme itself. The schemes provide no tendencies, only the stability-dependent information about the surface layer for the land-surface and PBL schemes. Currently, each surface layer option is tied to particular boundary-layer options, but in the future more interchangeability and options may become available. Note that some boundary layer schemes (YSU and MRF) require the thickness of the surface layer in the model to be representative of the actual surface layer (e.g. 50-100 meters).

8.3.1 Similarity theory (MM5)

This scheme uses stability functions from Paulson (1970), Dyer and Hicks (1970), and Webb (1970) to compute surface exchange coefficients for heat, moisture, and momentum. A convective velocity following Beljaars (1994) is used to enhance surface fluxes of heat and moisture. No thermal roughness length parameterization is included in the current version of this scheme. A Charnock relation relates roughness length to friction velocity over water. There are four stability regimes following Zhang and Anthes (1982). This surface layer scheme must be run in conjunction with the MRF or YSU PBL schemes. In Version 3, there is an option to replace the Charnock relation for roughness length with a Donelan relation that has lower drag at hurricane-force wind speeds, and may be more suitable for hurricane simulations. Also for water points, the Beljaars formulation for convective velocity is replaced by one proportional only to the vertical thermal gradient to help in weak-wind situations.

8.3.2 Similarity theory (Eta)

The Eta surface layer scheme (Janjic, 1996, 2002) is based on similarity theory (Monin and Obukhov, 1954). The scheme includes parameterizations of a viscous sub-layer. Over water surfaces, the viscous sub-layer is parameterized explicitly following Janjic (1994). Over land, the effects of the viscous sub-layer are taken into account through variable roughness height for

temperature and humidity as proposed by Zilitinkevich (1995). The Beljaars (1994) correction is applied in order to avoid singularities in the case of an unstable surface layer and vanishing wind speed. The surface fluxes are computed by an iterative method. This surface layer scheme must be run in conjunction with the Eta (Mellor-Yamada-Janjic) PBL scheme, and is therefore sometimes referred to as the MYJ surface scheme.

8.3.3   Similarity theory (PX)

The PX surface layer scheme (Pleim, 2006) was developed as part of the PX LSM but can be used with any LSM or PBL model. This scheme is based on similarity theory and includes parameterizations of a viscous sub-layer in the form of a quasi-laminar boundary layer resistance accounting for differences in the diffusivity of heat, water vapor, and trace chemical species. The surface layer similarity functions are estimated by analytical approximations from state variables.

8.4   Land-Surface Model

The land-surface models (LSMs) use atmospheric information from the surface layer scheme, radiative forcing from the radiation scheme, and precipitation forcing from the microphysics and convective schemes, together with internal information on the land's state variables and land-surface properties, to provide heat and moisture fluxes over land points and sea-ice points. These fluxes provide a lower boundary condition for the vertical transport done in the PBL schemes (or the vertical diffusion scheme in the case where a PBL scheme is not run, such as in large-eddy mode). [Note that large-eddy mode with interactive surface fluxes is not yet available in the ARW, but is planned for the near future.] The land-surface models have various degrees of sophistication in dealing with thermal and moisture fluxes in multiple layers of the soil and also may handle vegetation, root, and canopy effects and surface snow-cover prediction. The land-surface model provides no tendencies, but does update the land's state variables which include the ground (skin) temperature, soil temperature profile, soil moisture profile, snow cover, and possibly canopy properties. There is no horizontal interaction between neighboring points in the LSM, so it can be regarded as a one-dimensional column model for each WRF land grid-point, and many LSMs can be run in a stand-alone mode. Table 8.3 summarizes the basic features of the land-surface treatments in ARW.

8.4.1   5-layer thermal diffusion

This simple LSM is based on the MM5 5-layer soil temperature model. Layers are 1, 2, 4, 8, and 16 cm thick. Below these layers, the temperature is fixed at a deep-layer average. The energy budget includes radiation, sensible, and latent heat flux. It also allows for a snow-cover flag, but the snow cover is fixed in time. Soil moisture is also fixed with a landuse- and season-dependent constant value, and there are no explicit vegetation effects.

8.4.2   Noah LSM

The Noah LSM is the successor to the OSU LSM described by Chen and Dudhia (2001). The scheme was developed jointly by NCAR and NCEP, and is a unified code for research and

Table 8.3: Land Surface Options

Scheme	Vegetation Processes	Soil Variables (Layers)	Snow Scheme
5-layer	N	Temperature (5)	none
Noah	Y	Temperature, Water+Ice, Water (4)	1-layer, fractional
RUC	Y	Temperature, Ice, Water + Ice (6)	multi-layer
Pleim-Xiu	Y	Temperature, Moisture (2)	input only

operational purposes, being almost identical to the code used in the NCEP North American Mesoscale Model (NAM). This has the benefit of being consistent with the time-dependent soil fields provided in the analysis datasets. This is a 4-layer soil temperature and moisture model with canopy moisture and snow cover prediction. The layer thickness are 10, 30, 60 and 100 cm (adding to 2 meters) from the top down. It includes root zone, evapotranspiration, soil drainage, and runoff, taking into account vegetation categories, monthly vegetation fraction, and soil texture. The scheme provides sensible and latent heat fluxes to the boundary-layer scheme. The Noah LSM additionally predicts soil ice, and fractional snow cover effects, has an improved urban treatment, and considers surface emissivity properties, which are all new since the OSU scheme.

8.4.3 Rapid Update Cycle (RUC) Model LSM

The RUC LSM has a multi-level soil model (6 levels is default, could be 9 or more) with higher resolution in the top part of soil domain (0, 5, 20, 40, 160, 300 cm is default). The soil model solves heat diffusion and Richards moisture transfer equations, and in the cold season takes into account phase changes of soil water (Smirnova et al., 1997, 2000). The RUC LSM also has a multi-layer snow model with changing snow density, refreezing liquid water percolating through the snow pack, snow depth and temperature dependent albedo, melting algorithms applied at both snow-atmosphere interface and snow-soil interface, and simple parameterization of fractional snow cover with possibility of grid averaged skin temperature going above freezing. It also includes vegetation effects and canopy water. The RUC LSM has a layer approach to the solution of energy and moisture budgets. The layer spans the ground surface and includes half of the first atmospheric layer and half of the top soil layer with the corresponding properties (density, heat capacity, etc.) The residual of the incoming fluxes (net radiation, latent and sensible heat fluxes, soil heat flux, precipitation contribution into heat storage, etc.) modify the heat storage of this layer. An implicit technique is applied to the solution of these equations. Prognostic variables include soil temperature, volumetric liquid, frozen and total soil moisture contents, surface and sub-surface runoff, canopy moisture, evapotranspiration, latent, sensible and soil heat fluxes, heat of snow-water phase change, skin temperature, snow depth and density, and snow temperature.

8.4.4 Pleim-Xiu LSM

The PX LSM (Pleim and Xiu, 1995; Xiu and Pleim, 2001), originally based on the ISBA model Noilhan and Planton (1989), includes a 2-layer force-restore soil temperature and moisture model. The top layer is taken to be 1 cm thick, and the lower layer is 99 cm. The PX LSM features three pathways for moisture fluxes: evapotranspiration, soil evaporation, and evaporation from wet canopies. Evapotranspiration is controlled by bulk stomatal resistance that is dependent on root zone soil moisture, photosynthetically active radiation, air temperature, and the relative humidity at the leaf surface. Grid aggregate vegetation and soil parameters are derived from fractional coverages of land use categories and soil texture types. There are two indirect nudging schemes that correct biases in 2-m air temperature and RH by dynamic adjustment of soil moisture (Pleim and Xiu, 2003) and deep soil temperature (Pleim and Gilliam, 2008). Note that a small utility program (ipxwrf) can be used to propagate soil moisture and temperature between consecutive runs to create a continuous simulation of these quantities.

8.4.5 Urban Canopy Model

This can be run as an option with the Noah LSM. In order to represent the city scale effects on the mesoscale, an urban canopy model (UCM) originally developed by Kusaka et al. (2001) and Kusaka and Kimura (2004) and later on modified by Chen et al. (2006), is coupled to the WRF model via Noah Land surface model. In the UCM, all the urban effects in the vertical are assumed to be subgrid scale meaning that the urban processes are occurring below the lowest model level. The urban canopy model includes:

- (i) Parameterization of Street canyons to represent the urban geometry.
- (ii) Shadowing from building and radiation reflection.
- (iii) An exponential wind profile in the canopy layer
- (iv) multilayer heat equation from roof wall and road surfaces.

The urban canopy model estimates the surface temperature and heat fluxes from the roof, wall and road surface. It also calculates the momentum exchange between the urban surface and the atmosphere. If they are available, the UCM can take three dfferent densities of urban development using special land-use categories. In Version 3, an anthropogenic heating diurnal cycle was added as an option.

8.4.6 Ocean Mixed-Layer Model

This can be selected with the 5-layer option, and is designed for hurricane modeling in order to simulate the cooling of the ocean underneath hurricanes. The ocean mixed-layer model is based on that of Pollard et al. (1973). Each column is independently coupled to the local atmospheric column, so the model is one-dimensional. The ocean part consists of a time-varying layer, representing the variable-depth mixed layer over a fixed layer acting as a reservoir of cooler water with a specified thermal lapse rate. In the mixed layer, the prognostic variables are its depth, vector horizontal current, and mean temperature taken to be the sea-surface temperature (SST). The hurricane winds drive the current, which in turn leads to mixing at the base of the mixed layer when the Richardson number becomes low enough. This mixing deepens and cools

the mixed layer, and hence the cooler sea-surface temperature impacts the heat and moisture fluxes at the surface, and has a negative feedback on hurricane intensity. The model includes Coriolis effects on the current, which are important in determining the location of maximum cooling on the right side of the hurricane track. It also includes a mixed-layer heat budget, but the surface fluxes and radiation have much less impact than the hurricane-induced deep mixing on the thermal balance at the time scales considered during a forecast. The ocean mixed-layer model is initialized using the observed SST for the mixed layer, and with a single depth representative of known conditions in the hurricane's vicinity that may be replaced with a map of the mixed-layer depth, if available. The initial current is set to zero, which is a reasonable assumption given that the hurricane-induced current is larger than pre-existing ones.

8.4.7 Specified Lower Boundary Conditions

For long simulation periods, in excess of about a week, as in applications such as regional climate, ARW has a capability to specify lower boundary conditions on non-prognostic fields as a function of time. Foremost among these is the specification of the sea-surface temperature during the simulation. The Noah, RUC and PX LSMs also need to consider variations in vegetation fraction and albedo with season, so monthly datasets are interpolated to also be read in with the lower boundary file. Sea-ice cover variation can also be specified by this method in Version 3. The lower boundary conditions are simply read in typically at the same frequency as the lateral boundary conditions, and the fields are updated with new current values at each read.

8.5 Planetary Boundary Layer

The planetary boundary layer (PBL) is responsible for vertical sub-grid-scale fluxes due to eddy transports in the whole atmospheric column, not just the boundary layer. Thus, when a PBL scheme is activated, explicit vertical diffusion is de-activated with the assumption that the PBL scheme will handle this process. The most appropriate horizontal diffusion choices (Section 4.2.3) are those based on horizontal deformation or constant K_h values where horizontal and vertical mixing are treated independently. The surface fluxes are provided by the surface layer and land-surface schemes. The PBL schemes determine the flux profiles within the well-mixed boundary layer and the stable layer, and thus provide atmospheric tendencies of temperature, moisture (including clouds), and horizontal momentum in the entire atmospheric column. Most PBL schemes consider dry mixing, but can also include saturation effects in the vertical stability that determines the mixing. The schemes are one-dimensional, and assume that there is a clear scale separation between sub-grid eddies and resolved eddies. This assumption will become less clear at grid sizes below a few hundred meters, where boundary layer eddies may start to be resolved, and in these situations the scheme should be replaced by a fully three-dimensional local sub-grid turbulence scheme such as the TKE diffusion scheme (Section 4.2.4.) Table 8.4 summarizes the basic features of the PBL schemes in ARW.

8.5.1 Medium Range Forecast Model (MRF) PBL

The scheme is described by Hong and Pan (1996). This PBL scheme employs a so-called counter-gradient flux for heat and moisture in unstable conditions. It uses enhanced vertical

Table 8.4: Planetary Boundary Layer Options

Scheme	Unstable PBL Mixing	Entrainment treatment	PBL Top
MRF	K profile + countergradient term	part of PBL mixing	from critical bulk Ri
YSU	K profile + countergradient term	explicit term	from buoyancy profile
MYJ	K from prognostic TKE	part of PBL mixing	from TKE
ACM2	transilient mixing up, local K down	part of PBL mixing	from critical bulk Ri

flux coefficients in the PBL, and the PBL height is determined from a critical bulk Richardson number. It handles vertical diffusion with an implicit local scheme, and it is based on local Ri in the free atmosphere.

8.5.2 Yonsei University (YSU) PBL

The Yonsei University PBL (Hong et al., 2006) is the next generation of the MRF PBL, also using the countergradient terms to represent fluxes due to non-local gradients. This adds to the MRF PBL (Hong and Pan, 1996) an explicit treatment of the entrainment layer at the PBL top. The entrainment is made proportional to the surface buoyancy flux in line with results from studies with large-eddy models (Noh et al., 2003). The PBL top is defined using a critical bulk Richardson number of zero (compared to 0.5 in the MRF PBL), so is effectively dependent on the buoyancy profile, in which the PBL top is defined at the maximum entrainment layer (compared to the layer at which the diffusivity becomes zero). A smaller magnitude of the counter-gradient mixing in the YSU PBL produces a well-mixed boundary-layer profile, whereas there is a pronounced over-stable structure in the upper part of the mixed layer in the case of the MRF PBL. Details are available in Hong et al. (2006), including the analysis of the interaction between the boundary layer and precipitation physics. In version 3.0, an enhanced stable boundary-layer diffusion algorithm (Hong, 2007) is also devised that allows deeper mixing in windier conditions.

8.5.3 Mellor-Yamada-Janjic (MYJ) PBL

This parameterization of turbulence in the PBL and in the free atmosphere (Janjic, 1990, 1996, 2002) represents a nonsingular implementation of the Mellor-Yamada Level 2.5 turbulence closure model (Mellor and Yamada, 1982) through the full range of atmospheric turbulent regimes. In this implementation, an upper limit is imposed on the master length scale. This upper limit depends on the TKE as well as the buoyancy and shear of the driving flow. In the unstable range, the functional form of the upper limit is derived from the requirement that the TKE production be nonsingular in the case of growing turbulence. In the stable range, the upper limit is derived from the requirement that the ratio of the variance of the vertical velocity deviation and TKE cannot be smaller than that corresponding to the regime of vanishing turbulence. The

TKE production/dissipation differential equation is solved iteratively. The empirical constants have been revised as well (Janjic, 1996, 2002).

8.5.4 Asymmetrical Convective Model version 2 (ACM2) PBL

The ACM2 (Pleim, 2007) is a combination of the ACM, which is a simple transilient model that was originally a modification of the Blackadar convective model, and an eddy diffusion model. Thus, in convective conditions the ACM2 can simulate rapid upward transport in buoyant plumes and local shear induced turbulent diffusion. The partitioning between the local and non-local transport components is derived from the fraction of non-local heat flux according to the model of Holtslag and Boville (1993). The algorithm transitions smoothly from eddy diffusion in stable conditions to the combined local and non-local transport in unstable conditions. The ACM2 is particularly well suited for consistent PBL transport of any atmospheric quantity including both meteorological (u, v,θ , qv) and chemical trace species.

8.6 Atmospheric Radiation

The radiation schemes provide atmospheric heating due to radiative flux divergence and surface downward longwave and shortwave radiation for the ground heat budget. Longwave radiation includes infrared or thermal radiation absorbed and emitted by gases and surfaces. Upward longwave radiative flux from the ground is determined by the surface emissivity that in turn depends upon land-use type, as well as the ground (skin) temperature. Shortwave radiation includes visible and surrounding wavelengths that make up the solar spectrum. Hence, the only source is the Sun, but processes include absorption, reflection, and scattering in the atmosphere and at surfaces. For shortwave radiation, the upward flux is the reflection due to surface albedo. Within the atmosphere the radiation responds to model-predicted cloud and water vapor distributions, as well as specified carbon dioxide, ozone, and (optionally) trace gas concentrations. All the radiation schemes in WRF currently are column (one-dimensional) schemes, so each column is treated independently, and the fluxes correspond to those in infinite horizontally uniform planes, which is a good approximation if the vertical thickness of the model layers is much less than the horizontal grid length. This assumption would become less accurate at high horizontal resolution. Table 8.5 summarizes the basic features of the radiation schemes in the ARW.

8.6.1 Rapid Radiative Transfer Model (RRTM) Longwave

This RRTM, which is taken from MM5, is based on Mlawer et al. (1997) and is a spectral-band scheme using the correlated-k method. It uses pre-set tables to accurately represent longwave processes due to water vapor, ozone, CO_2, and trace gases (if present), as well as accounting for cloud optical depth.

Table 8.5: Radiation Options

Scheme	Longwave/ Shortwave	Spectral Bands	CO_2, O_3, clouds
RRTM	LW	16	CO_2, O_3, clouds
GFDL LW	LW	14	CO_2, O_3, clouds
CAM3 LW	LW	2	CO_2, O_3, clouds
GFDL SW	SW	12	CO_2, O_3, clouds
MM5 SW	SW	1	clouds
Goddard	SW	11	CO_2, O_3, clouds
CAM3 SW	SW	19	CO_2, O_3, clouds

8.6.2 Eta Geophysical Fluid Dynamics Laboratory (GFDL) Longwave

This longwave radiation scheme is from GFDL. It follows the simplified exchange method of Fels and Schwarzkopf (1975) and Schwarzkopf and Fels (1991), with calculation over spectral bands associated with carbon dioxide, water vapor, and ozone. Included are Schwarzkopf and Fels (1985) transmission coefficients for carbon dioxide, a Roberts et al. (1976) water vapor continuum, and the effects of water vapor-carbon dioxide overlap and of a Voigt line-shape correction. The Rodgers (1968) formulation is adopted for ozone absorption. Clouds are randomly overlapped. This scheme is implemented to conduct comparisons with the operational Eta model.

8.6.3 CAM Longwave

A spectral-band scheme used in the NCAR Community Atmosphere Model (CAM 3.0) for climate simulations. It has the potential to handle several trace gases. It interacts with resolved clouds and cloud fractions, and is documented fully by Collins et al. (2004).

8.6.4 Eta Geophysical Fluid Dynamics Laboratory (GFDL) Shortwave

This shortwave radiation is a GFDL version of the Lacis and Hansen (1974) parameterization. Effects of atmospheric water vapor, ozone (both from Lacis and Hansen, 1974), and carbon dioxide (Sasamori et al., 1972) are employed. Clouds are randomly overlapped. Shortwave calculations are made using a daylight-mean cosine solar zenith angle over the time interval (given by the radiation call frequency).

8.6.5 MM5 (Dudhia) Shortwave

This scheme is base on Dudhia (1989) and is taken from MM5. It has a simple downward integration of solar flux, accounting for clear-air scattering, water vapor absorption (Lacis and Hansen, 1974), and cloud albedo and absorption. It uses look-up tables for clouds from Stephens (1978). In Version 3, the scheme has an option to account for terrain slope and shadowing effects on the surface solar flux.

8.6.6 Goddard Shortwave

This scheme is based on Chou and Suarez (1994). It has a total of 11 spectral bands and considers diffuse and direct solar radiation components in a two-stream approach that accounts for scattered and reflected components. Ozone is considered with several climatological profiles available.

8.6.7 CAM Shortwave

A spectral-band scheme used in the NCAR Community Atmosphere Model (CAM 3.0) for climate simulations. It has the ability to handle optical properties of several aerosol types and trace gases. It uses cloud fractions and overlap assumptions in unsaturated regions, and has a monthly zonal ozone climatology. It is documented fully by Collins et al. (2004). The CAM radiation scheme is especially suited for regional climate simulations by having a ozone distribution that varies during the simulation according to monthly zonal-mean climatological data.

8.7 Physics Interactions

While the model physics parameterizations are categorized in a modular way, it should be noted that there are many interactions between them via the model state variables (potential temperature, moisture, wind, etc.) and their tendencies, and via the surface fluxes. Table 8.6 summarizes how the various physics processes interact in the model. In the table, i indicates that the state variable or flux is required input for the physics scheme, and o indicates that the tendency or flux is a probable output of the scheme. It can be seen that all the physical schemes interact in some way with the surface physics (land-surface models, and, potentially, coupled ocean models). The surface physics, while not explicitly producing tendencies of atmospheric state variables, is responsible for updating the land-state variables.

Note also that, as mentioned, the microphysics does not output tendencies, but updates the atmospheric state at the end of the model time-step. However, the rest of the o's in the upper half of the table are representative of the physical tendencies of these variables in the model.

The radiation, cumulus parameterization, and boundary-layer schemes all output tendencies, but the tendencies are not added until later in the solver, so from this perspective the order of call is not important. Moreover, these physics schemes do not have to be called at the same frequency as each other or the model time step. When lower frequencies are used, their tendencies are kept constant between calls. This is typically done for the radiation schemes, which are too expensive to call every time, and for the cumulus schemes, for which it is also not

Table 8.6: Physics Interactions. Columns correspond to model physical processes: radiation (Rad), microphysics (MP), cumulus parameterization (CP), planetary boundary layer/vertical diffusion (PBL), and surface physics (Sfc). Rows corresponds to model variables where i and o indicate whether a variable is input or output (updated) by a physical process.

		Rad	MP	CP	PBL	Sfc
Atmospheric State or Tendencies	Momentum			i	io	
	Pot. Temp.	io	io	io	io	
	Water Vapor	i	io	io	io	
	Cloud	i	io	o	io	
	Precip	i	io	o		
Surface Fluxes	Longwave Up	i				o
	Longwave Down	o				i
	Shortwave Up	i				o
	Shortwave Down	o				i
	Sfc Convective Rain			o		i
	Sfc Resolved Rain		o			i
	Heat Flux				i	o
	Moisture Flux				i	o
	Surface Stress				i	o

necessary. However, the surface/boundary-layer schemes are normally called every step in the ARW because this is likely to give the best results.

The radiation is called first because of the required radiative fluxes that are input to the land-surface scheme. The land-surface also requires rainfall from the microphysics and cumulus schemes, but that is from the previous time-step. The boundary-layer scheme is necessarily after the land-surface scheme because it requires the heat and moisture fluxes.

8.8   Four-Dimensional Data Assimilation

Four-dimensional data assimilation (FDDA), also known as nudging, is a method of keeping simulations close to analyses and/or observations over the course of an integration. There are two types of FDDA that can be used separately or in combination. Grid- or analysis-nudging simply forces the model simulation towards a series of analyses grid-point by grid-point. Observational- or station-nudging locally forces the simulation towards observational data. These methods provide a four-dimensional analysis that is somewhat balanced dynamically, and in terms of continuity, while allowing for complex local topographical or convective variations. Such datasets can cover long periods, and have particular value in driving off-line air quality or atmospheric chemistry models.

8.8.1   Grid Nudging or Analysis Nudging

Grid nudging is a major component of so-called Four-Dimensional Data Assimilation (FDDA). (Other components are surface-analysis nudging to be developed soon, and observational nudging, developed and released in WRF Version 2.2).

The grid-nudging method is specifically three-dimensional analysis nudging, whereby the atmospheric model is nudged towards time- and space-interpolated analyses using a point-by-point relaxation term. Stauffer and Seaman (1990) originally developed the technique for MM5.

The grid-nudging technique has several major uses.

a) Four-dimensional datasets. The model is run with grid-nudging for long periods, e.g. months, to provide a four-dimensional meteorologically self-consistent dataset that also stays on track with the driving analyses. In this way, the model is used as an intelligent interpolator of analyses between times, and also accounting better for topographic and convective effects. As mentioned, the primary use for such datasets is in air quality where the wind fields may be used to drive off-line chemistry models.

b) Boundary conditions. A nested simulation is run with the outer domain nudged towards analyses, and the nest running un-nudged. This provides better temporal detail at the nest boundary than driving it directly from linearly interpolated analyses, as it would be if it were the outer domain. This technique could also be used in forecasting, where an outer domain is nudged towards global forecast fields that are available in advance of the regional forecast.

c) Dynamic initialization. A pre-forecast period (e.g., -6 hours to 0 hours) is run with nudging using analyses at those times that are already available. This is probably better than a cold-start using just the 0 hour analysis because it gives the model a chance to spin up. In particular, the model will have six hours to adjust to topography, and produce cloud fields by hour 0, whereas with a cold start there would be a spin-up phase where waves are produced and

clouds are developed. This method could also be combined with 3D-Var techniques that may provide the hour 0 analysis.

Grid nudging has been added to ARW using the same input analyses as the WPS preprocessing systems can provide. Since it works on multiple domains in a nesting configuration, it requires multiple time-periods of each nudged domain as input analyses. Given these analyses, the *real* program produces another input file which is read by the model as nudging is performed. This file contains the gridded analysis 3d fields of the times bracketing the current model time as the forecast proceeds. The four nudged fields are the two horizontal wind components (u and v), temperature, and specific humidity.

The method is implemented through an extra tendency term in the nudged variable's equations, e.g.

$$\frac{\partial \theta}{\partial t} = F(\theta) + G_\theta W_\theta (\hat{\theta}_0 - \theta)$$

where $F(\theta)$ represents the normal tendency terms due to physics, advection, etc., G_θ is a timescale controlling the nudging strength, and W_θ is an additional weight in time or space to limit the nudging as described more below, while $\hat{\theta}_0$ is the time- and space-interpolated analysis field value towards which the nudging relaxes the solution.

Several options are available to control the nudging.

a) Nudging end-time and ramping. Nudging can be turned off during the simulation, as in dynamical initialization. Since turning nudging off suddenly can lead to noise, there is a capability for ramping the nudging down over a period, typically 1-2 hours to reduce the shock.

b) Strength of nudging. The timescale for nudging can be controlled individually for winds, temperature and moisture. Typically the namelist value of 0.0003 s-1 is used, corresponding to a timescale of about 1 hour, but this may be reduced for moisture where there may be less confidence in the analysis versus the details in the model.

c) Nudging in the boundary layer. Sometimes, since the analysis does not resolve the diurnal cycle, it is better not to nudge in the boundary layer to let the model PBL evolve properly, particularly the temperature and moisture fields. Each variable can therefore be selectively not nudged in the model boundary layer, the depth of which is given by the PBL physics.

d) Nudging at low levels. Alternatively the nudging can be deactivated for any of the variables below a certain layer throughout the simulation. For example, the lowest ten layers can be free of the nudging term.

e) Nudging and nesting. Each of these controls is independently set for each domain when nesting, except for the ramping function, which has one switch for all domains.

8.8.2 Observational or Station Nudging

The observation-nudging FDDA capability allows the model to effectively assimilate temperature, wind and moisture observations from all platforms, measured at any location within the model domains and any time within a given data assimilation periods With the observation-nudging formulation, each observation directly interacts with the model equations and thus the scheme yields dynamically and diabatically initialized analyses to support the applications that need regional 4-D full-field weather and/or to start regional NWP with spun-up initial conditions. The observation-nudging scheme, which is an enhanced version of the standard MM5

observation-nudging scheme, was implemented into WRF-ARW and has been in the model since WRF Version 2.2. More details of the methods can be found in Liu et al. (2008). The most significant modifications to the standard MM5 observation-nudging scheme (Stauffer and Seaman, 1994) that are included in the WRF observation-nudging scheme are summarized as follows:

(1) Added capability to incorporate all, conventional and non-conventional, synoptic and asynoptic data resources, including the twice daily radiosondes; hourly surface, ship and buoy observations, and special observations from GTS/WMO; NOAA/NESDIS satellite winds derived from cloud, water vapor and IR imageries; NOAA/FSL ACARS, AMDAR, TAMDAR and other aircraft reports; NOAA/FSL NPN (NOAA Profiler Network) and CAP (Corporative Agencies Profilers) profilers; the 3-hourly cloud-drifting winds and water-vapor-derived winds from NOAA/NESDIS; NASA Quikscat sea surface winds; and high-density, high-frequency observations from various mesonets of government agencies and private companies. In particular, special weights are assigned to the application-specific data, such as the SAMS network, special soundings and wind profilers located at and operated by the Army test ranges.

(2) Added capability to assimilate multi-level upper-air observations, such as radiosondes, wind profilers and radiometers, in a vertically coherent way, which is in contrast to the algorithm for single point observations such as aircraft reports and satellite derived winds.

(3) Surface temperature (at 2 m AGL) and winds (at 10 m AGL) observations are first adjusted to the first model level according to the similarity theory that is built in the model surface-layer physics and the surface-layer stability state at the observation time. The adjusted temperature and wind innovations at the lowest model level are then used to correct the model through the mixing layer, with weights gradually reduced toward the PBL top.

(4) Steep mountains and valleys severely limit the horizontal correlation distances. For example, weather variables on the upwind slope are not correlated with those on the downwind slope. To take account this effect, a terrain-dependent nudging weight correction is designed to eliminate the influence of an observation to a model grid point if the two sites are physically separated by a mountain ridge or a deep valley. More details about the scheme and numerical test results can be found in Xu et al. (2002). Essentially, for a given observation and grid point, a terrain search is done along the line connecting the grid point and the observation site. If there is a terrain blockage or a valley (deeper than a given depth), the nudging weight for the observation at the given grid point is set to zero. Currently, this algorithm is applied for surface observations assimilation only.

(5) The scheme was adjusted to accomplish data assimilation on multi-scale domains. Two adjustments among many are noteworthy. The first is an addition of grid-size-dependent horizontal nudging weight for each domain and the corresponding inflation with heights. The second is adding the capability of double-scans, a two-step observation-nudging relaxation. The idea is similar to the successive corrections: the first scan, with large influence radii and smaller weights, allows observations to correct large scale fields, while the second scan, with smaller influence radii and large weights, permits the observation to better define the smaller-scale feature.

(6) Observation-nudging allows the observation correction to be propagated into the model state in a given time influence window. One technical difficulty with this is that the model state is not known at the observation time for computing the observation increment, or innovation, during the first half of the time window. In the Stauffer and Seaman (1994) scheme, at each time step within the time influence window, the innovation is calculated (or approximated) by differing the observation from the model state at the time step. This obviously leads to dragging

the future forecasts toward previous (observation) states. To reduce this error, the innovation calculation is kept the same as before up to the observation time (this is OK since the model state is gradually tacking toward the observation state), but the true innovation s kept and used during the later half of the time influence window.

(7) An ability for users to set different nudging time-windows and influence radii for different (nested) domains has been added into WRF since the WRF V3.0 release.

Chapter 9

Variational Data Assimilation

An introduction to the basic ideas of variational data assimilation and the WRF-Var system is given in this chapter, followed by a brief overview of recent major improvements to WRF-Var. This overview supplements the original description of the three-dimensional variational (3D-Var) algorithm found in Barker et al. (2004). One of the most important additions to WRF-Var is a new utility *gen_be*, used to calculate background error covariances for a user's own application; it is discussed in the latter half of this chapter. The WRF-Var system is evolving rapidly, and a future technical note will accompany the general release of the 4D-Var component of WRF-Var. That technical note will include an extensive description of the entire WRF-Var system.

9.1   Introduction

The basic goal of any variational data assimilation system is to produce an optimal estimate of the true atmospheric state at analysis time through iterative solution of a prescribed cost-function (Ide et al., 1997):

$$J(\mathbf{x}) = J_b(\mathbf{x}) + J_o(\mathbf{x}) = \frac{1}{2}(\mathbf{x} - \mathbf{x}^b)^T \mathbf{B}^{-1}(\mathbf{x} - \mathbf{x}^b) + \frac{1}{2}(\mathbf{y} - \mathbf{y}^o)^T (\mathbf{E} + \mathbf{F})^{-1}(\mathbf{y} - \mathbf{y}^o). \qquad (9.1)$$

The variational problem can be summarized as the iterative minimization of (9.1) to find the analysis state $\mathbf{x}$ that minimizes $J(\mathbf{x})$. This solution represents the *a posteriori* maximum likelihood (minimum variance) estimate of the true state of the atmosphere given the two sources of *a priori* data: the first guess (or background) $\mathbf{x^b}$ and observations $\mathbf{y^o}$ (Lorenc, 1986). The fit to individual data points is weighted by estimates of their errors: $\mathbf{B}$, $\mathbf{E}$, and $\mathbf{F}$ are the background, observation (instrumental), and representivity error covariance matrices, respectively. Representivity error is an estimate of inaccuracies introduced in the observation operator H used to transform the gridded analysis $\mathbf{x}$ to observation space $\mathbf{y} = H(\mathbf{x})$ for comparison against observations. This error will be resolution dependent and may also include a contribution from approximations (e.g., linearizations) in H.

As described in Barker et al. (2004), the particular variational data assimilation algorithm adopted in WRF-Var is a model-space, incremental formulation of the variational problem. In this approach, observations, previous forecasts, their errors, and physical laws are combined to produce analysis increments $\mathbf{x^{a'}}$, which are added to the first guess $\mathbf{x^b}$ to provide an updated analysis.
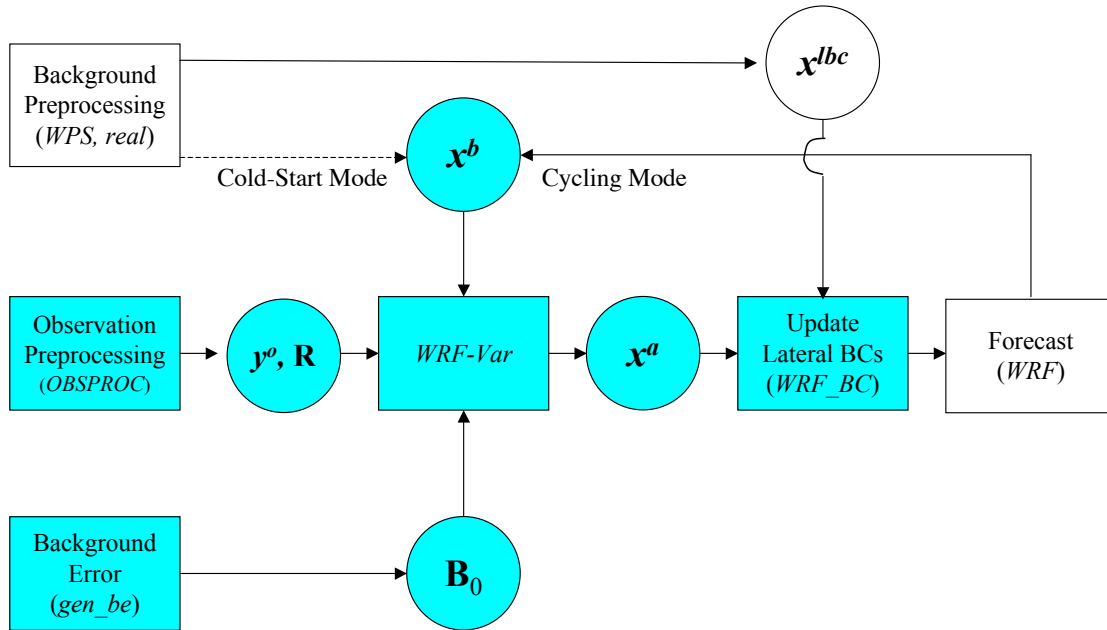
Figure 9.1: Sketch showing the relationship between datasets (circles), and algorithms (rectangles) of the ARW system.

Figure 9.1 illustrates the relationship between WRF-Var, the various datasets, and the other components of a typical NWP system (here ARW). The WRF-Var assimilation proceeds as described in Barker et al. (2004). A number of recent upgrades to the WRF-Var algorithm will be described in Section 9.2.

The three inputs to WRF-Var are:

a) First guess $\mathbf{x^b}$— In cold-start mode, this is typically a forecast/analysis from another model interpolated to the ARW grid (and variables) via the WRF SI and *real* programs. In cycling mode, the first guess is a short-range (typically 1–6 hour) ARW forecast.

b) Observations $\mathbf{y^o}$— In the current version of WRF-Var, observations may be supplied either in PREPBUFR format (*ob_format=1*) or an ASCII "little_r" format (*ob_format=2*). An observation preprocessor (3DVAR_OBSPROC) is supplied with the code release to perform basic quality control, assign "total" observation errors ($\mathbf{R} = \mathbf{E} + \mathbf{F}$ in Fig. 9.1), and reformat observations from the MM5 *little_r* text format into 3D-Var's own text format. Details can be found in Barker et al. (2003, 2004).

c) Background error covariances **B**— used to define the spatial and multivariate response of the analysis to an observation. In variational systems, these covariances are typically calculated off-line, and significant tuning is required to optimize performance for a particular application (e.g., Ingleby (2001); Wu et al. (2002)). The amount of work required to do this satisfactorily is significant, and should not be underestimated. In order to assist the user, WRF developers supply the following: i) a default set of statistics used for the initial set up of a domain; ii) a utility *gen_be* (described in Section 9.3) to process ensembles of forecasts into the appropriate control variable space; and iii) diagnostic routines to assess the accuracy of observation and background error statistics. These routines include both innovation vector-based approaches (Hollingsworth and Lonnberg, 1986) and variational tuning approaches (Desroziers and Ivanov, 2001).

Following assimilation of all data, an analysis $\mathbf{x^a}$ is produced that must be merged with the existing lateral boundary conditions $\mathbf{x^{lbc}}$ in the *WRF_BC* utility (Barker et al. (2003)). At this stage, the *wrfbdy* lateral boundary condition files ($\mathbf{x^{lbc}}$) output of WPS/real is updated to make the lateral boundaries consistent with the analysis, and surface fields (e.g. SST) are also updated in the *wrfinput* analysis file.

9.2   Improvements to the WRF-Var Algorithm

The latest version of WRF-Var (V3.0) contains a number of improvements relative to that described in the MM5 3DVAR technical note (Barker et al. (2003)). These are described below. It should also be noted that the public release of WRF-Var V3.0 contains only a subset of the capabilities of the full WRF-Var system. In particular, the direct assimilation of radiances, hybrid variational/ensemble data assimilation technique, and 4D-Var will be released once funding to support these complex algorithms is available.

9.2.1   Improved vertical interpolation

The original WRF 3D-Var system described in Barker et al. (2004) used height interpolation for all observation operators. If an observation is reported as a function of pressure, then height is approximated using the hydrostatic relation. This step introduces an unnecessary source of error. The new WRF-Var system performs vertical interpolation in terms of the original observed coordinate, i.e., pressure or height.

9.2.2   Improved minimization and "outer loop"

Prior to WRF-Var V3.0, the default WRF-Var cost function minimization used a modified version of the limited memory Quasi-Newton Method (QNM). In V3.0, an alternative Conjugate Gradient Method (CGM) has been implemented. Unlike the QNM technique, the CGM method restricts WRF-Var's inner loop to be completely linear. This limitation is dealt with through the inclusion of an outer loop in WRF-Var, the purpose of which is to iterate towards nonlinear solutions (e.g., observation operators, balance constraints, and the forecast itself in 4D-Var) using the WRF-Var analysis from the previous iteration as new first guess. The outer loop is also used as a form of variational quality control as follows: observations are rejected if the magnitude

of the observation minus first guess differences are larger than a specified threshold (typically several times the observation error standard deviation). This *errormax* test implicitly assumes the first guess is accurate. However, in cases when this assumption breaks down (i.e. in areas of large forecast error), there is a danger that good observations might be rejected in areas where they are most valuable. The outer loop alleviates this effect by allowing observations rejected in previous iterations to be accepted if their updated observation minus analysis differences pass the errormax QC check in in subsequent outer loops. The assimilation of nearby observations in previous iterations essentially provides a "buddy check" to the observation in question.

9.2.3 Choice of control variables

A major change that users of previous versions of WRF-Var will notice, is the simplification of the background error covariance model used within WRF-Var. As before, the background error covariance matrix $\mathbf{B}$ is computed not in model space $\mathbf{x}' : u, v, T, q, p_s$, but in a control variable space $\mathbf{v}$ related to model space via the control variable transform U, i.e.,

$$\mathbf{x}' = \mathrm{U}\mathbf{v} = \mathrm{U}_p\mathrm{U}_v\mathrm{U}_h\mathbf{v}. \tag{9.2}$$

The expansion $\mathrm{U} = \mathrm{U}_p\mathrm{U}_v\mathrm{U}_h$ represents the various stages of covariance modeling: horizontal correlations U_h, vertical covariances U_v, and multivariate covariances U_p.

The components of $\mathbf{v}$ are chosen so that their error cross-correlations are negligible, thus permitting the matrix $\mathbf{B}$ to be block-diagonalized. The major change in WRF-Var V3.0 is to simplify the control variable transform U_p to perform a simple statistical regression as described in subsection (9.3) below. Testing in numerous applications has shown a general improvement of forecasts scores using this definition of balance, as compared to the dynamical geostrophic//cyclostrophic balance constraint defined in Barker et al. (2003).

9.2.4 First Guess at Appropriate Time (FGAT)

A First Guess at Appropriate Time (FGAT) procedure has been implemented in WRF-Var (Lee et al., 2004). The FGAT capability results in a more accurate calculation of innovation vectors (observation minus first guess difference), and hence a better use of observations when their valid time differs from that of the analysis. FGAT is most effective for the analysis of observations from asynoptic, moving platforms (e.g., aircraft and satellite data).

9.2.5 Radar Data Assimilation

A capability to assimilate Doppler radar radial velocity and reflectivity observations is available in WRF-Var (Xiao et al., 2005, 2007a,b, 2008). In order to calculate the vertical velocity increment as a result of assimilating the vertical velocity component of radial velocity, the Richarson balance equation, which combines the continuity equation, adiabatic thermodynamic equation and hydrostatic relation, and its linear and adjoint codes are introduced. For reflectivity assimilation, total water is used as a control variable. This requires a partitioning between water vapor and hydrometeor increments during the minimization procedure. A warm-rain parameterization is included to assist the calculation of hydrometeors, which includes condensation of water vapor into cloud, accretion of cloud by rain, automatic conversion of cloud to rain, and

evaporation of rain to water vapor. The observation operators for Doppler radial velocity and reflectivity are included.

9.2.6 Unified Regional/Global 3D-Var Assimilation

There are many benefits to having a single data assimilation system for regional and global applications. The majority of the code is common to both (observation operators, minimization, background error preconditioning, interpolation, etc.). Technically, the main changes required to extend the regional application to global are related to the presence of a) the polar singularity, and b) periodic East-West boundary conditions. Of course, there are also scientific questions concerning the optimal mix of observations required for global/regional models, and the choice of control variables and balance constraints. A unified global/regional data assimilation system should therefore be flexible to a variety of thinning/quality-control algorithms and also to alternative formulations of the background error covariance matrix. This flexibility has been a key design requirement throughout the WRF-Var project.

The major difference between regional and global options in WRF-Var is in the definition of horizontal background error covariances. In regional mode, recursive filters (Purser et al., 2003) are used to project observation information away from the observation location. In global mode, a spectral decomposition is applied. The main benefits of the spectral technique are a) the isotropic and homogeneous covariances that are implied neatly solve the problems associated with the pole (the pole is not a special point in spectral space), and b) horizontal correlations are defined in terms of a single function— the power spectrum (a function of total wavenumber). However, the isotropy of correlation defined in spectral space is also a weakness— anisotropies need to be defined in an alternative manner. One solution to this problem is to replace the spectral correlations with grid-point correlations (Purser et al., 2003). An alternative technique is to supplement the isotropic spectral correlations with an anisotropic component derived via grid transformations, additional control variables or 4D-Var. Research using the latter techniques is underway using the WRF-Var system.

The WRF-Var code has been adapted to perform assimilation on a global, regular latitude-longitude grid. The major modifications are as follows.

a) Spectral to grid-point transformations (and their adjoints) have been included in 3D-Var to represent the horizontal component (U_h) of the background error covariance model.

b) A new global WRF-Var registry was created to accommodate the output of global forecast models (currently only the Korean Meteorological Administration's (KMA) global model has been tested). The final analysis increments are written in binary format and added back to the global first guess to provide the global analysis in the native model format.

c) Changes have been made to allow for periodic boundary conditions in the East–West direction.

d) A number of minor changes have been made to treat the polar rows as special points (e.g., in the grid-point ψ, χ to u, v wind conversion in the U_p transform and the observation operators for polar winds).

9.3 Background Error Covariances

Forecast ("first guess" or "background") error covariances are a vital input to variational data assimilation systems. They influence the analysis fit to observations and also completely define the analysis response away from observations. The latter impact is particularly important in data-sparse areas of the globe. Unlike ensemble filter data assimilation techniques (e.g., the Ensemble Adjustment Kalman Filter, the Ensemble Transform Kalman Filter), 3/4D-Var systems do not explicitly evolve forecast error covariances in real-time (although both 4D-Var and hybrid variational/ensemble data assimilation techniques currently being developed within WRF-Var implement flow-dependent covariances implicitly). Instead, climatologic statistics are usually estimated offline. The "NMC-method", in which forecast error covariances are approximated using forecast difference (e.g., T+48 minus T+24) statistics, is a commonly used approach (Parrish and Derber, 1992). Experiments at ECMWF (Fisher, 2003) indicate superior statistics may be obtained using a cycling analysis/forecast ensemble prediction system based on perturbed observations/physics.

Recent advances permit the use of flow-dependent forecast error covariances in 3D/4D-Var through, for example, grid transformations (Desroziers, 1997), anisotropic recursive filters (Wu et al., 2002; Purser et al., 2003), or observation-space formulations of the variational problem (Daley and Barker, 2001). Flow-dependence may be enhanced in 4D-Var through the use of the forecast model to provide dynamical consistency to the evolving forecast state during 4D-Var's time window (Rabier et al., 1998). Still, the practical effort required to specify and implement flow-dependent error covariances in 3/4D-Var is significant.

The development of a unified global/regional WRF-Var system, and its widespread use in the WRF community has necessitated the development of a new, efficient, portable forecast background error covariance calculation code. Numerous applications have also indicated that superior results are obtained if one invests effort in calculating domain-specific error covariances, instead of using the the default statistics supplied with the WRF-Var release. In this section, the new *gen_be* code developed by NCAR/MMM to generate forecast error statistics for use with the WRF-Var system is described.

The background error covariance matrix is defined as

$$\mathbf{B} = \overline{\epsilon\epsilon^T} \simeq \overline{\mathbf{x'}\mathbf{x'}^T}, \tag{9.3}$$

where the overbar denotes an average over time and/or geographical area. The true background error ϵ is not known in reality, but is assumed to be statistically well-represented by a model state perturbation $\mathbf{x'}$. In the standard NMC-method (Parrish and Derber, 1992), the perturbation $\mathbf{x'}$ is given by the difference between two forecasts (e.g., 24 hour minus 12 hour) verifying at the same time. Climatological estimates of background error may then be obtained by averaging such forecast differences over a period of time (e.g., one month). An alternative strategy proposed by (Fisher, 2003) makes use of ensemble forecast output, defining the $\mathbf{x'}$ vectors as ensemble perturbations (ensemble minus ensemble mean). In either approach, the end result is an ensemble of model perturbation vectors from which estimates of background error may be derived. The new *gen_be* utility has been designed to work with either forecast difference, or ensemble-based, perturbations. Using the NMC-method, $\mathbf{x'} = \mathbf{x_{T2}} - \mathbf{x_{T1}}$ where $T2$ and $T1$ are the forecast difference times (e.g., 48h minus 24h for global, 24h minus 12h for

BE Generation: Stage 0
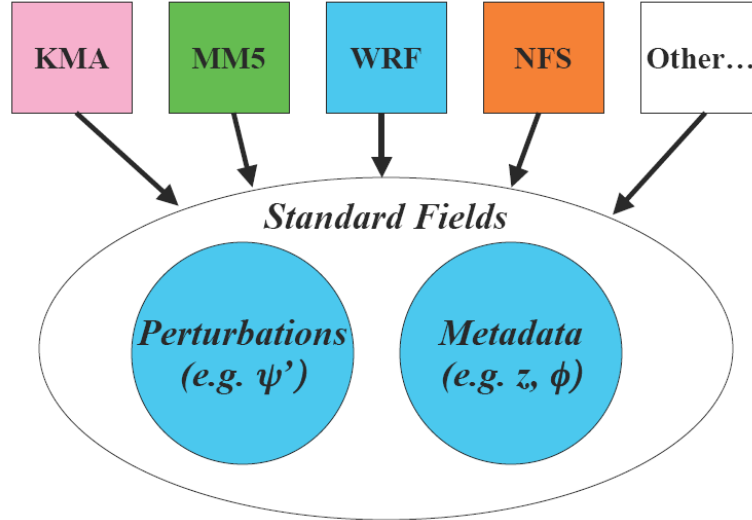
Figure 9.2: Sketch of the role of Stage 0 converters in transforming model-specific data (e.g., ARW, KMA global model, etc.) to standard perturbation fields and relevant metadata (e.g., latitude, height, land/sea, etc.).

regional). Alternatively, for an ensemble-based approach, $\mathbf{x_k}' = \mathbf{x_k} - \bar{\mathbf{x}}$, where the overbar is an average over ensemble members $k = 1, n_e$. The total number of binary files produced by this stage is $n_f \times n_e$ where n_f is the number of forecast times used (e.g., for 30 days with forecast every 12 hours, $n_f = 60$). Using the NMC-method, $n_e = 1$ (1 forecast difference per time). For ensemble-based statistics, n_e is the number of ensemble members.

As described above, the WRF-Var background error covariances are specified not in model space $\mathbf{x}'$, but in a control variable space $\mathbf{v}$, which is related to the model variables (e.g., wind components, temperature, humidity, and surface pressure) via the control variable transform defined in (9.2). Both (9.2) and its adjoint are required in WRF-Var. To enable this, the (offline) background error utility is used to compute components of the forecast error covariance matrix modeled within the U transform. This process is described in the following subsections.

The background error covariance generation code *gen_be* is designed to process data from a variety of regional/global models (e.g., ARW, MM5, KMA global model, NFS, etc.), and process it in order to provide error covariance statistics for use in variational data assimilation systems. The initial, model-dependent "stage 0" is illustrated in Fig. 9.2.

Alternative models use different grids, variables, data formats, etc., and so initial converters are required to transform model output into a set of standard perturbation fields (and metadata), and to output them in a standard binary format for further, model-independent processing. The standard grid-point fields are as follows.

- Perturbations: Streamfunction $\psi'(i, j, k)$, velocity potential $\chi'(i, j, k)$, temperature $T'(i, j, k)$, relative humidity $r'(i, j, k)$, surface pressure $p'_s(i, j)$.
- Full-fields: height $z(i, j, k)$, latitude $\phi(i, j)$. (These are required for the production of background error statistics stored in terms of physics variables, rather than tied to a

specific grid. This flexibility is included in *gen_be* through a namelist option to define the bins over which data is averaged in a variety of ways (e.g., latitude height, grid points). Land-sea and orographic effects may also be represented in this way.

In general, the *stage_0* converters are developed and maintained by those supporting individual models. Only the WRF-to-standard-fields converter *gen_be_stage0_wrf* is maintained and supported by the ARW effort.

9.3.1   Removal of time-mean

In order to calculate covariances between fields, the average value must first be removed. This is performed in the first stage utility *gen_be_stage1*.

9.3.2   Multivariate Covariances: Regression coefficients and unbalanced variables

The second stage of *gen_be (gen_be_stage2)* provides statistics for the unbalanced fields χ_u, T_u, and P_{su} used as control variables in WRF-Var. The unbalanced control variables are defined as the difference between full and balanced (or correlated) components of the field. In this stage of the calculation of background errors, the balanced component of particular fields is modeled via a regression analysis of the field using specified predictor fields (e.g., streamfunction; see Wu et al. (2002) for further details). The resulting regression coefficients are output for use in WRF-Var's U_p transform. Currently, three regression analyses are performed resulting in three sets of regression coefficients (note: The perturbation notation has been dropped for the remainder of this chapter for clarity.):

- Velocity potential/streamfunction regression: $\chi_b(k) = c(k)\psi(k)$;
- Temperature/streamfunction regression: $T_b(k) = \sum_{k1} G(k1, k)\psi(k1)$; and
- Surface pressure/streamfunction regression: $p_{sb} = \sum_{k1} W(k1)\psi(k1)$.

The summation over the vertical index $k1$ relates to the integral (hydrostatic) relationship between mass fields and the wind field. By default, the regression coefficients c, G, and W do not vary horizontally, however options exists to relax this assumption via the *bin_type* namelist variable in order to allow representation of differences between, for example, polar, mid-latitude, and tropical dynamical and physical processes. The scalar coefficient c used to estimate velocity potential errors from those of streamfunction is permitted to vary with model level in order to represent, for example, the impact of boundary-layer physics. Latitudinal/height smoothing of the resulting coefficients may be optionally performed to avoid artificial discontinuities at the edges of latitude/height boxes (see the future WRF-Var technical note for details of these "expert" features).

Having computed regression coefficients, the unbalanced components of the fields are calculated as $\chi_u(k) = \chi(k) - c(k)\psi(k)$, $T_u(k) = T(k) - \sum_{k1} G(k1, k)\psi(k1)$, and $p_{su} = p_s - \sum_{k1} W(k1)\psi(k1)$. These fields are output for the subsequent calculation of the spatial covariances as described below.

9.3.3 Vertical Covariances: Eigenvectors/eigenvalues and control variable projections

The third stage (*gen_be_stage3*) of *gen_be* calculates the statistics required for the vertical component of the control variable transform. This calculation involves the projection of 3D fields on model-levels onto empirical orthogonal functions (EOFs) of the vertical component of background error covariances Barker et al. (2004). For each 3D control variable (ψ, χ_u, T_u, and r), the vertical component of $\mathbf{B}$, is calculated and an eigenvector decomposition performed. The resulting eigenvectors $\mathbf{E}$ and eigenvalues Λ are saved for use in WRF-Var.

The *gen_be* code calculates both domain-averaged and local values of the vertical component of the background error covariance matrix. Eigendecomposition of the resulting $K \times K$ (K is the number of vertical levels) climatological vertical error covariance matrix $\mathbf{B} = \mathbf{E}\Lambda\mathbf{E}^T$ results in both domain-averaged and local eigenvectors $\mathbf{E}$ and eigenvalues Λ. Both sets of statistics are included in the dataset supplied to WRF-Var, allowing the choice between homogeneous (domain-averaged) or local (inhomogeneous) background error variances and vertical correlations to be chosen at run time Barker et al. (2004). Having calculated and stored eigenvectors and eigenvalues, the final part of *gen_be_stage3* is to project the entire sequence of 3D control variable fields into EOF space $\mathbf{v_v} = U_v^{-1}\mathbf{v_p} = \Lambda^{-1/2}\mathbf{E}^T\mathbf{v_p}$.

9.3.4 Horizontal Covariances: Recursive filter lengthscale (regional), or power spectra (global)

The last aspect of the climatological component of background error covariance data required for WRF-Var is the horizontal error correlations, the representation of which forms the largest difference between running WRF-Var in regional and global mode - the rest of *gen_be* is essentially the same for both regional and global models.

In a global application (*gen_be_stage4_global*), power spectra are computed for each of the K vertical modes of the 3D control variables ψ, χ_u, T_u, and relative humidity r, and for the 2D control variable p_{su} data. In contrast, in regional mode, horizontal correlations are computed between grid-points of each 2D field, binned as a function of distance. A Gaussian curve is then fitted to the data as described in Barker et al. (2004) to provide correlation lengthscales for use in the recursive filter algorithm.

9.4 WRF-Var V3.0 Software Engineering Improvements

A major overhall of the WRF-Var software has been performed for V3.0. The following is a summary:

9.4.1 Memory improvements

The WRF-Var registry had become bloated with WRF and U4D-Var 2d and 3d state variables that were unused in 3D-Var applications. These variables were allocated but uninitialised, and written to the analysis files. The removal of these dummy variable has resulted in a significant (10-50% depending on application) reduction in the memory requirements of WRF-Var.

9.4.2 Four-Byte I/O

The WRF-Var algorithm requires eight-byte precision internally. However, it only needs to read and write 4-byte files. Switching from 8-byte to 4-byte output in V3.0 has improved I/O performance and halves file sizes.

9.4.3 Switch from RSL to RSL_LITE

The switch from RSL to RSL_LITE has been made in V3.0 as the latter possesses a simpler "lighter" communications layer, and has been shown to be scalable to arbitrary domain sizes (largest to date: 4500x4500) and numbers of processors (largest to date: 64K processors on Blue Gene). RSL_LITE supports all capabilities of WRF, including Halo and periodic boundary exchanges, Distributed I/O, Nesting and moving nests, and parallel transposes. RSL_LITE has also been simplified by dropping irregular decomposition, load balancing, and ragged edge nesting, and the initialisation techniques improved to avoid recalculation and give better scaling at higher processor counts.

9.4.4 Reorganisation of observation structures

The F90 derived data types used for observations have been rewritten to permit batches of observations to be passed to subroutine calls, especially interpolation ones and subsequently makes better use of cache memory.

9.4.5 Radar reflectivity operators redesigned

The efficiency of the coding of the radar observation operators has been improved. Previously, routines were called once per observation, which would then recalculate common factors before performing what was often just a one-line calculation. Re-writing the code in V3.0 to move the calculations inside loops in the calling routine allows them to work on batches of observations at a time, vastly improving cache hit rates and eliminating recalculation.

Appendix A

Physical Constants

The following is a list of physical constants used in the model.

$$
\begin{aligned}
\pi &= 3.1415926 & & \text{Pi} \\
k &= 0.4 & & \text{Von Karman constant} \\
r_e &= 6.370 \times 10^6 \quad \text{m} & & \text{Radius of earth} \\
g &= 9.81 \quad \text{m s}^{-2} & & \text{Acceleration due to gravity} \\
\Omega_e &= 7.2921 \times 10^{-5} \quad \text{s}^{-1} & & \text{Angular rotation rate of the earth} \\
\sigma_B &= 5.67051 \times 10^{-8} \quad \text{W m}^{-2}\,\text{K}^{-4} & & \text{Stefan} - \text{Boltzmann constant} \\
R_d &= 287 \quad \text{J kg}^{-1}\,\text{K}^{-1} & & \text{Gas constant for dry air} \\
R_v &= 461.6 \quad \text{J kg}^{-1}\,\text{K}^{-1} & & \text{Gas constant for water vapor} \\
c_p &= 7 \times R_d/2 \quad \text{J kg}^{-1}\,\text{K}^{-1} & & \text{Specific heat of dry air at constant pressure} \\
c_v &= c_p - R_d \quad \text{J kg}^{-1}\,\text{K}^{-1} & & \text{Specific heat of dry air at constant volume} \\
c_{pv} &= 4 \times R_v \quad \text{J kg}^{-1}\,\text{K}^{-1} & & \text{Specific heat of water vapor at constant pressure} \\
c_{vv} &= c_{pv} - R_v \quad \text{J kg}^{-1}\,\text{K}^{-1} & & \text{Specific heat of water vapor at constant volume} \\
c_{liq} &= 4190 \quad \text{J kg}^{-1}\,\text{K}^{-1} & & \text{Specific heat capacity of water} \\
c_{ice} &= 2106 \quad \text{J kg}^{-1}\,\text{K}^{-1} & & \text{Specific heat capacity of ice} \\
L_v &= 2.5 \times 10^6 \quad \text{J kg}^{-1} & & \text{Latent heat of vaporization} \\
L_s &= 2.85 \times 10^6 \quad \text{J kg}^{-1} & & \text{Latent heat of sublimation} \\
L_f &= 3.50 \times 10^5 \quad \text{J kg}^{-1} & & \text{Latent heat of fusion} \\
\rho_w &= 1.0 \times 10^3 \quad \text{kg m}^{-3} & & \text{Density of liquid water}
\end{aligned}
$$

Appendix B

List of Symbols

Symbols used in this document are listed in alphabatical order in this appendix.

Symbols	Definition
a	generic variable
A	coefficient (Chapter 4), base-state lapse rate constant (Chapter 5)
$\mathbf{B}$	background error covariance matrix
c	scalar coefficient
c_s	speed of sound
C_k	a constant used in TKE closure
Cr	Courant number
Cr_{max}	maximum Courant number
Cr_{theory}	Courant number from Table 3.1
Cr_β	activation Courant number in vertical velocity damping
C_s	a constant used in eddy viscosity calculation
D	deformation
D_{nm}	deformation tensor, where $n, m = 1$, 2 and 3
e	cosine component of the Coriolis term (Chapters 2, 3); turbulent kinetic energy (Chapter 4)
$\mathbf{E}$	observation error covariance matrix
f	sine component of the Coriolis term
F	forcing terms for U, V, W, Θ and Q_m
$\mathbf{F}$	representivity error covariance matrix
$F_{X_{cor}}$	Coriolis forcing terms for $X = U$, V, and W
$F_{1,2}$	coefficients for weighting functions in specified boundary condition
g	acceleration due to gravity
G_k	regression coefficient
H	observation operator
J	cost function
$K_{dh,dv}$	horizontal and vertical eddy viscosity for gravity wave absorbing layer
$K_{h,v}$	horizontal and vertical eddy viscosities

Symbols   Definition

l_0	minimum length scale for dissipation
$l_{h,v}$	horizontal and vertical length scales for turbulence
l_{cr}	critical length scale for dissipation
L	latent heat of condensation
$L_{x,y}$	periodicity length in x and y
m	map scale factor
n_s	ratio of the RK3 time step to the acoustic time step
N	Brunt-Väisälä frequency
p	pressure
p'	perturbation pressure
p_0	reference sea-level pressure
p_h	hydrostatic pressure
$p_{ht,hs}$	hydrostatic pressure at the top and surface of the model
$p_{dht,dhs}$	dry hydrostatic pressure at the top and surface of the model
p_s	surface pressure
P_r	Prandtl number
q	generic scalar
$q_{c,i,r,s}$	mixing ratios for cloud water, ice, rain water and snow
q_m	generic mixing ratios for moisture
q_v	mixing ratio for water vapor
q_{vs}	saturation mixing ratio for water vapor
Q_m	generic coupled moisture variable
r	relative humidity
r_e	radius of earth
R	remaining terms in equations
R_d	gas constant for dry air
R_v	gas constant for water vapor
t	time
Δt	a full model time step
T	temperature
T_0	reference sea-level temperature
u	horizontal component of velocity in x-direction
U	coupled horizontal component of velocity in x-direction (Chapters 2, 3, 6, 7); control variable transform (Chapter 9)
U_h	horizontal correlation
U_p	multivariate covariance
U_v	vertical covariance
v	horizontal component of velocity in y-direction
$\mathbf{v}$	three dimensional vector velocity
V	coupled horizontal component of velocity in y-direction
$\mathbf{V}$	three dimensional coupled vector velocity
w	vertical component of velocity
W	coupled vertical component of velocity

Symbols	Definition
W_k	regression coefficient
z	height
z_d	depth of damping layer
z_{top}	height of model top
α	inverse density of air
α'	perturbation inverse density of air
$\bar{\alpha}$	inverse density of air for the reference state
α_d	inverse density of dry air
α_r	local rotation angle between y-axis and the meridian
β	off-centering coefficient for semi-implicit acoustic step
γ	ratio of heat capacities for dry air at constant pressure and volume
γ_d	divergence damping coefficient
γ_e	external mode damping coefficient
γ_g	damping coefficient for upper boundary gravity wave absorbing layer
γ_r	Rayleigh damping coefficient
ϵ	molecular weight of water over the molecular weight of dry air (Chapter 4); true background error (Chapter 9)
η	terrain-following hydrostatic-pressure vertical coordinate
$\dot{\eta}$	contravariant 'vertical' velocity or coordinate velocity
θ	potential temperature
θ_e	equivalent potential temperature
θ_m	moist potential temperature
Θ	coupled potential temperature
μ	hydrostatic pressure difference between surface and top of the model
$\bar{\mu}$	reference state hydrostatic pressure difference between surface and top of the model
μ_d	dry hydrostatic pressure difference between surface and top of the model
τ	acoustic time (Chapter 3), vertical structure function for Rayleigh damping (Chapter 4)
τ_{nm}	stress tensor (Chapter 4) where $n.m = 1$, 2 and 3
$\Delta\tau$	acoustic time step
ϕ	geopotential (Chapters 2, 3, 5); latitude (Chapter 9)
$\bar{\phi}$	geopotential for reference state
ϕ'	perturbation geopotential
Φ	generic prognostic variable (coupled)
ψ	generic variable (Chapter 6)
ψ'	streamfunction increment
χ'	velocity potential increment
ω	same as $\dot{\eta}$
Ω	coupled coordinate velocity
Ω_e	angular rotation rate of the earth

Subscripts/Superscripts	*Definition*
$()_d$	dry
$()_h$	hydrostatic
$()_0$	base state sea-level constant
$\overline{()}$	reference state
$()'$	perturbation from reference state
$()^{t*}$	full value at a Runge-Kutta step
$()''$	perturbation from Runge-Kutta step value in acoustic steps

Appendix C

Acronyms

AFWA	Air Force Weather Agency
API	Application Program Interface
ARPS	Advanced Regional Prediction System
ARW	Advanced Research WRF
BUFR	Binary Universal Form for the Representation of Meteorological Data
CAPE	Convectively Available Potential Energy
CAPS	Center for the Analysis and Prediction of Storms
CGM	Conjugate Gradient Method
COAMPS	Coupled Ocean / Atmosphere Mesoscale Prediction System
COMET	Cooperative Program for Operational Meteorology, Education, and Training
DFI	Digital Filtering Initialization
DTC	Developmental Testbed Center
ECMWF	The European Centre for Medium-Range Weather Forecasts
EOF	Empirical Orthogonal Function
ESMF	Earth System Modeling Framework
FAA	Federal Aviation Administration
FGAT	First Guess at Appropriate Time
FSL	Forecast System Laboratory
GFDL	Geophysical Fluid Dynamics Laboratory
GFS	Global Forecast System
GRIB	Gridded Binary
KMA	Korean Meteorological Administration
LSM	Land Surface Model
MKS	Meter Kilogram Second
MM5	Pennsylvania State / NCAR Mesoscale Model Version 5
MMM	Mesoscale and Microscale Meteorology Division
MRF	Medium Range Forecast Model
NAM	North American Mesoscale Model
NCAR	National Center for Atmospheric Research
NCEP	National Centers for Environmental Prediction
NFS	Non-hydrostatic Forecast System (Central Weather Bureau of Taiwan)
NMM	Nonhydrostatic Mesoscale Model
NOAA	National Oceanographic and Atmospheric Administration

NRL	Navy Research Laboratory
NWP	Numerical Weather Prediction
OSU	Oregon State University
PBL	Planetary Boundary Layer
PPM	Piecewise Parabolic Method
QNM	Quasi Newton Method
RHS	Right Hand Side
RRTM	Rapid Radiative Transfer Model
RUC	Rapid Update Cycle
SI	(WRF) Standard Initialization
TKE	Turbulent Kinetic Energy
UCAR	University Corporation for Atmospheric Research
YSU	Yonsei University (Korea)
VAR	Variational Assimilation
WRF	Weather Research and Forecasting Model
WSF	WRF Software Framework

Bibliography

Barker, D. M., W. Huang, Y.-R. Guo, and A. Bourgeois, 2003: A Three-Dimensional Variational (3DVAR) Data Assimilation System For Use With MM5. NCAR Tech Note, NCAR/TN-453+STR, 68 pp. [Available from UCAR Communications, P.O. Box 3000, Boulder, CO, 80307.].

Barker, D. M., W. Huang, Y.-R. Guo, A. Bourgeois, and X. N. Xiao, 2004: A Three-Dimensional Variational Data Assimilation System for MM5: Implementation and Initial Results *Mon. Wea. Rev.*, **132**, 897–914.

Beljaars, A.C.M., 1994: The parameterization of surface fluxes in large-scale models under free convection, *Quart. J. Roy. Meteor. Soc.*, **121**, 255–270.

Betts, A. K., 1986: A new convective adjustment scheme. Part I: Observational and theoretical basis. *Quart. J. Roy. Meteor. Soc.*, **112**, 677–691.

Betts, A. K., and M. J. Miller, 1986: A new convective adjustment scheme. Part II: Single column tests using GATE wave, BOMEX, and arctic air-mass data sets. *Quart. J. Roy. Meteor. Soc.*, **112**, 693–709.

Carpenter, R. L., K. K. Droegemeier, P. R. Woodward, and C. E. Hane, 1990: Application of the Piecewise Parabolic Method (PPM) to meteorological modeling. *Mon. Wea. Rev.*, **118**, 586–612.

Chen, F., and J. Dudhia, 2001: Coupling an advanced land-surface/ hydrology model with the Penn State/ NCAR MM5 modeling system. Part I: Model description and implementation. *Mon. Wea. Rev.*, **129**, 569–585.

Chen, F., M. Tewari, H. Kusaka, and T. T. Warner, 2006: Current status of urban modeling in the community Weather Research and Forecast (WRF) model. Joint with Sixth Symposium on the Urban Environment and AMS Forum: Managing our Physical and Natural Resources: Successes and Challenges, Atlanta, GA, USA, Amer. Meteor. Soc., CD-ROM. J1.4.

Chen, S.-H., and W.-Y. Sun, 2002: A one-dimensional time dependent cloud model. *J. Meteor. Soc. Japan*, **80**, 99–118.

Chou M.-D., and M. J. Suarez, 1994: An efficient thermal infrared radiation parameterization for use in general circulation models. NASA Tech. Memo. 104606, 3, 85pp.

Collins, W.D. et al., 2004: Description of the NCAR Community Atmosphere Model (CAM 3.0), NCAR Technical Note, NCAR/TN-464+STR, 226pp.

Cooper, W. A., 1986: Ice initiation in natural clouds. *Precipitation Enhancement — A Scientific Challenge*, Meteor. Monogr., No. 43, Amer. Met. Soc., 29–32.

Daley, R., and E. Barker, 2001: NAVDAS: Formulation and Diagnostics. *Mon. Wea. Rev.*, **129**, 869–883.

Davies, H. C., and R. E. Turner, 1977: Updating prediction models by dynamical relaxation: An examination of the technique. *Quart. J. Roy. Meteor. Soc.*, **103**, 225–245.

Deardorff, J. W., 1972 Numerical investigation of neutral and unstable planetary boundary layers, *J. Atmos. Sci.*, **29**, 91–115.

Desroziers, G., 1997: A coordinate change for data assimilation in spherical geometry of frontal structures. *Mon. Wea. Rev.*, **125**, 3030–3039.

Desroziers, G., and S. Ivanov, 2001: Diagnosis and adaptive tuning of observation-error parameters in a variational assimilation. *Quart. J. Roy. Meteor. Soc.*, **127**, 1433–1452.

Dudhia, J., 1989: Numerical study of convection observed during the winter monsoon experiment using a mesoscale two-dimensional model, *J. Atmos. Sci.*, **46**, 3077–3107.

Dudhia, J., 1995: Reply, *Mon. Wea. Rev.*, **123**, 2571–2575.

Dudhia, J., S.-Y. Hong, and K.-S. Lim, 2008: A new method for representing mixed-phase particle fall speeds in bulk microphysics parameterizations. *J. Met. Soc. Japan*, in press.

Durran, R. D., and J. B. Klemp, 1983: A compressible model for the simulation of moist mountain waves, *Mon. Wea. Rev.*, **111**, 2341–2361.

Dyer, A. J., and B. B. Hicks, 1970: Flux-gradient relationships in the constant flux layer, *Quart. J. Roy. Meteor. Soc.*, **96**, 715–721.

Easter, R. C., 1993: Two modified versions of Bott's positive definite numerical advection scheme. *Mon. Wea. Rev.,* **121,** 297–304.

Fels, S. B. and M. D. Schwarzkopf, 1975: The Simplified Exchange Approximation: A New Method for Radiative Transfer Calculations, *J. Atmos. Sci.*, **32**, 1475–1488.

Fisher, M., 2003: Background error covariance modeling. *Seminar on Recent Development in Data Assimilation for Atmosphere and Ocean*, 45–63, ECMWF.

Fletcher, N. H., 1962: *The Physics Of Rain Clouds.* Cambridge University Press, 386 pp.

Grell, G. A., and D. Devenyi, 2002: A generalized approach to parameterizing convection combining ensemble and data assimilation techniques. *Geophys. Res. Lett.*, **29(14)**, Article 1693.

Grell, G.A., S.E. Peckham, R. Schmitz, S.A. McKeen, G. Frost, W.C. Skamarock and B. Eder, 2005: Fully coupled online chemistry within the WRF model. *Atmos. Environ.*, **39**, 6957-6975.

Haltiner, G. J., and R. T. Williams, 1980: *Numerical prediction and dynamic meteorology.* John Wiley & Sons, Inc., 477pp.

Hollingsworth, A., and P. Lonnberg, 1986: The Statistical Structure Of Short-Range Forecast Errors As Determined From Radiosonde Data. Part I: The Wind Field. *Tellus*, **38A**, 111–136.

Holtslag, A. A. M. and B. A. Boville, 1993: Local versus non-local boundary layer diffusion in a global climate model, *J. Climate*, **6**, 1825–1842.

Hong, S.-Y., 2007: Stable Boundary Layer Mixing in a Vertical Diffusion Scheme. The Korea Meteor. Soc., Fall conference, Seoul, Korea, Oct. 25-26.

Hong, S.-Y., and J.-O. J. Lim, 2006: The WRF Single-Moment 6-Class Microphysics Scheme (WSM6), *J. Korean Meteor. Soc.*, **42**, 129–151.

Hong, S.-Y., and H.-L. Pan, 1996: Nonlocal boundary layer vertical diffusion in a medium-range forecast model, *Mon. Wea. Rev.*, **124**, 2322–2339.

Hong, S.-Y., H.-M. H. Juang, and Q. Zhao, 1998: Implementation of prognostic cloud scheme for a regional spectral model, *Mon. Wea. Rev.*, **126**, 2621–2639.

Hong, S.-Y., J. Dudhia, and S.-H. Chen, 2004: A Revised Approach to Ice Microphysical Processes for the Bulk Parameterization of Clouds and Precipitation, *Mon. Wea. Rev.*, **132**, 103–120.

Hong, S.-Y., and Y. Noh, and J. Dudhia, 2006: A new vertical diffusion package with an explicit treatment of entrainment processes. *Mon. Wea. Rev.*, **134**, 2318–2341.

Huang, X.-Y. and P. Lynch, 1993: Diabatic Digital-Filtering Initialization: Application to the HIRLAM Model., *Mon. Wea. Rev.*, **121**, 589–603.

Ide, K., P. Courtier, M. Ghil, and A. C. Lorenc, 1997: Unified notation for data assimilation: Operational, sequential and variational. *J. Met. Soc. Japan*, **75**, 181–189.

Ingleby, N. B., 2001: The statistical structure of forecast errors and its representation in the Met. Office global 3-D variational data assimilation scheme. *Quart. J. Roy. Meteor. Soc.*, **127**, 209–232.

Janjic, Z. I., 1990: The step-mountain coordinate: physical package, *Mon. Wea. Rev.*, **118**, 1429–1443.

Janjic, Z. I., 1994: The step-mountain eta coordinate model: further developments of the convection, viscous sublayer and turbulence closure schemes, *Mon. Wea. Rev.*, **122**, 927–945.

Janjic, Z. I., 1996: The surface layer in the NCEP Eta Model, *Eleventh Conference on Numerical Weather Prediction*, Norfolk, VA, 19–23 August; Amer. Meteor. Soc., Boston, MA, 354–355.

Janjic, Z. I., 2000: Comments on "Development and Evaluation of a Convection Scheme for Use in Climate Models", *J. Atmos. Sci.*, **57**, p. 3686.

Janjic, Z. I., 2002: Nonsingular Implementation of the Mellor–Yamada Level 2.5 Scheme in the NCEP Meso model, *NCEP Office Note*, **No. 437**, 61 pp.

Kain, J. S., and J. M. Fritsch, 1990: A one-dimensional entraining/ detraining plume model and its application in convective parameterization, *J. Atmos. Sci.*, **47**, 2784–2802.

Kain, J. S., and J. M. Fritsch, 1993: Convective parameterization for mesoscale models: The Kain-Fritcsh scheme, *The representation of cumulus convection in numerical models*, K. A. Emanuel and D.J. Raymond, Eds., Amer. Meteor. Soc., 246 pp.

Kain, J. S., 2004: The Kain-Fritsch convective parameterization: An update. *J. Appl. Meteor.*, **43**, 170–181.

Kessler, E., 1969: On the distribution and continuity of water substance in atmospheric circulation, *Meteor. Monogr.*, **32**, Amer. Meteor. Soc., 84 pp.

Klemp, J. B., and D. K. Lilly, 1978: Numerical simulation of hydrostatic mountain waves, *J. Atmos. Sci.*, **35**, 78–107.

Klemp, J. B., and R. Wilhelmson, 1978: The simulation of three-dimensional convective storm dynamics, *J. Atmos. Sci.*, **35**, 1070–1096.

Klemp, J. B., W. C. Skamarock, and J. Dudhia, 2007: Conservative split-explicit time integration methods for the compressible nonhydrostatic equations, *Mon. Wea. Rev.*., **135,** 2897–2913.

Klemp, J. B., J. Dudhia, and A. Hassiotis, 2008: An Upper Gravity Wave Absorbing Layer for NWP Applications. *Mon. Wea. Rev.*., submitted.

Knievel, J. C., G. H. Bryan, and J. P. Hacker, 2007: Explicit numerical diffusion in the WRF Model. *Mon. Wea. Rev.*, **135**, 3808–3824.

Kusaka, H. and F. Kimura, 2004: Coupling a single-layer urban canopy model with a simple atmospheric model: Impact on urban heat island simulation for an idealized case. *J. Meteor. Soc. Japan*, **82**, 67–80.

Kusaka, H., H. Kondo, Y. Kikegawa, and F. Kimura, 2001: A simple single-layer urban canopy model for atmospheric models: Comparison with multi-layer and slab models. *Bound.-Layer Meteor.*, **101**, 329–358.

Lacis, A. A., and J. E. Hansen, 1974: A parameterization for the absorption of solar radiation in the earth's atmosphere. *J. Atmos. Sci.*, **31**, 118–133.

Laprise R., 1992: The Euler Equations of motion with hydrostatic pressure as as independent variable, *Mon. Wea. Rev.*, **120**, 197–207.

Lee, M.-S., D. Barker, W. Huang and Y.-H. Kuo, 2004: First Guess at Appropriate Time (FGAT) with WRF 3DVAR. *WRF/MM5 Users Workshop*, 22–25 June 2004, Boulder, Colorado.

Lin, Y.-L., R. D. Farley, and H. D. Orville, 1983: Bulk parameterization of the snow field in a cloud model. *J. Climate Appl. Meteor.*, **22**, 1065–1092.

Lin, S.-J., and R. B. Rood, 1996: Multidimensional flux-form semi-Lagrangian transport schemes. *Mon. Wea. Rev.*, **124**, 2046–2070.

Liu, Y., T.T. Warner, J. F. Bowers, L. P. Carson, F. Chen, C. A. Clough, C. A. Davis, C. H. Egeland, S. Halvorson, T.W. Huck Jr., L. Lachapelle, R.E. Malone, D. L. Rife, R.-S. Sheu, S. P. Swerdlin, and D.S. Weingarten, 2008: The operational mesogamma-scale analysis and forecast system of the U.S. Army Test and Evaluation Command. Part 1: Overview of the modeling system, the forecast products. *J. Appl. Meteor. Clim.*, **47**, 1077–1092.

Lorenc, A. C., 1986: Analysis methods for numerical weather prediction. *Quart. J. Roy. Meteor. Soc.*, **112**, 1177–1194.

Lynch, P., and X.-Y. Huang, 1992: Initialization of the HIRLAM Model Using a Digital Filter. *Mon. Wea. Rev.*, **120**, 1019–1034.

Lynch, P., and X.-Y. Huang, 1994: Diabatic initialization using recursive filters. *Tellus*, **46A**, 583–597.

Lynch, P., 1997: The Dolph-Chebyshev Window: A Simple Optimal Filter. *Mon. Wea. Rev.*, **125**, 655–660.

McCumber, M., W.-K. Tao, J. Simpson, R. Penc, and S.-T. Soong, 1991: Comparison of ice-phase microphysical parameterization schemes using numerical simulations of tropical convection, *J. Appl. Meteor.*, **30**, 985–1004.

Mellor, G. L., and T. Yamada, 1982: Development of a turbulence closure model for geophysical fluid problems. *Rev. Geophys. Space Phys.*, **20**, 851–875.

Michalakes, J., J. Dudhia, D. Gill, J. Klemp, and W. Skamarock, 1999: Design of a next-generation regional weather research and forecast model, *Towards Teracomputing*, World Scientific, River Edge, New Jersey, 117–124.

Michalakes, J., J. Dudhia, D. Gill, T. Henderson, J. Klemp, W. Skamarock, and W. Wang, 2004: The Weather Research and Forecast Model: Software Architecture and Performance. To appear in proceeding of *the Eleventh ECMWF Workshop on the Use of High Performance Computing in Meteorology*. 25–29 October 2004, Reading, U.K., Ed. George Mozdzynski.

Mlawer, E. J., S. J. Taubman, P. D. Brown, M. J. Iacono, and S. A. Clough, 1997: Radiative transfer for inhomogeneous atmosphere: RRTM, a validated correlated-k model for the longwave. *J. Geophys. Res.*, **102** (D14), 16663–16682.

Monin, A.S. and A.M. Obukhov, 1954: Basic laws of turbulent mixing in the surface layer of the atmosphere. *Contrib. Geophys. Inst. Acad. Sci.*, USSR, **(151)**, 163–187 (in Russian).

Morrison, H., J. A. Curry, and V. I. Khvorostyanov, 2005: A new double-moment microphysics parameterization for application in cloud and climate models, Part I: Description. *J. Atmos. Sci.*, **62**, 1665–1677.

Morrison, H., and J. O. Pinto, 2006: Intercomparison of bulk microphysics schemes in mesoscale simulations of springtime Arctic mixed-phase stratiform clouds. *Mon. Wea. Rev.*, **134**, 1880–1900.

Morrison, H., G. Thompson, and V. Tatarskii, 2008: Impact of cloud micrpohysics on the development of trailing stratiform precipitation in a simulated squall line: Comparison of one- and two-moment schemes. Submitted to *Mon. Wea. Rev.*

Noh, Y., W.G. Cheon, S.-Y. Hong, and S. Raasch, 2003: Improvement of the K-profile model for the planetary boundary layer based on large eddy simulation data. *Bound.-Layer Meteor.*, **107**, 401–427.

Noilhan, J., and S. Planton, 1989: A simple parameterization of land surface processes for meteorological models. *Mon. Wea. Rev.*, **117**, 536–549.

Ooyama K. V., 1990: A thermodynamic foundation for modeling the moist atmosphere, *J. Atmos. Sci.*, **47**, 2580–2593.

Parrish, D. F., and J. C. Derber, 1992: The National Meteorological Center's Spectral Statistical Interpolation analysis system. *Mon. Wea. Rev.*, **120**, 1747–1763.

Paulson, C. A., 1970: The mathematical representation of wind speed and temperature profiles in the unstable atmospheric surface layer. *J. Appl. Meteor.*, **9**, 857–861.

Pleim, J. E., 2006: A simple, efficient solution of flux-profile relationships in the atmospheric surface layer, *J. Appl. Meteor. and Clim.*, **45**, 341–347

Pleim, J. E., 2007: A combined local and non-local closure model for the atmospheric boundary layer. Part 1: Model description and testing, *J. Appl. Meteor. and Clim.*, **46**, 1383–1395.

Pleim, J.E. and R.C. Gilliam, 2008: An indirect data assimilation scheme for deep soil temperature in the Pleim-Xiu land surface model. Submitted to *J. Appl. Meteor. Climatol.*

Pleim, J. E. and A. Xiu, 1995: Development and testing of a surface flux and planetary boundary layer model for application in mesoscale models. *J. Appl. Meteor.*, **34**, 16–32.

Pleim, J. E., and A. Xiu, 2003: Development of a land surface model. Part II: Data Assimilation. *J. Appl. Meteor.*, **42**, 1811–1822.

Pollard, R. T., P. B. Rhines and R. O. R. Y. Thompson, 1973: The deepening of the wind-mixed layer. *Geophys. Fluid Dyn.*, **3**, 381–404.

Purser, R. J., W. -S. Wu, D. F. Parrish, and N. M. Roberts, 2003: Numerical aspects of the application of recursive filters to variational statistical analysis. Part I: Spatially homogeneous and isotropic Gaussian covariances. *Mon. Wea. Rev.*, **131**, 1524–1535.

Rabier, F., H., J. N. Thepaut, and P. Courtier, 1998: Extended assimilation and forecast experiments with a four-dimensional variational assimilation system. *Quart. J. Roy. Meteor. Soc.*, **124**, 1861–1887.

Reisner, J. R., R. M. Rasmussen, and R. T. Bruintjes, 1998: Explicit forecasting of supercooled liquid water in in winter storms using the MM5 mesoscale model. *Quart. J. Roy. Meteor. Soc.*, **124**, 1071–1107.

Roberts, R. E., J. E. A. Selby, and L. M. Biberman, 1976: Infrared continuum absorption by atmospheric water-vapor in 8–12 um window. *Applied Optics*, **15 (9)**, 2085–2090.

Rodgers, C. D., 1968: Some extensions and applications of the new random model for molecular band transmission. *Quart. J. Roy. Meteor. Soc.*, **94**, 99–102.

Rutledge, S. A., and P. V. Hobbs, 1984: The mesoscale and microscale structure and organization of clouds and precipitation in midlatitude cyclones. XII: A diagnostic modeling study of precipitation development in narrow cloud-frontal rainbands. *J. Atmos. Sci.*, **20**, 2949–2972.

Ryan, B. F., 1996: On the global variation of precipitating layer clouds. *Bull. Amer. Meteor. Soc.*, **77**, 53–70.

Sasamori, T., J. London, and D. V. Hoyt, 1972: Radiation budget of the Southern Hemisphere. *Meteor. Monogr.*, **13**, No. 35, 9–23.

Schwarzkopf, M. D., and S. B. Fels, 1985: Improvements to the algorithm for computing CO2 transmissivities and cooling rates. *J. Geophys. Res.*, **90** (ND6), 541–550.

Schwarzkopf, M. D., and S. B. Fels, 1991: The simplified exchange method revisited — An accurate, rapid method for computation of infrared cooling rates and fluxes. *J. Geophys. Res.*, **96** (D5), 9075–9096.

Skamarock W. C. and J. B. Klemp, 1992: The Stability of Time-Split Numerical Methods for the Hydrostatic and the Nonhydrostatic Elastic Equations, *Mon. Wea. Rev.*: **120**, 2109–2127.

Skamarock W. C. and M. L. Weisman, 2008: The impact of positive-definite moisture transport on NWP precipitation forecasts, *Mon. Wea. Rev.*: submitted.

Skamarock W. C., 2005: Timesplitting techniques for multidimensional transport, available at *http://www.mmm.ucar.edu/individual/skamarock/advect3d_2005.pdf*, 26 pp.

Smirnova, T. G., J. M. Brown, and S. G. Benjamin, 1997: Performance of different soil model configurations in simulating ground surface temperature and surface fluxes. *Mon. Wea. Rev.*, **125**, 1870–1884.

Smirnova, T. G., J. M. Brown, S. G. Benjamin, and D. Kim, 2000: Parameterization of cold-season processes in the MAPS land-surface scheme. *J. Geophys. Res.*, **105** (D3), 4077–4086.

Smolarkiewicz, P. K., and G. A. Grell, 1990: A class of monotone interpolation schemes, *J. Comp. Phys.*, **101**, 431–440.

Stauffer D. R., and N. L. Seaman, 1990: Use of four-dimensional data assimilation in a limited-area mesoscale model. Part I: Experiments with synoptic-scale data. *Mon. Wea. Rev.*, **118**, 1250–1277.

Stauffer D. R., and N. L. Seaman, 1994: Multiscale four-dimensional data assimilation. *J. Appl. Meteor.*, **33**, 416–434.

Stephens, G. L., 1978: Radiation profiles in extended water clouds. Part II: Parameterization schemes, *J. Atmos. Sci.*, **35**, 2123–2132.

Tao, W.-K., and J. Simpson, 1993: The Goddard cumulus ensemble model. Part I: Model description. *Terr. Atmos. Oceanic Sci.*, **4**, 35–72.

Tao, W.-K,, J. Simpson, D. Baker, S. Braun, M.-D. Chou, B. Ferrier, D. Johnson, A. Khain, S. Lang, B. Lynn, C.-L. Shie, D. Starr, C.-H. Sui, Y. Wang, and P. Wetzel, 2003: Microphysics, radiation and surface processes in the Goddard Cumulus Ensemble (GCE) model. *Meteor. and Atmos. Phys.*, **82**, 97–137.

Tao, W.-K., J. Simpson, and M. McCumber 1989: An ice-water saturation adjustment, *Mon. Wea. Rev.*, **117**, 231–235.

Thompson, G., R. M. Rasmussen, and K. Manning, 2004: Explicit forecasts of winter precipitation using an improved bulk microphysics scheme. Part I: Description and sensitivity analysis. *Mon. Wea. Rev.*, **132**, 519–542.

Walko, R. L., W. R. Cotton, M. P. Meyers, and J. Y. Harrington, 1995: Newe RAMS cloud microphysics parameterization. Part I: The single-moment scheme. *Atmos. Res.,* **38**, 29–62.

Wang, W., D. Barker, C. Bruyère, M. Duda, J. Dudhia, D. Gill, J. Michalakes, and S. Rizvi, 2008: WRF Version 3 Modeling System User's Guide. *http://www.mmm.ucar.edu/wrf/users/docs/user_guide_V3/.*

Webb, E. K., 1970: Profile relationships: The log-linear range, and extension to strong stability, *Quart. J. Roy. Meteor. Soc.*, **96**, 67–90.

Wicker, L. J. and W. C. Skamarock, 2002: Time splitting methods for elastic models using forward time schemes, *Mon. Wea. Rev.*, **130**, 2088–2097.

Wicker, L. J., and R. B. Wilhelmson, 1995: Simulation and analysis of tornado development and decay within a three-dimensional supercell thunderstorm. *J. Atmos. Sci.*, **52**, 2675–2703.

Wu, W. -S., R. J. Purser, and D. F. Parrish, 2002: Three-Dimensional Variational Analysis with Spatially Inhomogeneous Covariances. *Mon. Wea. Rev.*, **130**, 2905–2916.

Xiao, Q. N., Y. H. Kuo, J. Sun, W. C. Lee, E. Lim, Y. R. Guo, and D. M. Barker, 2005: Assimilation of Doppler Radar Observations with a Regional 3D–Var System: Impact of Doppler Velocities on Forecasts of a Heavy Rainfall Case. *J. Appl. Met.*, **44(6)**, 768–788.

Xiao, Q., Ying-Hwa Kuo, Juanzhen Sun, Wen-Chau Lee, D. M. Barker, and Eunha Lim, 2007: An approach of radar reflectivity data assimilation and its assessment with the inland QPF of Typhoon Rusa (2002) at landfall. *J. Appl. Meteor. Climat.*, **46**, 14–22.

Xiao, Q., J. Sun, 2007: Multiple radar data assimilation and short-range quantitative precipitation forecasting of a squall line observed during IHOP 2002. *Mon. Wea. Rev.*, **135**, 3381–3404.

Xiao, Q., Eunha Lim, D.-J. Won, J. Sun, W.-C. Lee, M.-S. Lee, W.-J. Lee, J.-Y. Cjo, Y.-H. Kuo, D. M. Barker, D.-K. Lee, and H.-S. Lee, 2008: Doppler radar data assimilation in KMAs operational forecasting. *Bull. Amer. Meteor. Soc.*, **89**, 39–43.

Xiu, A. and J. E. Pleim, 2001: Development of a land surface model part I: Application in a mesoscale meteorology model. *J. Appl. Meteor.*, **40**, 192–209

Xu, M., Y. Liu, C. Davis and T. Warner, 2002: Sensitivity of nudging parameters on the performance of a mesoscale FDDA system: A case study. 15th Conference on Numerical Weather Prediction, 12-16 August, 2002, San Antonio, Texas, 127-130.

Xue, M., 2000: High-order monotonic numerical diffusion and smoothing. *Mon. Wea. Rev.*, **128**, 2853–2864.

Zhang, D.-L., and R.A. Anthes, 1982: A high-resolution model of the planetary boundary layer–sensitivity tests and comparisons with SESAME–79 data. *J. Appl. Meteor.*, **21**, 1594–1609.

Zilitinkevich, S. S., 1995: Non-local turbulent transport: pollution dispersion aspects of coherent structure of convective flows, *Air Pollution III* — Volume I. Air Pollution Theory and Simulation, Eds. H. Power, N. Moussiopoulos and C.A. Brebbia. Computational Mechanics Publications, Southampton Boston, 53–60.